

Impinging Drops on Superhydrophobic Surfaces at Icing Conditions

A Dissertation
Presented to the Faculty of the
School of Engineering and Applied Science
University of Virginia

In Partial Fulfillment
of the Requirements for the Degree of
Doctor of Philosophy in Mechanical and Aerospace Engineering

by

YONG HAN YEONG

M.S., University of Illinois, Champaign-Urbana, IL – 2009
B.S., Purdue University, West Lafayette, IN – 2007

May 2014

Approval Sheet

The dissertation is submitted in partial fulfillment of the requirements for the degree of Doctor of Philosophy in Mechanical and Aerospace Engineering

Yong Han Yeong, Author

This dissertation has been read and approved by the examining committee:

Dr. Eric Loth, Advisor

Dr. Ilker Bayer

Dr. Carl Knospe

Dr. David Green

Dr. Patrick Hopkins, Chairman

Accepted for the School of Engineering and Applied Science:

Dean, School of Engineering and Applied Science

May 2014

Abstract

Due to their excellent water repellent characteristics, superhydrophobic surfaces have been hypothesized to be icephobic. This is based on the premise that water droplets will be repelled from the surface before ice nucleation can occur. The icephobic nature of these surfaces provides an attractive solution to current icing problems that can occur in aerospace applications. However, significant challenges remain before anti-wetting coatings could be implemented as an effective ice mitigation tool. For example, the majority of current synthetic superhydrophobic surfaces are fragile and unable to withstand the harsh environmental conditions that are encountered by aerospace applications. In addition, their static and dynamic wettability at varying temperatures and humidity, as well as their ice-shedding performance under the impact of a super-cooled icing cloud, are not well understood.

Therefore, in this dissertation, fabrication techniques for a previously developed nanocomposite surface were improved so that coatings of consistent anti-wetting performance and durability could be produced. The icephobicity of this nanocomposite coating was then systematically investigated. First, an experiment was conducted to study the wettability of a water drop on the coating for a full temperature cycle (20°C to -3°C and back to 20°C) and at varying humidity levels. The investigation was then extended to study the impact and rebound dynamics of a

drop on an inclined coating, at different fluid viscosities and at various temperatures (50°C to -8°C). This was followed by a study of ice adhesion strength of the coatings created under the impingement of 20 μm super-cooled water droplets. The receding contact angle was discovered from these experiments to be a key parameter in controlling superhydrophobic wettability and ice adhesion. Therefore, the receding angle depinning dynamics from a superhydrophobic surface were also studied in detail at micron length scales and at microsecond temporal scales. In summary, results from this dissertation revealed the crucial parameters that govern the icing performance of a nanocomposite superhydrophobic surface.

For my grandma

Acknowledgements

The process of completing this dissertation has been arduous and would not have been possible without the guidance and support of various outstanding individuals. First and foremost, my most sincere thanks goes to my advisor and mentor, Dr. Eric Loth, who graciously offered me the opportunity to join his research team four years ago, and to partake in a new journey of learning and discovery in the area of nanotechnology. By constantly challenging me to think outside the box, I truly believe I have grown to become a better scientist and engineer. I am also indebted to Dr. Ilker Bayer and Dr. Adam Steele, who have provided both technical guidance and mental support during the challenging moments of my dissertation study. Special thanks goes out to my fellow colleagues, Dr. Athanasios Milionis and Alex Davis for all the assistance that was provided to me. Thank you to my roommates (and good friends) over the years: Albert Lee, Jason Mickey, Tyler Gillen, Kevin Clark, Dr. Dominic Barone, Nam Le, Ashleigh Allen and Brooks Child. You all have made my time at Virginia an enjoyable one!

I also want to thank Areva and Rolls-Royce for sponsoring this research for the past four years. To my principal investigators, Dr. Charles Lakeman, Dr. Guillaume DeCombarieu, Dr. Dinesh Gera and Dr. Jack Sokhey, thank you for guiding me in my studies and providing insights into the process of engineering

problem-solving from the industrial perspective. The opportunity of research collaboration with industrial partners is very valuable to a graduate student like me, and for that I am thankful.

Last but not least, I want to thank my parents and my sister for their unwavering and unconditional love and support. To my parents, who have sacrificed so much over the last 10 years for me to achieve my goals and to fulfill my dreams, I owe you everything. You truly are the greatest parents in the world!

Table of Contents

List of Figures	xii
List of Tables.....	xix
Nomenclature	xx

Chapter 1 – Introduction

1.1. Background	1
1.2. Wetting Models	2
1.3. Motivation and Problem Definition	7
1.4. Objectives and Dissertation Outline	9

Chapter 2 – Fabrication and Durability of Nanocomposite Coatings

2.1. Introduction	11
2.2. Materials and Method	13
2.2.1. Nanocomposite Fabrication.....	13
2.2.2. Performance Measurement.....	16
2.3. Results and Discussion	18
2.4. Conclusions	32

Chapter 3 – Temperature and Humidity Effects

3.1. Introduction	33
3.2. Experimental Methods.....	35
3.2.1. Nanocomposite Coating.....	35

3.2.2. Experimental Set-Up.....	36
3.3. Results and Discussion.....	38
3.4. Conclusions	43

Chapter 4 – Drop Impact and Rebound Dynamics

4.1. Introduction	44
4.2. Experimental Methods.....	48
4.2.1 Nanocomposite Fabrication.....	48
4.2.2. Experimental Set-Up.....	50
4.2.3. Test Conditions.....	53
4.3. Results and Discussion	57
4.3.1. Drop Contact Time and Maximum Spread on Surface...60	
4.3.2. Rebound Outcome Classifications and Regime Map.....67	
4.4. Conclusions	74

Chapter 5 – Ice Adhesion Strength with a Thick “Defect”

5.1. Introduction	76
5.2. Experimental Methods.....	80
5.2.1. Experimental Set-Up.....	80
5.2.2. Tested Coatings.....	86
5.2.3. Test Procedures and Conditions.....	94
5.2.4. Calculation of Ice Fracture Energy.....	98

5.3.	Results and Discussion	100
5.4.	Conclusions	106

Chapter 6 – Ice Adhesion Strength with a Thin “Defect”

6.1.	Introduction	107
6.2.	Experimental Methods.....	108
6.2.1.	Experimental Set-Up.....	108
6.2.2.	Modification of Test Procedures.....	112
6.2.3.	Tested Coatings.....	113
6.3.	Results and Discussion	117
6.4.	Conclusions	137

Chapter 7 – Microscopic Receding Angle Dynamics

7.1.	Introduction	139
7.2.	Experimental Methods.....	143
7.2.1.	Fabrication of Textured Pillar Surface.....	143
7.2.2.	Fabrication of the Nanocomposite Surface.....	146
7.2.3	Experimental Set-Up.....	147
7.3.	Results and Discussion.....	149
7.3.1.	Textured Pillar Surface.....	149
7.3.2.	Irregular Nanocomposite Surface.....	162
7.4.	Conclusions	164

Chapter 8 – Conclusions

8.1.	Fabrication and Durability of Nanocomposite Coatings	166
8.2.	Temperature and Humidity Effects	167
8.3	Drop Impact and Rebound Dynamics.....	167
8.4	Ice Adhesion Strength with Thick and Thin “Defects”.....	168
8.5	Microscopic Receding Angle Dynamics.....	169
8.6	Contributions of Dissertation and Recommendations.....	170
References		173

List of Figures

	Figure caption	Page
Figure 1.1	Schematic of wetting models (a) equilibrium contact angle, (b) apparent contact angle in Wenzel state and (c) apparent contact angle in Cassie State.....	4
Figure 1.2	Images of a drop on surfaces of different wetting states (a) hydrophilic, (b) hydrophobic and (c) superhydrophobic (with ROA of less than 10°)..	5
Figure 1.3	Schematic of a drop sliding down an inclined surface. Definitions of ROA, ACA and RCA are as indicated	6
Figure 1.4	Icing in an aircraft turbofan engine (a) ice accretion on the inlet fan blades and (b) close up view of icing on the outlet guide vanes.....	7
Figure 2.1	(a) Schematic of the spray-casting process and (b) image of the spray-casting set-up.	15
Figure 2.2	Effect of spray-casting height on superhydrophobicity of the nanocomposite coating (spray-casting air pressure fixed at 415 kPa gage).....	19
Figure 2.3	Optical microscope images of “wet” and “dry” nanocomposite coatings spray-casted at heights of (a) 5cm and (b) 13 cm (spray-casting air pressure fixed at 415 kPa gage).....	20
Figure 2.4	SEM images of nanocomposite coatings spray-coated at a height of (a) 5cm and (b) 7.5 cm (spray-casting air pressure fixed at 415 kPa gage).....	21
Figure 2.5	3D topological images (800 X 800 μ m surface area) of “wet” and “dry” nanocomposite coatings spray-casted at heights of (a) 5cm and (b) 13 cm (spray-casting air pressure fixed at 415 kPa gage).....	22
Figure 2.6	Effect of spray-casting air pressure on superhydrophobicity of the nanocomposite coating (spray-casting height fixed at 7.5 cm).....	24

Figure 2.7	Effect of slurry droplet flight time on the CA of the nanocomposite coating.	27
Figure 2.8	Effect of slurry droplet flight time on the ROA of the nanocomposite coating.....	28
Figure 2.9	Dependence of wear rate (thickness of coating worn per abrasion cycle) on (a) spray-casting pressure fixed at 415 kPa gage and (b) spray-casting height fixed at 7.5 cm.....	29
Figure 2.10	Image of coating (spray-casted at a height and pressure of 13 cm and 415 kPa gage, respectively) subjected to abrasion until the point of coating breakthrough.....	30
Figure 3.1	SEM images of nanocomposite coating at magnifications of (a) 200X and (b) 3000X.	36
Figure 3.2	Experimental set-up for thermally homogeneous, high and low humidity tests. (a) schematic and (b) picture of the set-up within the refrigerated incubator.....	37
Figure 3.3	Superhydrophobic performance of nanocomposites for a temperature cycle (20°C to -3°C to 20°C) while maintaining thermal homogeneity at each point of measurement (a) CA at low RH (b) ROA at low RH (c) CA at high RH and (d) ROA at high RH.	39
Figure 3.4	Homogeneous vs. non-homogeneous thermal effects on the superhydrophobicity of the nanocomposites.....	41
Figure 4.1	Experimental set-up for single drop oblique impact test (a) schematic and (b) picture of the set-up within the refrigerated incubator.	51
Figure 4.2	Set up of experimental apparatuses outside the refrigerated incubator	53
Figure 4.3	ACA and RCA measurements of the nanocomposite superhydrophobic surfaces for water and water-glycerol solutions at different viscosities.	57
Figure 4.4	Categorization of water drop impact and rebound stages on an inclined (a) polyurethane topcoat surface ($We_N=11.5$) and (b) nanocomposite superhydrophobic coating ($We_N=23$).	58

Figure 4.5	Drop contact times of all liquid drops at different viscosities on a superhydrophobic surface as a function of capillary time scale, where data from Richard <i>et al.</i> is for normal impacts and present data are for oblique impacts..	61
Figure 4.6	The relationship between non-dimensional maximum spread of drops on superhydrophobic surfaces with normal Weber number, comparing drops at various viscosities impacting on an inclined surface with water drops on a horizontal surface from current data as well as from Comeau <i>et al.</i> and Clanet <i>et al.</i>	63
Figure 4.7	Comparison of high-speed images acquired for a water drop impact and rebound on an inclined superhydrophobic surface at $We_N=57$ and $We=113$, horizontal superhydrophobic surface at $We = We_N= 61$ and horizontal superhydrophobic surface at $We = We_N = 111$.	64
Figure 4.8	(a) Classification of high-speed images of drop rebound, disengagement and post-impact outcomes after impingement on an inclined superhydrophobic surface and (b) sequence of images depicting an expanding-contracting drop during the post-impact stage.	68
Figure 4.9	(a) Sketches of drop shapes and outcomes for the stages of rebound, disengagement and post impact based on images classified in Figure 4.9, and (b) sketches of drop shapes depicting an expanding-contracting drop during the post-impact stage.	69
Figure 4.10	Regime map depicting the rebounding outcomes of an oblique drop impact on the superhydrophobic surface as a function of We_N and Oh , with red arrow indicating outcome variability at high We_N and low Oh	70
Figure 5.1	Schematic of the experimental set-up.	81
Figure 5.2	Picture of the walk-in cold chamber used in the ice adhesion experiment.	82
Figure 5.3	Pictures of the experimental set-up in the walk-in cold chamber. (a) side view and (b) top view.	84

Figure 5.4	NASA Icing Wind Tunnel Mod-1 nozzle. (a) picture of the nozzle and (b) calibration air and water pressure curves of the nozzle to produce desired droplet sizes.....	85
Figure 5.5	Design of the boss piece attached with test substrate discs. (a) aluminum substrate disc, (b) Ti 6-4 substrate disc and (c) ice accretion on an aluminum substrate disc.	86
Figure 5.6	Optical microscope pictures of a titanium 6-4 surface. (a) as-received and (b) shot-peened.	88
Figure 5.7	SEM images of (a) SH-8, (b) SH-3 and (c) SH-1. (d-f) are high magnification images of respective coatings. A reduction in surface cracking and increase in general homogeneity was observed from SH-8 to SH-1.	93
Figure 5.8	Stages of ice accretion on substrate disc followed by removal by pressurized air. (a) 2 mm thick ice after 20 seconds spray, (b) 6 mm thick ice after 80 seconds spray, (c) 10 mm thick ice after 135 seconds spray and (d) release of ice by pressurized air.	95
Figure 5.9	Sequence of the experiment procedures.	96
Figure 5.10	Temperature variation of air, substrate disc, spray nozzle and water tube with respect to time.	97
Figure 5.11	Top-down perspective of the substrate disc after ice fracture (a) mixed-mode fracture (cohesive + adhesive) on an as-received aluminum surface and (b) full adhesive fracture on an <i>Aculon</i> surface.	99
Figure 5.12	Ice fracture pressure of all tested coatings.	101
Figure 5.13	Ice fracture energy of all tested coatings.	101
Figure 5.14	Percentage area of adhesive fracture of coatings plotted with respect to its fracture energy to identify coatings with desirable ice release performance.	103
Figure 5.15	Effect of coating CA on ice fracture energy.	104

Figure 5.16	Effect of coating CAH on ice fracture energy.....	105
Figure 5.17	Effect of coating RCA on ice fracture energy.....	105
Figure 6.1	Schematic of the experimental set-up. (a) set-up for thick “defect” experiments and (b) modified set-up for thin “defect” disc experiments....	110
Figure 6.2	A 50 μm thick “defect” disc secured on a <i>Hydrobead</i> substrate disc by an adjusted suction force provided by a vacuum pump.....	111
Figure 6.3	Sequence of the modified experiment procedures.....	112
Figure 6.4	SEM images of (a) UVA ABS and (b) <i>Hydrobead 2</i> coating at 500 \times magnification. (c and d) are high magnification images of respective coatings at 5000 \times	117
Figure 6.5	Effect of CA and averaged S_a (color-coded) on ice fracture energy of all tested coatings.....	119
Figure 6.6	Effect of CAH and averaged S_a (color-coded) on ice fracture energy of all tested coatings.....	119
Figure 6.7	Effect of RCA and averaged S_a (color-coded) on ice fracture energy of all tested coatings.....	120
Figure 6.8	Effect of RCA and averaged S_a (color-coded) on ice fracture energy of hydrophobic coatings fabricated on titanium 6-4 substrates.	122
Figure 6.9	Effect of RCA and averaged S_a (color-coded) on ice fracture energy of hydrophobic coatings fabricated on aluminum substrates.	122
Figure 6.10	Effect of RCA and averaged S_a (color-coded) on ice fracture energy of superhydrophobic coatings fabricated on aluminum substrates.....	123
Figure 6.11	Profile examples of positive and negative S_{sk} with its height distribution curves.....	125
Figure 6.12	Profile examples of S_{ku} above and under 3, with its height distribution curves.....	126

Figure 6.13	Effect of RCA and averaged S_{sk} (color-coded) on ice fracture energy of superhydrophobic coatings fabricated on aluminum substrates.....	127
Figure 6.14	Effect of RCA and averaged S_{ku} (color-coded) on ice fracture energy of superhydrophobic coatings fabricated on aluminum substrates.....	128
Figure 6.15	3D topology image of pillar surfaces with S_a and S_{al} measurements. (a) inter-pillar distance of 28 μm and (b) inter-pillar distance of 90 μm .	131
Figure 6.16	Effect of S_{al} and S_{sk} on ice fracture energy of superhydrophobic coatings fabricated on aluminum substrates.	132
Figure 6.17	3D topology images of superhydrophobic coatings with S_{al} measurements (a) <i>Hydrobead</i> 2 (b) SH-d and (c) SH-a.	134
Figure 6.18	Effect of S_{al} and S_a on ice fracture energy of superhydrophobic coatings SH-1, 3 and 5 fabricated for tests described in Chapter 5...	135
Figure 6.19	3D topology image of SH-c superhydrophobic coating. The image shows a rough surface with deep valleys..	136
Figure 7.1	SEM images of a pillar surface at $L = 63\mu\text{m}$. (a) pristine surface prior to deposition of PTFE particles (b) superhydrophobic pillar surface after deposition of PTFE particles (c) $5000\times$ magnified image of the PTFE particles on a pillar and (d) $80,000\times$ magnified image of PTFE particles on a pillar...	144
Figure 7.2	SEM images of a nanocomposite superhydrophobic surface. (a) $1000\times$ magnified image and (b) $20,000\times$ magnified image....	147
Figure 7.3	Schematic of the experimental setup depicting the tilt method and driving method.....	148
Figure 7.4	Sequence of images depicting the first and last 0.26 ms of the microscopic receding line motion on a pillar surface ($L = 63\mu\text{m}$) while at tilt.....	150
Figure 7.5	Sketches of the position of individual microscopic receding lines on a pillar from the receding line onset until point of “snapping” for surfaces (a) $L = 63\mu\text{m}$ and (b) $L = 120\mu\text{m}$	152

Figure 7.6	Measurements of the angles of each receding contact line as a function of time for a length of four pillars. Surfaces consist of (a) $L = 63\mu\text{m}$ (b) $L = 90\mu\text{m}$ (c) $L = 105\mu\text{m}$ and (d) $L = 120\mu\text{m}$	154
Figure 7.7	Averaged microscopic and apparent receding angles acquired for a distance of four pillars as a function of non-dimensional time ($t^* = (t - t_0)/T$) where t , t_0 and T represents the current, initial and total duration of receding line travel on a single pillar, respectively.....	156
Figure 7.8	A comparison of the averaged microscopic receding angles for all pillar surfaces at varying L distances as a function of non-dimensional time ($t^* = (t - t_0)/T$) where t , t_0 and T represents the current, initial and total duration of receding line travel on a single pillar, respectively.....	157
Figure 7.9	Averaged travel speed of the apparent and microscopic receding lines as a function of inter-pillar distance.....	160
Figure 7.10	Coefficient of dynamic friction of pillar surfaces.....	161
Figure 7.11	Sketches of the position of individual microscopic receding lines on an irregular nanocomposite coating from the receding line onset until point of “snapping”.....	162
Figure 7.12	Measurements of the angles of each receding contact line as a function of time for a length of four irregular surface features.....	163

List of Tables

	Table title	Page
Table 2.1	Surface texture parameters of “wet” and “dry” nanocomposite coatings spray-casted at 5 and 13 cm (spray-casting air pressure fixed at 415 kPa gage).....	23
Table 4.1	Viscosity, density, surface tension and temperature values of test liquids used in the present experiments.....	55
Table 5.1	Nanocomposite formulations, surface preparation and spray deposition parameters for the fabrication of SH-1, SH-3 and SH-8 coatings.	90
Table 6.1.	S_a , S_{sk} and S_{ku} values for superhydrophobic surfaces with ice fracture energies of less than 0.6 J, as compared to superhydrophobic surfaces from Kulinich and Farzaneh.	129
Table 7.1	Apparent measurements of the superhydrophobic performance of the textured pillar and nanocomposite surfaces.....	146

Nomenclature

a	Acceleration
A	Area
B	Turbulent decay jet constant
c	Radius of defect
C_1	2 nd order correction factor for ΔLE
C_2	2 nd order correction factor for ΔTE
C_3	Difference between C_1 and C_2
d	Drop diameter
D	Spray nozzle diameter
E	Young's modulus for ice
f_1	Ice fracture energy constants
f_2	Ice fracture energy constants
g	Gravity
h	Height of ice accretion
L	Inter-pillar distance
L_{max}	Maximum spread of drop
m	Mass of drop
M	Mach number
Oh	Ohnesorge number

P_i	Air pressure at spray nozzle exit
P_o	Air pressure at upstream of spray nozzle
P_{atm}	Atmospheric pressure
P_c	Critical pressure for ice fracture
r	Wenzel wetting state surface roughness
S_a	Arithmetic mean roughness
S_{sk}	Skewness
S_{ku}	Kurtosis
S_q	Root mean squared surface roughness
S_{al}	Autocorrelation length
t_x	Autocorrelation function (in x-direction)
t_y	Autocorrelation function (in y-direction)
t^*	Non-dimensional time for microscopic receding line travel
t	Current time of microscopic receding line travel
t_o	Initial time of microscopic receding line travel
t_{flight}	Time of flight of slurry droplets
T	Total duration of travel of microscopic receding line on 4 pillars
U_i	Initial air velocity at spray nozzle exit
U_c	Centerline air velocity of turbulent jet
$V_{apparent}$	Velocity of apparent receding line

$V_{microscopic}$	Velocity of microscopic receding line
V_N	Normal velocity
V_T	Tangential velocity
We_N	Normal Weber number
We_T	Tangential Weber number
W	Width of pillar
z	Height of surface features

Greek Symbols

γ	Air specific heat ratio
γ_{sv}	Solid-vapor surface tension
γ_{ls}	Liquid-solid surface tension
γ_{lv}	Liquid-vapor surface tension
θ	Equilibrium contact angle
θ^*	Apparent contact angle
ΔLE	Leading edge shift of drop maximum spread at oblique impact
ΔTE	Trailing edge shift of drop maximum spread at oblique impact
μ_{pillar}	Coefficient friction of drop on pillar surface
μ_p	Viscosity of drop
ν	Poisson's ration of ice

ϱ_p	Density of drop
σ	Surface tension of drop
2τ	Cohesive ice fracture
τ_{cap}	Capillary time scale of drop
τ_{cont}	Contact time of drop on surface
ϕ	Solid-liquid area fraction
ω	Adhesive ice fracture

List of Abbreviations

ACF	Autocorrelation function
ACA	Advancing contact angle
CA	Contact angle
CAH	Contact angle hysteresis
HMFS	Hydrophobically modified fumed silica
MCPU	Moisture-cured polyurethane
PMC	Waterborne perfluoroalkyl methacrylic copolymer
PTFE	Polytetrafluoroethylene
RCA	Receding contact angle
ROA	Roll-off angle

RH	Relative humidity
SH	Superhydrophobic
SLR	Single lens reflex
SEM	Scanning electron microscope

Chapter 1

Introduction

1.1 Background

Inspired by nature, specifically the lotus leaf, superhydrophobic surfaces feature remarkable water repellent characteristics. This water repellency effect is due in part to a low surface energy which reduces the molecular scale attraction between a liquid and the solid of the surface. However, a distinct surface morphology is also required. This morphology usually consists of micro/nano scale features that are closely spaced to trap a layer of air in between the asperities. This results in the suspension of water droplets on the tips of these features to reduce the liquid-surface contact area. The combination of these two effects causes water droplets to bead up, roll or bounce off superhydrophobic surfaces with great ease and provides a self-cleaning mechanism known as the “lotus effect”.¹

Given the potential of superhydrophobic surfaces in providing solutions in different areas of applications such as textile and electronics water-proofing, anti-corrosion/fouling applications as well as drag reduction in marine and fluid-powered systems, researchers have been seeking to reproduce the superhydrophobic effect on synthetic surfaces. To date, thousands of publications have been published featuring successful studies in creating synthetic superhydrophobic surfaces using a wide-array of methods and materials.²⁻⁴ Fabrication methods include surface etching techniques (plasma, laser, chemical),⁵⁻⁷ lithography (photolithography, electron beam, X-ray),^{8,9} electrochemical deposition processes^{10,11} as well as electro-spinning techniques.¹²

1.2 Wetting Models

The wettability of a surface can be described mathematically using three models. If a drop is placed on a completely smooth surface, it will spread itself on the surface. Its equilibrium angle can therefore be described as a function of surface tension between the liquid, solid and vapor phases. As shown in Equation 1.1, this is the Young's equation

$$\cos\theta = \frac{\gamma_{sv} - \gamma_{ls}}{\gamma_{lv}} \quad (1.1)$$

where γ is the surface tension, s, l and v are the solid, liquid and vapor phases, θ is the equilibrium contact angle of drop on flat surface.

If roughness is introduced to the smooth surface considered in the Young's equation, one can expect the liquid from a drop to infiltrate the asperities to fully wet the surface. The apparent contact angle of this surface can be described by the Wenzel model¹³ as Equation 1.2.

$$\cos\theta^* = r \cos\theta \quad (1.2)$$

where r is the dimensionless roughness factor defined as the actual surface (surface area including the walls of the roughness) divided by the geometric surface (the projected area of the drop on the surface) and θ^* the apparent contact angle on the textured surface.

Consider a surface with roughness similar to the condition in Wenzel model. Instead of a penetration of liquid into the asperities, the spaces in between the asperities are filled with a layer of air, therefore suspending a drop on tips of the asperities. This can be described by the Cassie-Baxter model¹⁴ (Equation 1.3) and is also the condition for superhydrophobicity.

$$\cos\theta^* = -1 + \phi_s (1 + \cos\theta) \quad (1.3)$$

where ϕ_s is the area fraction of solid-liquid contact.

Schematic representations of the three wetting models are shown in Figure 1.1.¹⁵

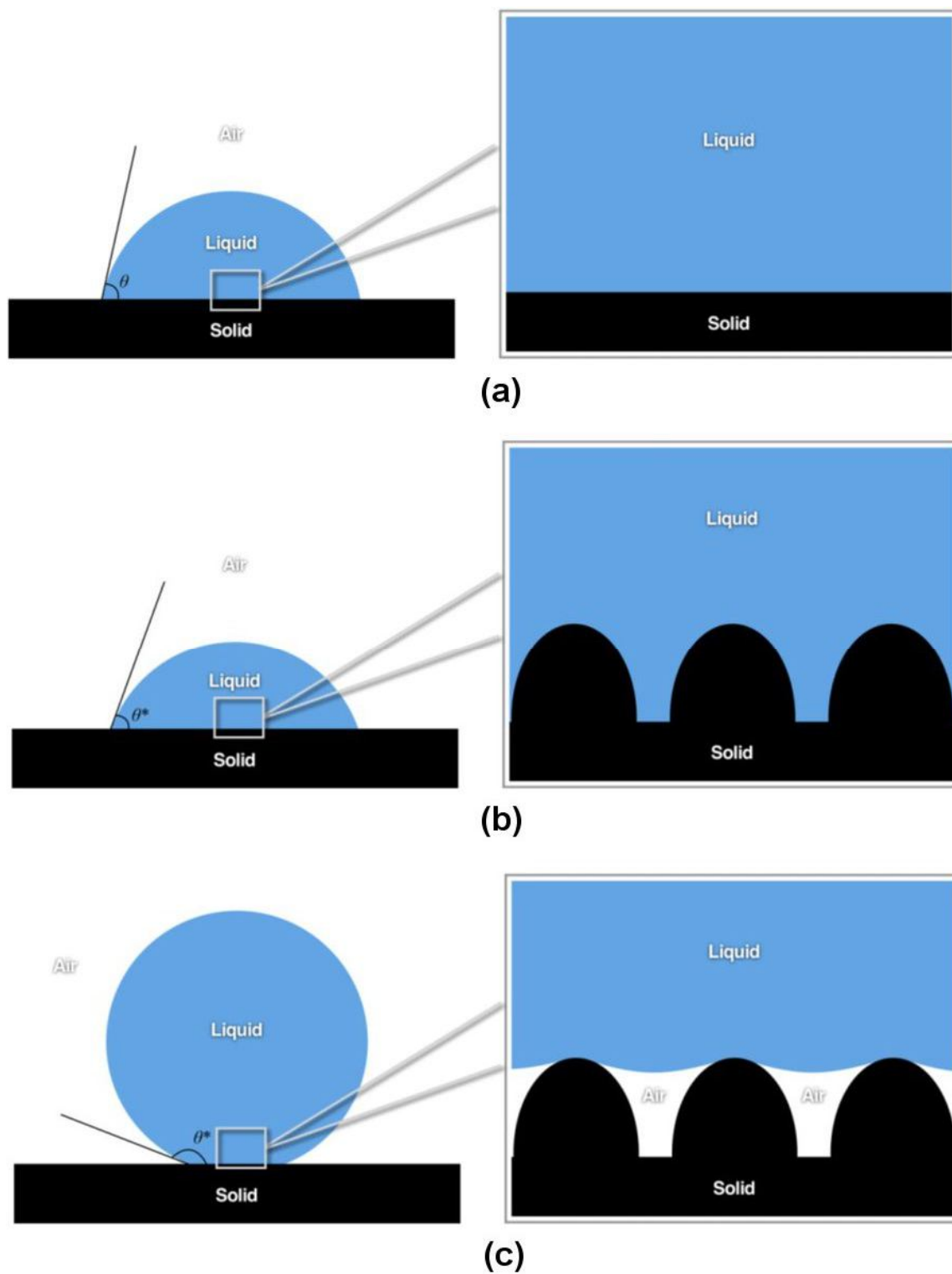


Figure 1.1 Schematic of wetting models (a) equilibrium contact angle, (b) apparent contact angle in Wenzel state and (c) apparent contact angle in Cassie State.

The degree of superhydrophobicity is quantified by the combination of water drop static contact angle (CA) and drop roll-off angle (ROA). As shown in Figure 1.2, the contact angle is the angle between the liquid and solid surface contact line. At a low CA, the water drop spreads and stretches along the surface (Figure 1.2a). As the drop beads up, the contact area between the drop and surface decreases and the CA increases (Figure 1.2b and c). The drop ROA is defined as the surface inclination angle in which the drop is released from the surface and begins to slide down the inclination. A schematic of this angle is shown in Figure 1.3. A surface with a CA measurement of less than 100° is hydrophilic. If the surface CA is between 100° and a 150° , it is typically termed a hydrophobic surface. A superhydrophobic surface is defined as a surface with a CA greater than 150° and a ROA of less than 10° .

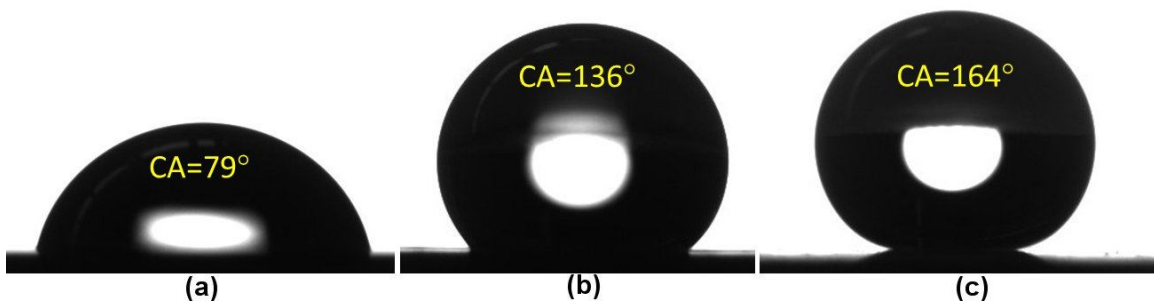


Figure 1.2 Images of a drop on surfaces of different wetting states (a) hydrophilic, (b) hydrophobic and (c) superhydrophobic (with ROA of less than 10°).

A related measurement to the drop ROA is the drop contact angle hysteresis (CAH). As shown in Fig. 1.3, as a drop slides off a surface, an angle is created between the liquid-solid interface at the leading edge of the drop, called an advancing contact angle (ACA). A similar measurement could be made on the trailing edge of the drop, called a receding contact angle (RCA). Therefore, the CAH is defined as the difference between the advancing and receding contact angle. The measurements of CAH, ACA and RCA are critical towards determining the extent of mobility of a drop on a superhydrophobic surface as they quantify the affinity of the drop on the surface under dynamic conditions. Superhydrophobic surfaces that depict extreme water repellency characteristics typically have high RCA ($> 140^\circ$) and small CAH values ($< 10^\circ$).

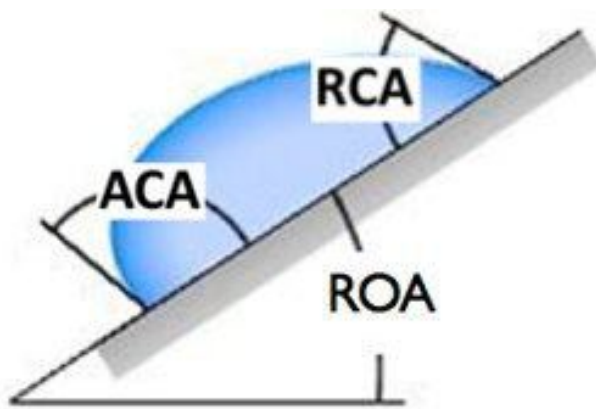


Figure 1.3 Schematic of a drop sliding down an inclined surface. Definitions of ROA, ACA and RCA are as indicated.

1.3 Motivation and Problem Definition

The extreme water-repellent characteristics of superhydrophobic surfaces have led to the hypothesis that anti-wetting coatings could be ice-phobic. This is based on the premise that water drops/droplets will be repelled from a superhydrophobic surface before ice nucleation can occur.

The occurrence of icing creates undesirable effects on the performance of aircraft, aircraft engines and wind turbines. Ice accretion typically occurs when an aircraft or wind turbine encounters an icing cloud consisting of super-cooled water droplets in freezing environmental conditions. These droplets impact the surfaces to instantaneously form ice. An iced wing on an aircraft can lead to a complete stall with devastating consequences as evidenced by the crash of an ATR-72 commuter aircraft near Roselawn, Indiana on October 31st 1994.¹⁶ As shown in Figure 1.4, ice accretion can also occur under similar environmental conditions on an aircraft

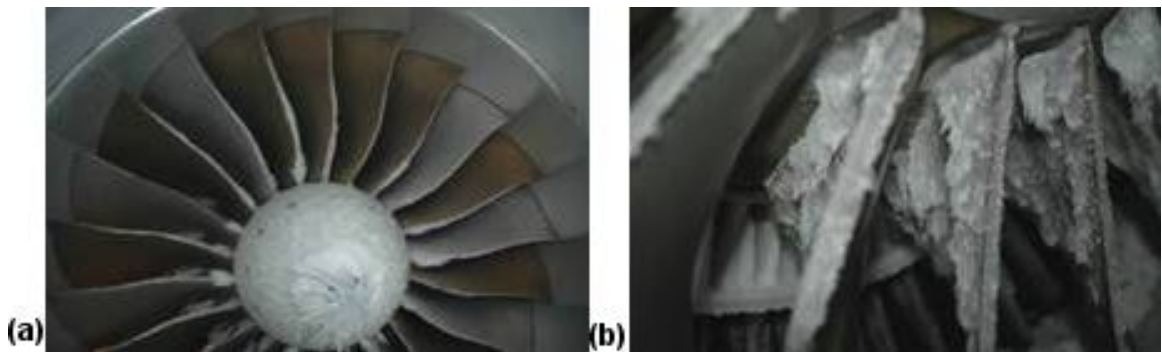


Figure 1.4 Icing in aircraft turbofan engine (a) ice accretion on the inlet fan blades and (b) close up view of icing on the outlet guide vanes.

engine.¹⁷ These conditions can cause a loss in engine power and thus create an aviation safety hazard. In addition, icing on the blades of a wind turbine can reduce its annual power production by up to 50%.¹⁸ Current ice-mitigation strategies include pneumatically controlled rubber boots often installed on turboprop aircraft to shed any ice that forms at the leading edge of the wing. Electro-thermal de-icing systems are also typically employed on turbofan aircraft surfaces and engines as well as on wind turbines. However, these existing de-icing technologies still have a few weaknesses. Operation of the pneumatic de-icing boot is effective only after a certain amount of ice build-up has occurred on the surface¹⁹, while electro-thermal systems require a continuous supply of energy, which often reduces the operating efficiency of the aircraft components or wind turbine.

Therefore, the use of superhydrophobic surfaces as an inherent ice-repellent surface could serve as an attractive alternative to the de-icing technologies described above. However, challenges still remain before these anti-wetting coatings could be implemented as an effective ice mitigation tool. The majority of current synthetic superhydrophobic surfaces such as the ones listed in Section 1.1 are fragile and unable to withstand the harsh environmental conditions typically encountered by aerospace applications. Therefore, a durable superhydrophobic coating is desired. In addition, the static and dynamic wettability, as well as its ice-shedding performance

of the superhydrophobic surface under aerospace icing conditions is still not well understood.

1.4 Objectives and Dissertation Outline

The overarching goal of this dissertation is to study the wettability performance and hence ice-shedding capabilities of a nanocomposite superhydrophobic nanocomposite surface at aerospace icing conditions. This is systematically studied through five objectives presented in six chapters:

- i) Chapter 2: Improve fabrication techniques of the nanocomposite surface which was previously developed by Steele¹⁵ so that coatings of consistent anti-wetting performance and durability suitable for aerospace applications could be produced.
- ii) Chapter 3: Study the wettability of *a drop* on the nanocomposite coating for a full temperature cycle (20 ° C to -3 ° C and back to 20°C) and at varying humidity levels.
- iii) Chapter 4: Investigate the impact and rebound dynamics of *a drop* on an inclined nanocomposite coating (45°) at varying temperatures (50°C to -8°C) and at various fluid viscosities.

- iv) Chapter 5 & 6: Conduct a study of the ice adhesion strength of hydrophobic and superhydrophobic coatings under an *icing spray* consisting of 20 μm water droplets.
- v) Chapter 7: Perform a study of the microscopic receding angle dynamics on a textured pillar and on an irregular nanocomposite superhydrophobic surface. (The receding angle was discovered to be a key wettability parameter in affecting single drop rebound dynamics as well as for ice adhesion strength)

Each of these objectives involved studies that required the design and implementation of separate experiments. They are therefore presented as individual chapters and written as independent articles to convey pertinent information to the reader. In addition, the results from the study of ice adhesion strength of superhydrophobic surfaces (objective iv) are separated into two chapters (one for a thick “defect” and the other for a thin “defect”). Finally, a conclusion to summarize the results for all these objectives is presented in Chapter 8. In addition, a summary of the contributions from this dissertation to the field of anti-icing superhydrophobicity is also provided.

Chapter 2

Fabrication and Durability of Nanocomposite Coatings

2.1 Introduction

As previously mentioned in Chapter 1, various synthetic superhydrophobic surfaces have been successfully fabricated by researchers. However, it is uneconomical and impractical to adopt most of these fabrication methods for realistic large-area applications. This is due to the expensive and restrictive fabrication processes commonly associated with these fabrication techniques. In addition, these superhydrophobic surfaces are fragile and prone to damage when exposed to the harsh environmental conditions typically encountered in aerospace applications. To resolve this problem, researchers have recently employed a method in which a nanoparticle-polymer suspension is atomized, dispersed and coated on a surface via spray deposition techniques.²⁰⁻³¹ By introducing heat to the surface

thereafter, the polymer chains on the coating can crosslink and self-assemble into a durable, superhydrophobic nanocomposite coating.³²⁻³⁴ This fabrication method is a simple and cost-effective process that can be applied to not only a large surface area but also to a variety of substrate materials.

Although the mechanism for the formation of superhydrophobic nanocomposites by spray atomization has been well documented,²⁰ the effects of the spray deposition parameters, i.e., spray-casting height and spray air pressure, on the superhydrophobicity and wear durability of the coating are largely unknown. Understanding these effects is critical for large-scale manufacturing processes such as for aerospace applications where coatings of consistent durability and superhydrophobicity are desired. The effects of these spray deposition conditions have not been investigated in detail nor are they well understood. In fact, most studies on spray-casting for superhydrophobic surfaces do not report the details of these spray parameters. One study that gave more detail was that of Manoudis *et al.*²⁴ who reported that their selection of spray pressures were chosen by trial and error and noted poor adherence of the superhydrophobic coatings for certain spray times. Since the spray-casting height and pressure can have a significant impact on the performance properties of the resulting coatings, this study sought to systematically investigate these effects. In particular, this was completed for polyurethane clay-fluorine nanocomposite coatings, which have been previously

investigated in terms of adhesion strength as a function of mixture components by Steele *et al.*³² We expand that work by fabricating these superhydrophobic coatings from a range of spray-casting heights and spray air pressures so that its effect on the superhydrophobicity (by measurement of CA and ROA and wear durability (by linear surface abrasion) of the surface can be quantified.

2.2 Materials and Method

2.2.1 Nanocomposite Fabrication

Precursor solutions were first created, followed by spray casting and then thermosetting to produce the final nanocomposite coatings. First, 2.6 g of polyurethane was dispersed via vortex-mixing in 15.7 g of ethyl alcohol. Next, 4 g of as-received dimethyl dialkyl C14-C18 amine functionalized montmorillonite clay particles (Nanoclay, Nanocor Inc., USA) were added using a spatula and vortex-dispersed in the polyurethane-alcohol mixture. Finally, 15 g of waterborne fluorinated acrylic copolymer (25%wt polymer, 75%wt water; Dupont) was added slowly to the polyurethane-nanoclay suspension and also blended with vortex mixing for 15 minutes, creating a Pickering emulsion. To further promote homogeneity in the solution, the slurry was sonicated at 35% amplitude at a frequency of 20khz for two minutes with an ultrasonicator (Model VC750, Sonics & Materials, Inc., USA). Additional solvent was added as necessary into the sonicated solution to reduce the

viscosity of the mixture. The reason for the addition of fluoropolymer within the nanocomposite formulation matrix was to reduce the surface energy and promote superhydrophobicity of the coating.^{35,36} The existence of this chemical component on the nanocomposite coating has been measured by Steele *et al.*³² in a previous investigation using the technique of backscattered electron analysis.

To create the nanocomposite coatings from this precursor solution, the slurries were spray-casted onto aluminum substrates from various spray-casting heights and air pressures and then heat cured at 100 °C for 8 hours. The aluminum substrate was placed on a motorized platform and translated in controlled longitudinal (Y axis) and lateral (X axis) motions while the air-atomizing nozzle sprayed the nanocomposite mixture above the platform. The motorized platform was controlled by two linear slides driven by stepper motors (Xslide, Velmex Inc., USA). The schematic and picture of this set-up is shown in Figure 2.1a and b, respectively. This spray-casting method was not employed by Steele *et al.*¹⁵ and was designed as an improvement to ensure consistency in the quality of the nanocomposite coatings.

The air-atomizing spray nozzle was an internal mix model (1/4JCO series, Spray Systems Co., USA) with a round spray pattern and with the capacity of approximately 2.8 liters/hour at 275 kPa air pressure. Regulated air pressure was provided by an external air compressor (3 hp, Craftsman) while the polyurethane-

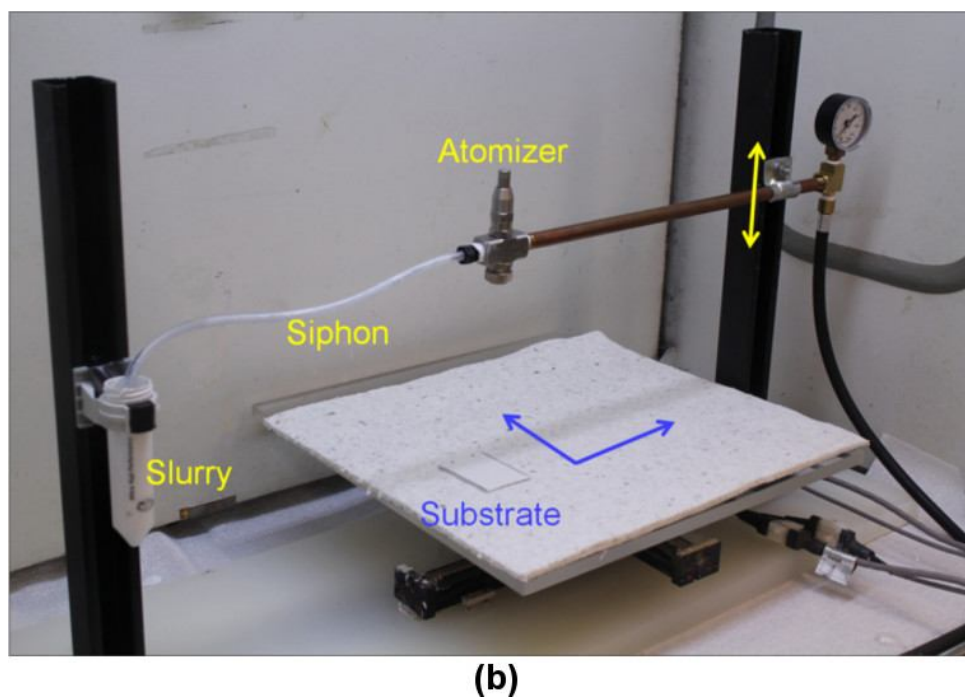
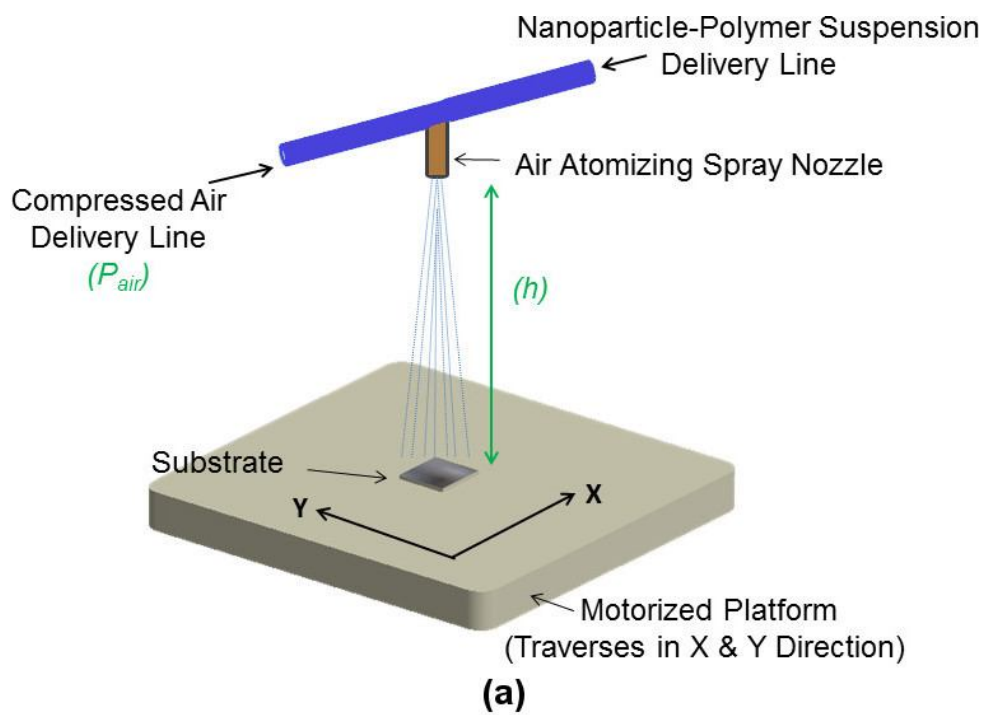


Figure 2.1 (a) Schematic of the spray-casting process and (b) image of the spray-casting set-up.

nanoclay-fluorine slurry was siphoned into the spray nozzle. The spray-casting process began when the air-atomizing nozzle was set at a fixed height and position above the substrate to deliver a fine mist of polymer-nanoclay slurry droplets. The motorized platform holding the substrate was then programmed to step in the lateral direction (X axis) for a distance of 0.5 cm before traversing in the longitudinal direction at a speed of 15 cm/second. The programmed motion was repeated until the entire substrate was coated. Various spray heights (2-16 cm) and air pressures (138-690 kPa gage) were used to create a range of nanocomposite coatings for quantitative superhydrophobic and wear durability measurements.

2.2.2 Performance Measurement

Static water CA measurements were performed by capturing three digital images of a water droplet (10 μ l volume) through a digital SLR camera (Canon EOS T2i, macro lens MP-E). The images were then analyzed using a B-spline snake approach pioneered by Stalder *et al.*³⁷ as a plug-in program within the Image-J software to provide an averaged CA measurement. ROA were acquired by measuring the tilt angle of the coating where a 10 μ l water droplet would slide off the surface. ROA measurements were also repeated five times so that an averaged ROA value could be acquired.

The surface features and texture of the coatings were imaged and measured by an optical digital microscope (Model KH-7700, Hirox) and a confocal laser scanning microscope (Model 510 Meta, Zeiss), respectively. Images acquired by the confocal microscope were then reconstructed by a surface imaging and metrology software (Mountains Map, Digital Surf) to provide a 3-D topology image of the coating representing an 800 X 800 μ m surface area as well as quantitative texture parameters such as arithmetic mean roughness, maximum peak height etc. In addition, higher magnification images of the surface features were acquired with a scanning electron microscope (6700F, Jeol).

To assess the wear durability of the coatings, a linear abraser (Model 5750, Taber Industries) was used. This device consisted of an abradant tip attached to a horizontal arm that reciprocated in a linear fashion at a force determined by weight discs. The abradant tip (H-10 Calibrade, Taber Industries) was made of aluminum oxide abrasive particles designed to provide medium abrasive action. Weight discs were placed on the mechanical arm before the abradant tip was positioned to be in contact with the surface of the coating. The nanocomposite surface was then repeatedly abraded along a linear path until the point of coating-break-through. Coating-break-through was defined as the point where the abradant tip completely wore through the coating and the underlying aluminum substrate became visible. The thickness of the coating was measured with a profilometer (Dektak 8 Stylus,

Veeco) and the thickness value was divided by the abrasion cycles required for coating-break-through. This wear rate quantifies the wear durability of the nanocomposites by describing the extent to which the coating was worn by the abradant tip (in microns) after each abrasion cycle. Abrasion trials were first conducted to determine the appropriate disc weight to be used in this experiment. This was to ensure that the number of cycles required for coating break-through was reasonable and that the experiment could be conducted efficiently. Based on these preliminary tests, 900 grams of weight discs were chosen.

2.3 Results and Discussion

Figure 2.2 shows the effect of spray-casting height on the superhydrophobicity of the coatings when spray-casting air pressure was fixed at 415 kPa gage. It can be observed that nanocomposite coatings fabricated at less than or equal to 5 cm spray-casting height were not superhydrophobic. Static water CA did not exceed 140° and roll-off angle measurements resulted in a pinned droplet on the surface. However, at 7.5 cm spray-casting height, the superhydrophobic performance of the coatings improved tremendously. Static water CA increased to nearly 160° with an abrupt decrease of ROA to approximately 8° . Further increase of the spray-casting height beyond 7.5 cm showed that coatings remained superhydrophobic, albeit with a slight reduction in superhydrophobicity.

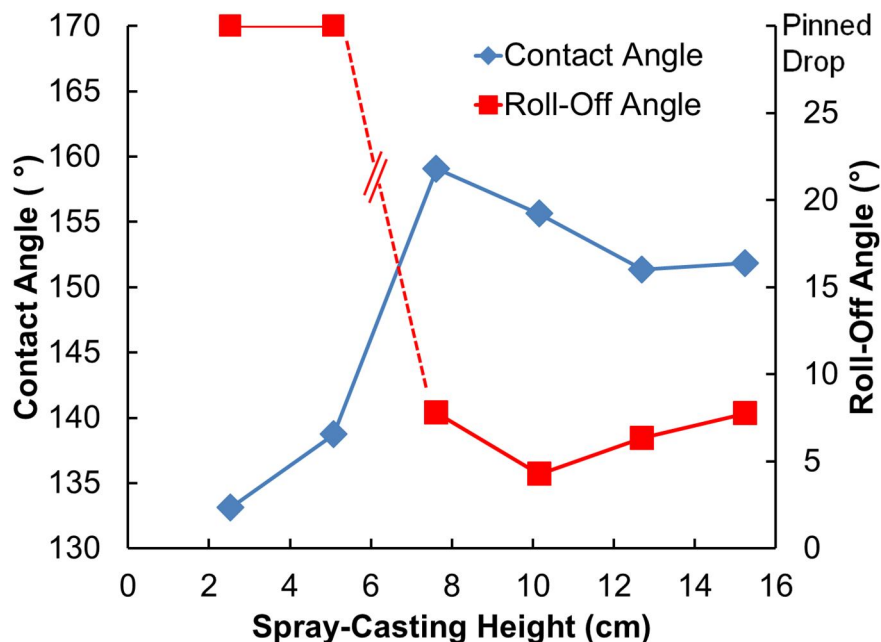


Figure 2.2 Effect of spray-casting height on superhydrophobicity of the nanocomposite coating (spray-casting air pressure fixed at 415 kPa gage).

This effect can be explained by considering the mechanism of nanocomposite formation by spray atomization. After atomization, the nanoclay-polymer suspension travels through air from the nozzle to the substrate in the form of droplets. Each of these droplets contains solvent which acts as a medium of transport while evaporating during the time of flight, ultimately leaving mainly nanoclay and polymer components on the substrate to form a nanocomposite coating. The degree of evaporation, however, is linked to the height between the spray nozzle and substrate. For a low spray-casting height (2 to 5 cm), there is insufficient time for the solvent to evaporate before the droplets impact the surface of the substrate. As such, the spray droplets remain large in size before impinging and spreading out on

the surface. This creates a “wet” coating on the substrate which allows the nanoparticles to sink and embed itself within the polymer matrix to create a smooth coating. On the other hand, at higher spray-casting heights (higher than 7.5 cm), most of the solvent evaporates during the longer time of flight, resulting in spray droplets that are much smaller in size and leaving a high concentration of nanoclay and polymer components on the substrate to form a “dry”, more porous nanocomposite coating. As the spray heights increase, until the point where at a maximum spray height of 15 cm, only a very small percentage of solvent reaches the substrate, creating a coating that is scattered with poly-disperse nanoclay particles and giving the coating a “dusty” appearance. This effect can be observed visually and is shown in Figure 2.3a and b via optical microscope pictures of coatings spray-casted at 5 and 13 cm, respectively. The significantly smoother texture presented by

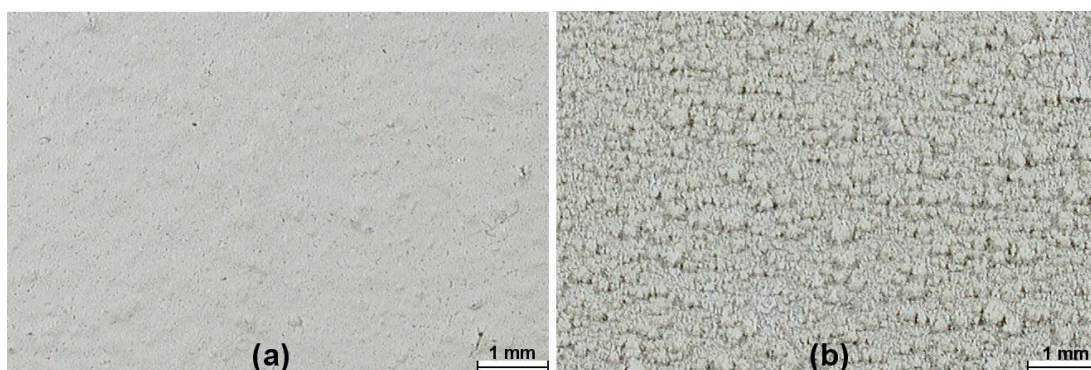


Figure 2.3 Optical microscope images of “wet” and “dry” nanocomposite coatings spray-casted at heights of (a) 5cm and (b) 13 cm (spray-casting air pressure fixed at 415 kPa gage).

the coating spray-casted at 5cm as compared to the one at 13 cm suggested a lack of surface morphology on the former coating, which itself is a crucial governing parameter for surface water repellency.³

To further investigate the surface morphology at the micro/nano scale, scanning electron microscope (SEM) images for coatings spray-casted at a height of 5 cm and 7.5 cm were acquired. As shown in Figure 2.4a, a “flatter” surface texture was observed for the coating spray-casted at 5 cm. The lack of hierarchal surface features and roughness reduces the superhydrophobicity of the coating. On the other hand, SEM images acquired at a spray-casting height of 7.5 cm (Figure 2.4b) revealed a surface texture at different length scales, with sub-micron sized features embedded within micron sized structures. The existence of this hierarchal surface structure not only promotes but also stabilizes the superhydrophobicity of the coating.³⁸

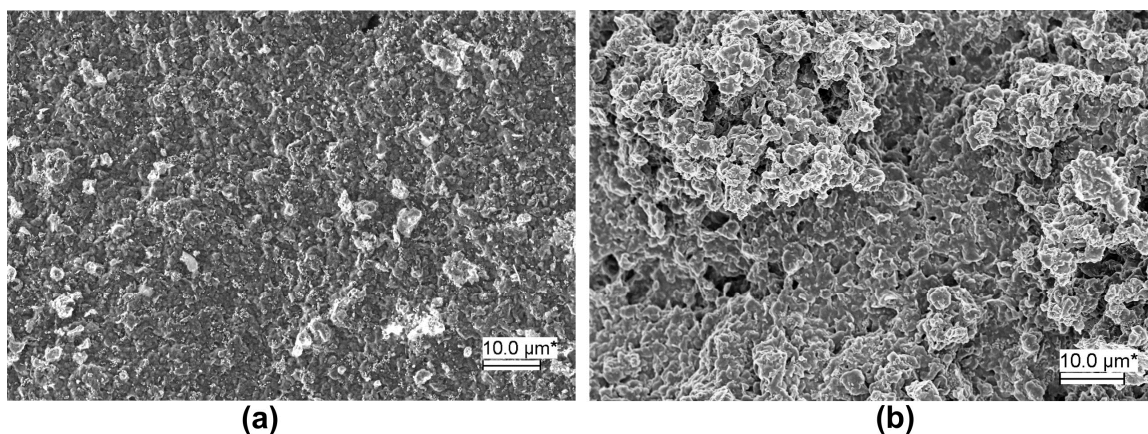


Figure 2.4 SEM images of nanocomposite coatings spray-coated at a height of (a) 5 cm and (b) 7.5 cm (spray-casting air pressure fixed at 415 kPa gage).

To quantify the difference in surface roughness between coatings spray-casted at different heights, confocal laser scanning microscope images were acquired. The acquired confocal images were then reconstructed to create three dimensional (3D) topological images representing an 800 X 800 μm surface coating area. This is shown in Figure 2.5a and b for coatings spray-casted at 5 and 13 cm, respectively. Similar

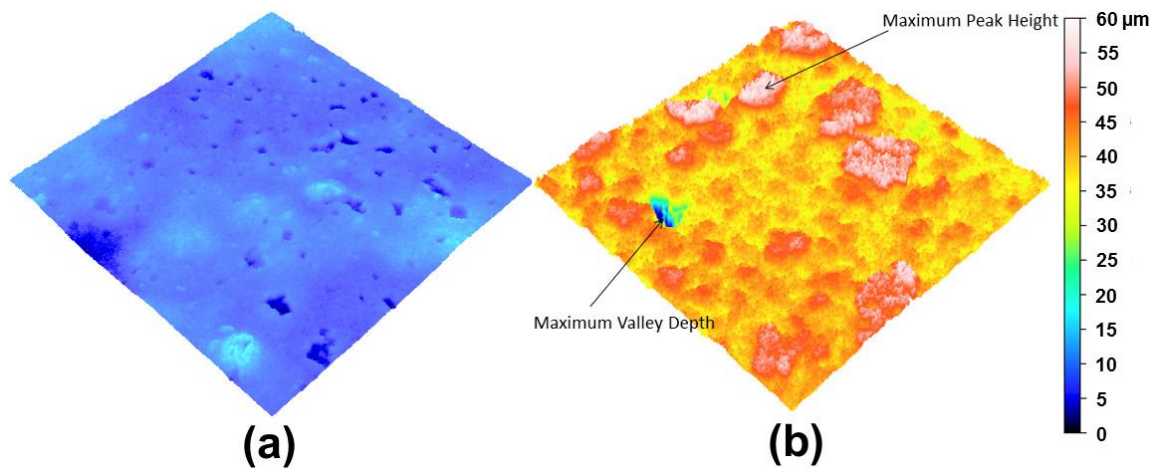


Figure 2.5 3D topological images (800 X 800 μm surface area) of “wet” and “dry” nanocomposite coatings spray-casted at heights of (a) 5 cm and (b) 13 cm (spray-casting air pressure fixed at 415 kPa gage).

to optical microscope pictures shown in Figure 2.3, significant differences in surface topology were noted, i.e., a smooth, flat texture for coatings sprayed at 5 cm as compared to a rough, porous surface for coatings sprayed at 13 cm. Quantitative surface topology measurements such as arithmetic mean roughness, maximum peak height and valley depth as well as the maximum height of the surface were derived from these images and listed in Table 2.1. Arithmetic mean roughness measurements

provided an overall measure of texture and roughness of the surface while maximum peak height and valley depth were measurements that represent the highest and lowest points on the surface. The maximum height of the surface was the sum of the highest and lowest point distances on the surface. Results from Table 2.1 showed that the arithmetic surface roughness measurements of a surface sprayed at 13 cm was approximately four times higher than a surface sprayed at 5cm. In addition, the maximum peak height and maximum valley distances and consequently the maximum height of the surface for the coating sprayed at 13 cm was significantly larger. These measurements provided quantitative validation for previous visual observations that suggest the presence of a rough, textured surface with large length scales for a coating fabricated at higher spray-casting distances.

	Coatings Spray-Casted at 5 cm	Coatings Spray-Casted at 13 cm
Arithmetic Mean Roughness (μm)	1.3	4.2
Maximum Peak Height (μm)	10.2	23.1
Maximum Valley Depth (μm)	9.6	41.4
Maximum Height of Surface (μm)	19.8	64.5

Table 2.1 Surface texture parameters of “wet” and “dry” nanocomposite coatings spray-casted at 5 and 13 cm (spray-casting air pressure fixed at 415 kPa gage).

Figure 2.6 shows the effect of spray air pressure on the superhydrophobicity of the coatings when spray height was fixed at 7.5 cm. It can be observed that at spray-casting air pressures between 140 and 415 kPa, the nanocomposite remained superhydrophobic with static water CA between 151° and 159° with ROA less than 8° . However, superhydrophobic performance degraded at a spray-casting air pressure of 550 kPa (a factor of two increase of the ROA angle) with a complete loss of superhydrophobicity for coatings fabricated at an air pressure of 690 kPa.

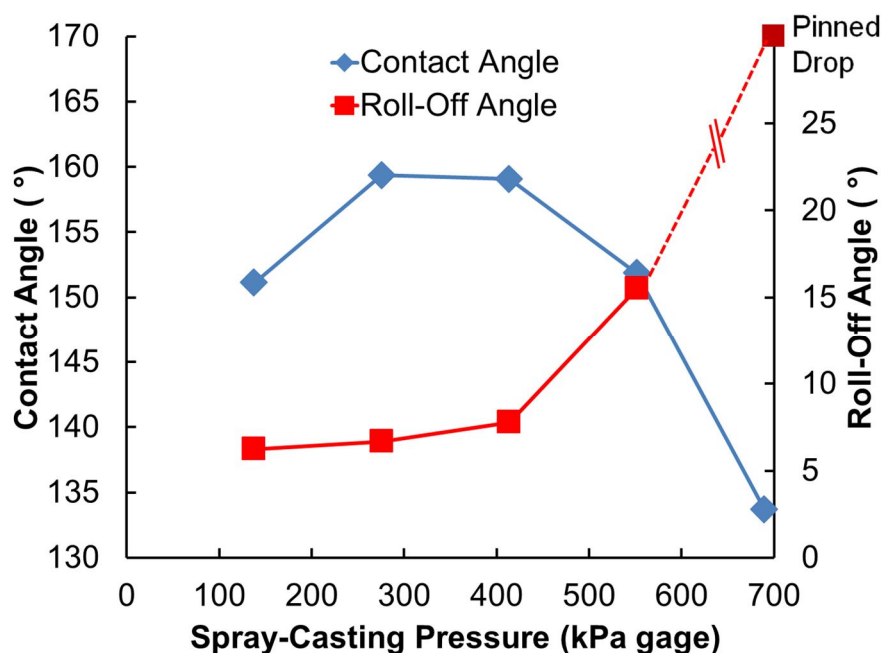


Figure 2.6 Effect of spray-casting air pressure on superhydrophobicity of the nanocomposite coating (spray-casting height fixed at 7.5 cm).

The degradation in superhydrophobicity was caused by an increase in nanocomposite volume that was also delivered at a higher speed to the surface of the substrate at high spraying pressures. Since the spraying height was fixed, there was insufficient time for the higher volume of solvent within the nanocomposite slurry to evaporate on its flight path, therefore impinging on the surface of the substrate and resulting in a coating with a “flatter” texture. This surface texture was visually similar to coatings fabricated at spray-casting heights of less than 5 cm at a constant 415 kPa gage air pressure shown in Figures 2.3a and 2.5a.

Since the superhydrophobicity of the coating is significantly influenced by the extent of droplet evaporation of the slurry as it travels from the spray nozzle to the substrate surface, the superhydrophobic performance (CA and ROA) of all coatings were plotted as a function of droplet flight time. The droplet flight time was calculated by assuming that the spray exhausted by the nozzle was a turbulent axisymmetric jet. After emission from the nozzle, the centerline velocity of this particular jet decayed in a manner described mathematically in Equation 2.1.³⁹

$$\frac{U_i}{U_c} = \frac{2}{B\sqrt{\pi}} \left[\frac{x}{D} - \frac{x_i}{D} \right] \quad (2.1)$$

where U_i and U_c are the initial (nozzle exit) and centerline velocity, respectively, D the diameter of the nozzle, x_i and x the initial and x-distances away from the nozzle, while B is a constant. The value for B was approximated to be 5.6, based on

Papadopoulos *et al.*⁴⁰ The initial centerline velocity was predicted using the Rayleigh flow relation shown in Equation 2.2.

$$\frac{P_i}{P_o} = \frac{1 + \gamma}{1 + \gamma M_i^2} \quad (2.2)$$

P_i and P_o refer to the air pressures at the exit and upstream of the nozzle, respectively, γ the air specific heat ratio, and M the Mach number. Assuming that the air flow reached sonic conditions upstream and that the pressure at the exit of nozzle was at atmospheric pressure, the initial velocity can then be prescribed as Equation 2.3.

$$U_o = \sqrt{\frac{\gamma + 1 - \left(\frac{P_{atm}}{P_o}\right)}{\left(\frac{P_{atm}}{P_o}\right)\gamma} \gamma RT} \quad (2.3)$$

where P_o is the spray-casting pressure. Therefore, by solving the ordinary differential equation of Equation 2.1, and assuming that the droplets had similar response times as compared to the air flow, the droplet flight time (t_{flight}) for various spray pressures and heights could be obtained. (Equation 2.4)

$$t_{flight} = \frac{x^2}{\sqrt{\pi DBU_o}} \quad (2.4)$$

Figure 2.7 and 2.8 shows the contact angle and roll-off angle of the coatings fabricated at various spray heights and pressures (previously shown in Figure 2.2 and 2.6) plotted only as a function of droplet flight time. It can be observed that the superhydrophobic performance curves from the different sets of spray deposition conditions coincide with each other. This confirms the previous hypothesis that the droplet flight time, hence the evaporation rate, affects the superhydrophobicity of the coating. It should be noted however that the droplet flight time is also a function of droplet size. Therefore, for more precise quantification of droplet flight time, measurements on the droplet size of the spray (by laser diagnostics) should be acquired.

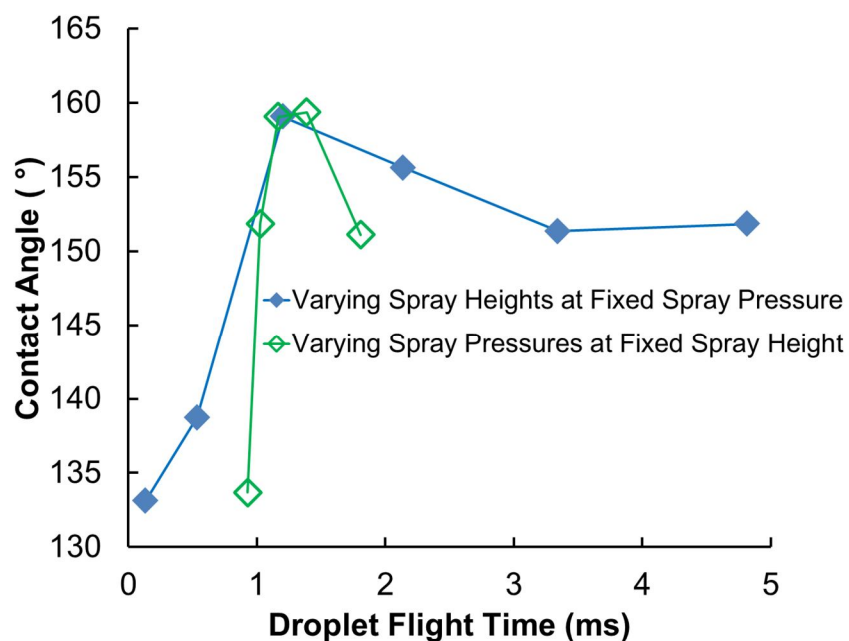


Figure 2.7 Effect of slurry droplet flight time on the CA of the nanocomposite coating.

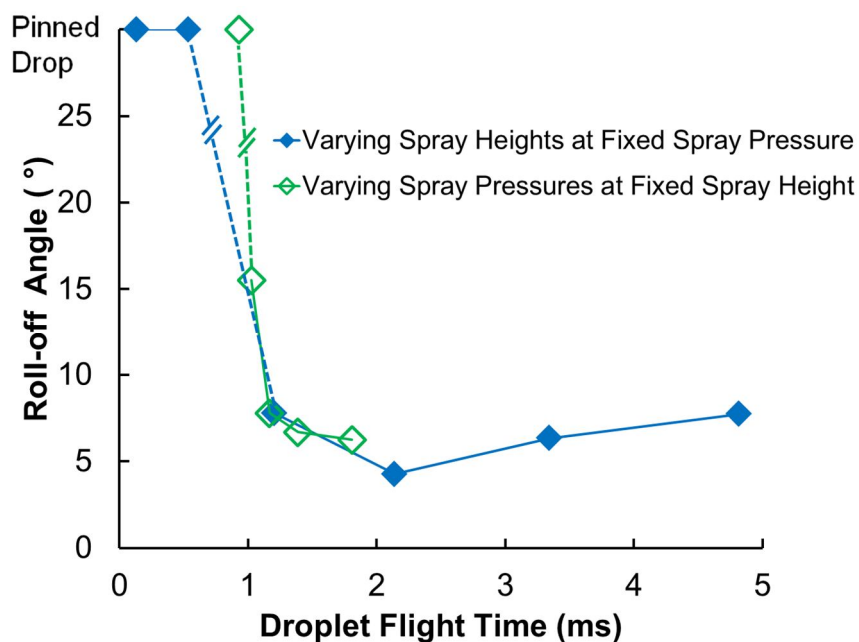


Figure 2.8 Effect of slurry droplet flight time on the ROA of the nanocomposite coating.

Figure 2.9 shows the wear durability of the nanocomposite coating over a range of spray-casting heights while fixed at an air atomizing pressure of 415 kPa gage. As observed in Figure 2.10, the coatings were repeatedly abraded by the abradant tip until the point of coating break-through. It can be observed that coatings fabricated below a spray height of 10 cm showed good abrasion resistance, with approximately 10 μm or less of the coating worn at every abrasion cycle. The most durable coating was fabricated at the lowest spray height of 5 cm, where only 800 nm of the coating was removed per abrasion cycle.

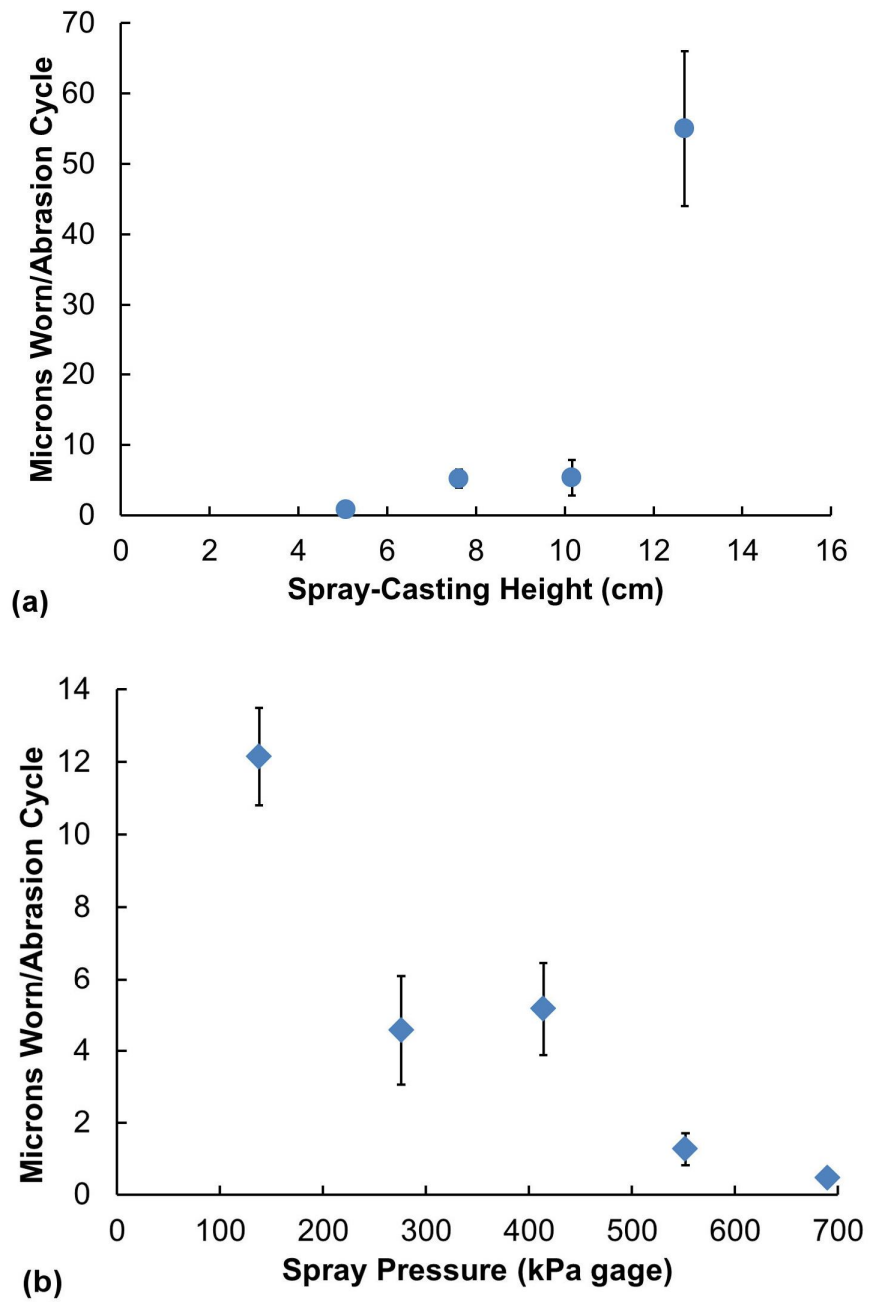


Figure 2.9 Dependence of wear rate (thickness of coating worn per abrasion cycle) on (a) spray-casting pressure fixed at 415 kPa gage and (b) spray-casting height fixed at 7.5 cm.



Figure 2.10 Image of coating (spray-casted at a height and pressure of 13 cm and 415 kPa gage, respectively) subjected to abrasion until the point of coating breakthrough.

However, once the spray-casting height was raised above 11 cm, the coating was significantly more fragile, with a durability of 55 $\mu\text{m}/\text{cycle}$, an approximately ten fold decrease in wear durability from the previous spray height. This effect shows that a “wet” coating from a low spray height is mechanically stronger than a “dry” porous coating fabricated from a higher spray height since they are less likely to suffer from the ablating effects associated with mechanical wear.⁴¹ A similar experiment was performed on nanocomposite coatings fabricated at different spray-casting air pressures while fixed at a 7.5 cm spray-casting height with similar results. Since a higher volume was delivered at a higher speed to the substrate at high spray pressures (550-690 kPa gage), a “wet” coating was fabricated, hence increasing the durability of the coating.

The results revealed the tradeoff nature of the superhydrophobicity and durability of nanocomposite coatings fabricated from a spray-casting technique, i.e., increasing the spray- height and decreasing the spray pressure (increasing droplet flight time) improves superhydrophobic performance but is accompanied by a decrease in wear durability. On the other hand, decreasing the spray height and increasing the spray pressure (decreasing droplet flight time) increases the strength of the coating but decreases its superhydrophobicity. For the formulation and spray nozzle used specifically in this investigation, the optimal composite coating should be fabricated at a spray height between 6 and 8 cm, with a spray pressure from 415 to 550 kPa gage. This set of optimal spray conditions correlate to a slurry droplet flight time of approximately 1 to 2 ms. Additional investigations have been conducted to fabricate the necessary surface roughness to achieve superhydrophobicity yet maintaining it a low roughness level so that it would be less susceptible to abrasive failures. These studies focus on changing the fluoropolymer medium and pre-treating the substrate surface as well as strengthening the chemical compatibility and stability of the combined chemical components. This will be described in Chapter 4.

2.4 Conclusions

The study of spray-casting height and air pressure effects on the superhydrophobicity and durability of polyurethane-nanoclay nanocomposite coatings indicate that coatings manufactured from a high spray-casting height were superhydrophobic. This can be attributed to the fact that a high percentage of the solvent evaporated during the spray event at these heights, resulting in a porous coating with an increased level of surface hierarchical features. At low spray-casting heights, surfaces with smoother surface textures with a lower degree of hydrophobicity were observed. A similar reduction in superhydrophobicity was observed with high spray-casting air pressures where a high volume of nanoclay-polymer mixture was delivered at a higher speed to the substrate to form a “wet” coating. Although lacking in hydrophobicity, these “wet” coatings provided a remarkably higher resistance towards abrasion as compared to a more porous coating fabricated from a higher spray-casting height or lower air pressure. By balancing these application parameters, a combination of durability and superhydrophobicity can be achieved for the specific formulation and spray nozzle used in this investigation, with a range of pressures between 415 and 550 kPa gage and at a spray-casting height between 6 to 8 cm. These parameters would serve as guidelines for the fabrication of consistent and durable nanocomposite coatings for further icing experiments described in the following chapters.

Chapter 3

Temperature & Humidity Effects

3.1 Introduction

This chapter investigates temperature and humidity effects on the static wettability of nanocomposite coatings. For a superhydrophobic coating to be ice-repellent, it has to be effective in maintaining its water-repellent characteristics at freezing temperatures as well as in an environment of varying humidity conditions. To assess this capability, numerous studies have been carried out to monitor the wettability of superhydrophobic coatings at freezing surface temperatures and at low humidity. These experiments generally demonstrated a decrease in CA and CAH as surface temperature decreases.⁴²⁻⁴⁴ It has been hypothesized that this effect is due to water condensation on the superhydrophobic surface driven by differences between surface and air temperatures. In particular, it was suggested that condensed microdroplets penetrate into the gaps of the micro and nano-structures, triggering a local

transition from Cassie to Wenzel wetting state.^{13,14} By modifying the surface chemistry and structure of the superhydrophobic surfaces, this effect can be reduced to render the surfaces “condensation resistant”.⁴⁵⁻⁴⁸ Recently, Yin *et al.*⁴⁹ studied condensation effects due to both surface temperature and air humidity and demonstrated a loss of superhydrophobicity in natural and artificial surfaces below 10°C and where relative humidity was greater than 60%. However, while the performance of a freezing superhydrophobic surface in ambient conditions is well documented, little attention has been given to the superhydrophobicity of nanocomposites in isothermal systems subjected to a temperature cycle. Questions also remain concerning the influence of “humidity history” effects on the superhydrophobic performance of the nanocomposites. These issues are of importance since the above mentioned environmental conditions are frequently encountered by aerospace vehicles.

To address the above questions, an experiment was designed to systematically measure the static water CA and ROA of a superhydrophobic polyurethane/organoclay nanocomposite surface for a full temperature cycle from 20°C to -3°C and back to 20°C at both low and high humidity conditions while maintaining homogeneous thermal conditions (equal air, nanocomposite surface and water temperatures) at each point of measurement (every 5 °C) within the specified temperature cycle.

3.2 Experimental Methods

3.2.1. Nanocomposite Coating

The nanocomposite coatings were created by first preparing a precursor solution, followed by spray casting and then thermosetting. First, dimethyl dialkyl C14-C18 amine functionalized montmorillonite clay particles (Nanoclay, Nanocor Inc., USA) were dispersed in ethyl alcohol at room temperature. Waterborne perfluoroalkyl methacrylic copolymer (PMC) (30% wt. polymer, 70% wt. water; Dupont, USA) was then added to the solution and blended with vortex mixing. Separately, a moisture-cured polyurethane (MCPU) was also dispersed in ethyl alcohol. The MCPU was a one-component liquid formula comprising of 25% diphenyl-methane-diisocyanate and 75% polyurethane pre-polymer (hexanedioic acid, polymer with 1,6-hexa-nediol and 1,1-methylenebis 4-isocyanato-benzene). Finally, the alcohol/organoclay/PMC suspension was blended into the MCPU solution, creating a Pickering emulsion. The emulsion was then spray-casted onto aluminum substrates using an internal mix, double-action airbrush atomizer (model VL-SET, Paasche). The substrates were coated with a single spray application from a distance of approximately 30 cm above the substrate for a “dry” spray and then heat cured at 100°C overnight. SEM images of the resulting nanostructures are shown in Figure 3.1.

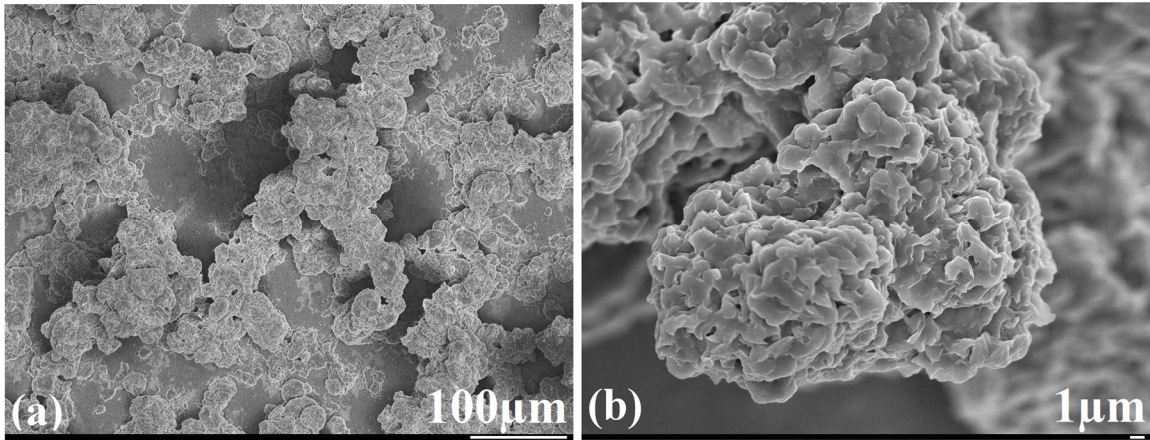
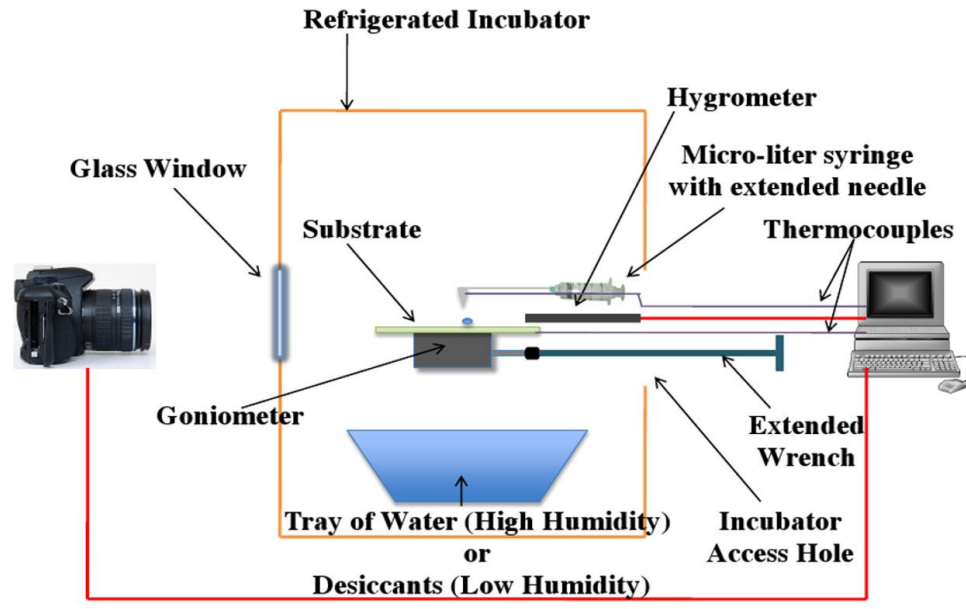


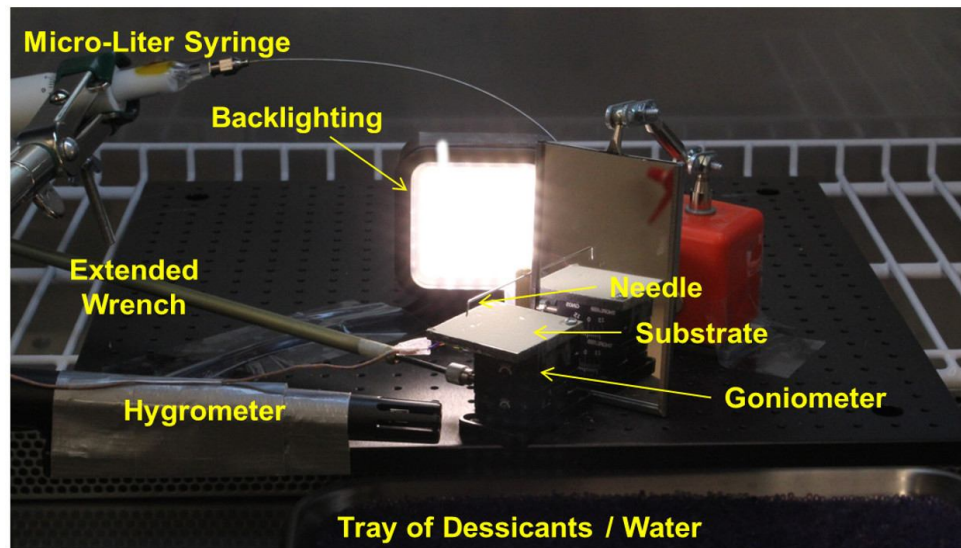
Figure 3.1 SEM images of nanocomposite coating at magnifications of (a) 200X and (b) 3000X.

3.2.1. Experimental Set-up

The nanocomposite substrate was fixed to a manual goniometer stage (GN-05, Thorlabs) and placed within a refrigerated incubator (MIR-154, Sanyo) which has a temperature range of -10°C to 60°C with an accuracy of $\pm 1.5^{\circ}\text{C}$. This setup, together with a 2 ml syringe (GS-1200, Gilmont) and thermocouples (5SRTC Type T, Omega) on the substrate and syringe, ensured that the incubator was able to provide a thermally homogeneous condition for the substrate, air and water. (Figure 3.2a and b) For high relative humidity levels, a tray of water was placed in the incubator chamber while desiccants (DX0017, EMD Chemicals) were used to reduce the relative humidity. Relative humidity (RH) levels were monitored using a hygrometer (Model 4185, Control Company), accurate to within $\pm 2\%$ RH. To ensure proper mixing of air moisture within the chamber, an independent humidity



(a)



(b)

Figure 3.2 Experimental set-up for thermally homogeneous, high and low humidity tests. (a) schematic and (b) picture of the set-up within the refrigerated incubator.

measurement at different chamber locations were conducted. Results showed less than 1% RH spatial variation within the chamber. Therefore, it was concluded that the RH spatial variations were small and not quantifiable with present

instrumentation. At each temperature/humidity point in the cycle, a 10 μL water droplet was deposited on the nanocomposite surface. Averaged water droplet ROAs were obtained by simply tilting the goniometer stage while averaged CA measurements were performed by capturing images of the water droplet on the nanocomposite surface through the incubator glass window using a digital SLR camera (Canon T2i, MP-E 65 mm macro lens) and analyzed using a B-spline snake approach developed by Stalder *et al.*³⁷ The entire data acquisition process was repeated for every 5°C until a temperature cycle (20°C to -3°C to 20°C) was completed. In addition, care was exercised to ensure that the humidity levels at temperatures during the warming cycle (-2°C to 20°C) closely resembled the humidity levels acquired during the cooling cycle (20°C to -2°C).

3.3 Results and Discussion

The averaged CA results of the low humidity experiment are shown in Figure 3.3a with the arrow representing the initial direction of the temperature cycle. It can be seen that the RH levels were consistently maintained below 20% throughout the entire temperature cycle and the CAs remained constant at approximately 160° as the temperature was reduced from 20°C to 0°C. Once below 0°C, the CA measurement decreased slightly to 154°. During the warming cycle, CAs remained

close to the measurements from the cooling cycle with no sign of path divergence.

This indicates that humidity history effects were negligible. Figure 3.3b shows that the averaged ROA across the temperature cycle also remained constant. Thus, the low humidity result indicated that superhydrophobicity was retained at low humidity conditions ($RH < 20\%$) over a wide range of surface/air temperatures.

Under high humidity conditions ($RH > 80\%$) and as shown in Figure 3.3c and 3.3d,

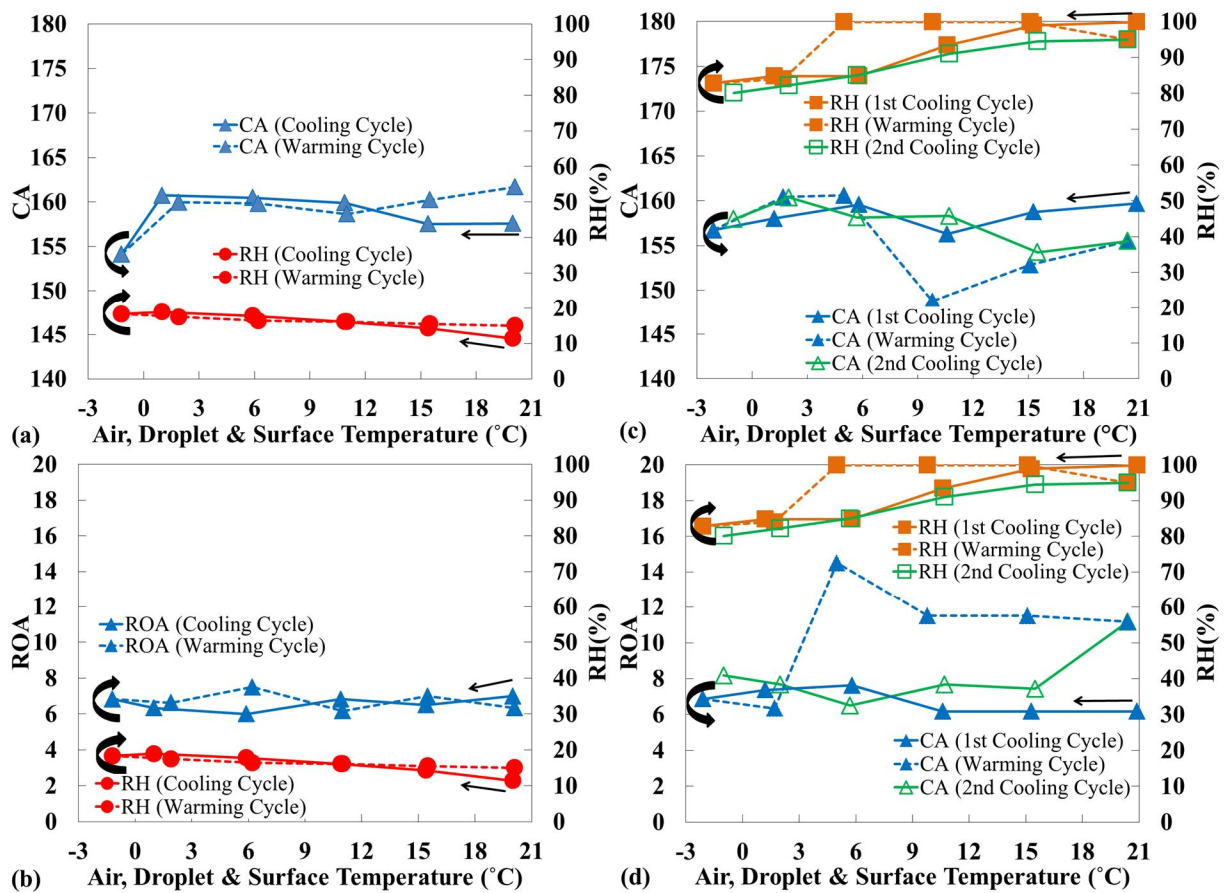


Figure 3.3 Superhydrophobic performance of nanocomposites for a temperature cycle (20°C to -3°C to 20°C) while maintaining thermal homogeneity at each point of measurement (a) CA at low RH (b) ROA at low RH (c) CA at high RH and (d) ROA at high RH.

the nanocomposite surface also maintained similar levels of superhydrophobicity with nearly constant CA and ROA values as temperature was reduced from 20°C to -3°C. These trends are substantially different than those of Yin *et al.*,⁴² Karmouch *et al.*,⁴³ He *et al.*⁴⁸ and Yin *et al.*⁴⁹ who found marked reductions in CA and CAH angles as surface temperature was reduced for both low and high humidity environments.

To understand the differences between the present high humidity results from the cooling cycle and those of Yin *et al.*,⁴² Karmouch *et al.*,⁴³ He *et al.*⁴⁸ and Yin *et al.*,⁴⁹ an additional experiment was performed. A Peltier cooling stage was set up to investigate the effect of homogeneous versus non-homogeneous thermal conditions on superhydrophobicity. To create a non-homogeneous thermal system, room temperature water droplets were placed on gradually cooled surfaces exposed to open environment ($T_{\text{air}}=22^{\circ}\text{C}$, $\text{RH}=60\%$) while CAs were measured. As shown in Figure 3.4, CAs decreased dramatically from 160° to 108° when the surface temperature was reduced from 20°C to -10°C at room temperature. In this case, when the surrounding air and droplet temperatures were held fixed, cooling the surface with the Peltier stage resulted in condensation, which was observed to significantly decrease the superhydrophobicity of the nanocomposite. This was in contrast to the cooling cycle in the incubator, where CAs remained fairly constant as temperatures of the nanocomposite, air and water droplet were homogeneously controlled by the chamber temperature even at a relative humidity over 85%. This indicates that regardless of

humidity levels, surface superhydrophobicity was generally not degraded as surface temperature decreased. Instead, superhydrophobic degradation was associated to condensation effects generally triggered by non-homogeneous thermal conditions, which caused wetting transitions from Cassie to Wenzel state.

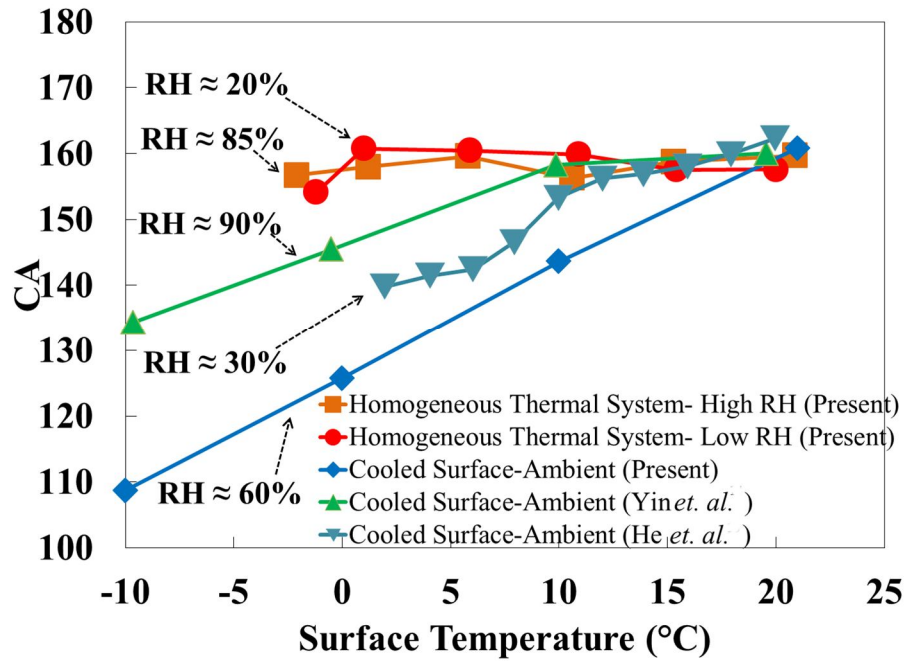


Figure 3.4 Homogeneous vs. non-homogeneous thermal effects on the superhydrophobicity of the nanocomposite coatings.

It is important to note however, that degradation in superhydrophobicity was observed during the warming cycle (from -3°C to 20°C) of the high humidity experiment. As shown in Figure 3.3c and 3.3d, while the first few points of measurement in the warming cycle closely resembled the values previously acquired in the cooling cycle, the superhydrophobicity of the nanocomposite decreased above

5°C. In particular, the ROA increased by a factor of two. This divergence from the cooling cycle measurements was coupled with: 1) visual appearance of condensation in the incubator and 2) a change in direction of the slight imbalance between air and nanocomposite surface temperature. The slight imbalance (measured to be an average of 2°C) results because the surface temperature lags behind the air temperature due to thermal inertia from the aluminum substrate, hence creating a slight non-homogeneous thermal system. In particular, the surface temperature (for RH≈85%) was above the air dew point for the first two points of the warming cycle which is consistent with the absence of condensation. However, at the third point of measurement, the imbalance between the surface and air temperature widened with the surface temperature dipping slightly below the air dew point. This result strongly suggests that condensation is the cause for the decrease in superhydrophobicity. In general however, the surface and air temperature equilibrated in about 35 minutes. To assess any additional humidity history effects after the warm up cycle, a second cooling cycle was also conducted from 20°C to -3°C a few hours after the completion of the warm-up cycle. It was observed that the previously condensed water from the warming cycle evaporated off the surface by this time. As seen in Figure 3.3c and 3.3d, no additional humidity history effects were found, i.e., superhydrophobicity resumed on the surface at CAs and ROAs consistent with the first cooling cycle. Thus it is hypothesized that condensation

effects, which result in the change from Cassie to Wenzel wetting state, are reversible.

3.4 Conclusions

In conclusion, it was shown that superhydrophobicity was maintained for a full temperature cycle of 20°C to -3°C in a low humidity environment, when at each point of the temperature cycle, the nanocomposite, air and water droplet remained thermally homogeneous. Comparable results were also observed for the cooling cycle of a thermally homogeneous, high humidity test. These results differed from those obtained from open environment experiments (in previous studies and in this study) where only the substrate was cooled while the air and water droplet were fixed at room temperature. Even small differences between the air and nanocomposite surface caused condensation which led to superhydrophobic degradation, especially at high humidity during a warming cycle.

Chapter 4

Drop Impact & Rebound Dynamics

4.1 Introduction

This chapter focuses on the study of single drop impact and rebound dynamics on an inclined superhydrophobic surface. These dynamic studies are important because the formation of ice in aerospace applications typically involve the impingement of super-cooled water droplets on freezing surfaces. Therefore, an understanding of these impact and rebound characteristics is crucial towards a successful implementation of superhydrophobic coatings as an ice mitigation tool.

In general, impact dynamics on a surface has profound implications in a wide variety of other applications such as spray-cooling of hot surfaces, inkjet printing, spray coating, precision molten drop deposition as well as in applications such as fire suppression by sprinklers, internal combustion engines and criminal forensics.⁵⁰ Therefore, it has been extensively studied for over a century using both

experimental⁵¹⁻⁵⁵ and computational tools.^{56,57} Due to recent advances in technology in high speed photography and in drop generation techniques, researchers were able to perform detailed experimental studies of impact dynamics using a wide range of drop viscosities⁵⁸⁻⁶⁰, diameters⁶¹⁻⁶³, and surface temperatures.⁶⁴ The findings from these investigations improved our understanding of the drop-surface impact process and also strengthened our capability to quantitatively predict the outcome of the impact event.

Recently, the focus of drop impact studies has shifted towards surfaces that are superhydrophobic. The water-repellency effect of these surfaces changes the dynamic interaction between the drop and the surface, particularly on the drop rebound dynamics. In general, after a drop impinges upon a hydrophilic or hydrophobic surface at low impact speeds, it tends to adhere on the substrate. However, upon striking a superhydrophobic substrate under similar impact conditions, a drop recoils, rebounds and completely releases itself from the surface. The ability of the superhydrophobic surface in promoting drop rebound has led to the hypothesis that anti-wetting coatings could be ice-repellent.

A drop's impact and rebound characteristics on superhydrophobic surfaces are governed primarily by its impact velocity and inherent liquid properties, such as density, viscosity and surface tension.⁵⁰ When a moving drop impinges on a superhydrophobic surface, its inertial energy pinches the drop on the surface, causing

the drop to spread and deform. The shape and extent of the deformation are counter-balanced by the surface tension of the drop and can be quantified non-dimensionally by the Weber number. After impingement, the inertial energy of the water drop is dissipated through viscous forces. This viscous resistance affects the drop rebound characteristics and can be quantified by the Ohnesorge number.⁵³

Numerous studies have investigated the perpendicular drop impact and rebound characteristics on a superhydrophobic surface at a variety of Weber and Ohnesorge numbers.⁶⁵⁻⁷⁰ For example, Chen *et al.*⁷¹ categorized the drop rebound outcome (partial rebound, partial rebound, splashing etc.) for Weber numbers ranging from 0 to 170 and Ohnesorge numbers ranging from 0 to 0.0028, on a synthetic superhydrophobic surface as well as on a lotus leaf. Tsai *et al.*⁷² performed an experiment to quantitatively study the characteristics of a drop impact at Weber numbers as high as 800. In addition, they also investigated drop splashing dynamics at reduced ambient air pressures. Kwon *et al.*⁷³ focused on the study of impact and wetting pressure of micro-droplets with diameters less than 50 μm on a photoresist pillar-textured surface, while Pearson *et al.*⁷⁴ utilized drops consisting of water-glycerol mixtures to qualitatively and quantitatively study the influence of liquid viscosity on impact and rebound behavior. These investigations provided detailed insight into the anti-wetting dynamic behavior of drops and, in particular, noted the various impact and rebound outcomes that could result from drop impingement at

various impact velocities and viscosities. However, these studies were all performed for impact perpendicular to the surfaces. In reality, drops tend to strike a target surface at an inclination for most applications. For example, ice accretion on a wind turbine blade as well as on an aircraft wing typically involves impact and freezing of super-cooled liquid droplets on those surfaces at sub-zero environmental temperatures. These surfaces are usually positioned at an angle of attack while in operation and hence, the impingements of super-cooled droplets on these components are also at an inclination.

There are a few studies that considered oblique drop interactions. Sikalo *et al.*⁷⁵ investigated the impact of drops on inclined hydrophilic and hydrophobic surfaces and found a back to front asymmetry in drop deformation upon impingement. Chiarot *et al.*⁷⁶ and Zheng *et al.*⁷⁷ extended the work by studying the grazing impact of high velocity, continuous droplet streams on inclined superhydrophobic surfaces. The study found that the shape and structure of the rebounding stream was a strong function of the frequency of the droplet ejection as well as its velocity. However, to the author's knowledge, there have been no published studies which have investigated in detail the characteristics of a single drop oblique impingement on a superhydrophobic surface. This area of study is of great importance since the successful implementation of superhydrophobicity on

applications such as anti-icing hinges substantially upon the drop impact and rebound dynamics at tilt.

Therefore, the objective of this study is to quantitatively study the drop oblique impact and rebound characteristics for a substantive range of Weber and Ohnesorge numbers on a 45° inclined nanocomposite superhydrophobic surface. Normal Weber numbers ranging from 9 to 67 and Ohnesorge numbers ranging 0.0018 to 0.028 were achieved by varying the drop release heights as well as using drop-glycerol mixtures. With the aid of a high-speed camera, detailed qualitative and quantitative analysis from the impact and recoil dynamics was then performed. In addition, the shape and characteristics of the drop rebound was systematically categorized in a normal Weber-Ohnesorge number regime map.

4.2 Experimental Methods

4.2.1 Nanocomposite Fabrication

As with all coatings studied in this dissertation, the superhydrophobic surface was created by spray-casting precursor solutions on aluminum substrates followed by thermosetting to produce the final nanocomposite coatings. The concept of a controlled spray-casting process as described in Chapter 2 was utilized. However, the

formulations as well slurry preparation for the coating used in this particular study were different from the ones used in Chapter 2 and 3.

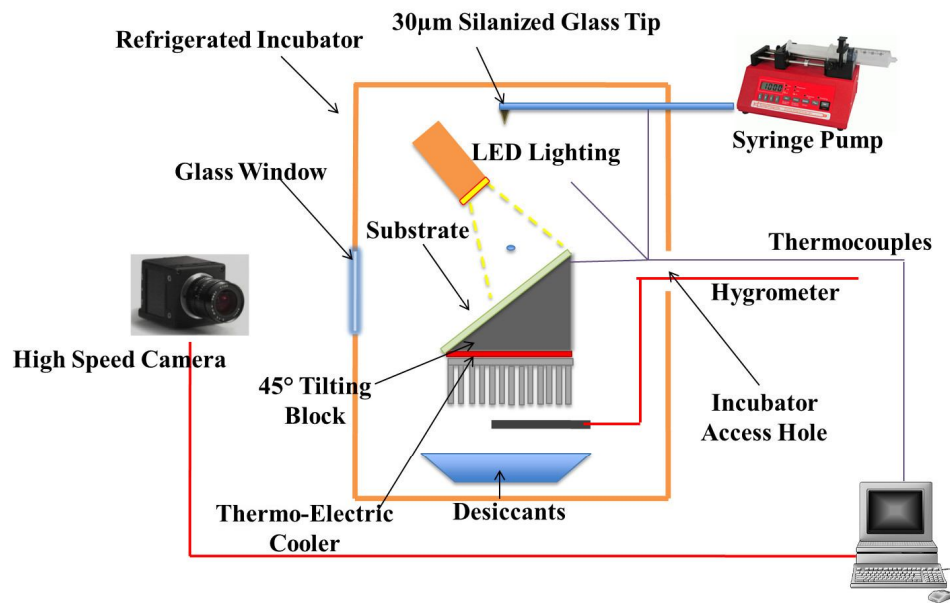
First, an aviation polyurethane topcoat (Imron AF3500; DuPont., USA) was dispersed in acetone. Next, as-received silicon dioxide nanoparticles (5-15nm particle size; Sigma Aldrich., USA) were dispersed in the polyurethane-acetone mixture. To create the slurry, waterborne fluorinated acrylic copolymer (25 weight% polymer, 75 weight% water; Capstone ST-110, DuPont, USA) was added slowly to the polyurethane-silicon dioxide suspension and blended with vortex mixing for 10 minutes, creating a Pickering emulsion. To further promote homogeneity in the solution, the slurry was sonicated at 35% amplitude at a frequency of 20 kHz for two minutes with an ultra-sonicator (Model VC750, Sonics & Materials, Inc., USA). Additional solvent (acetone) was added as necessary into the sonicated solution to reduce the viscosity of the mixture. To create the nanocomposite coatings from this precursor solution, the slurries were spray-casted from 9 cm above the aluminum substrates using an internal-mix air-atomizing spray nozzle (1/4 JCO series, Spray Systems Co., USA) driven at 170kPa. The sprayed surfaces were then heat cured at 100°C for 8 hours.

Static and dynamic contact angle measurements were performed to quantify the superhydrophobic performance of the nanocomposite coating. This was accomplished using a goniometer (model 290, Ramé-Hart, USA) and repeated three

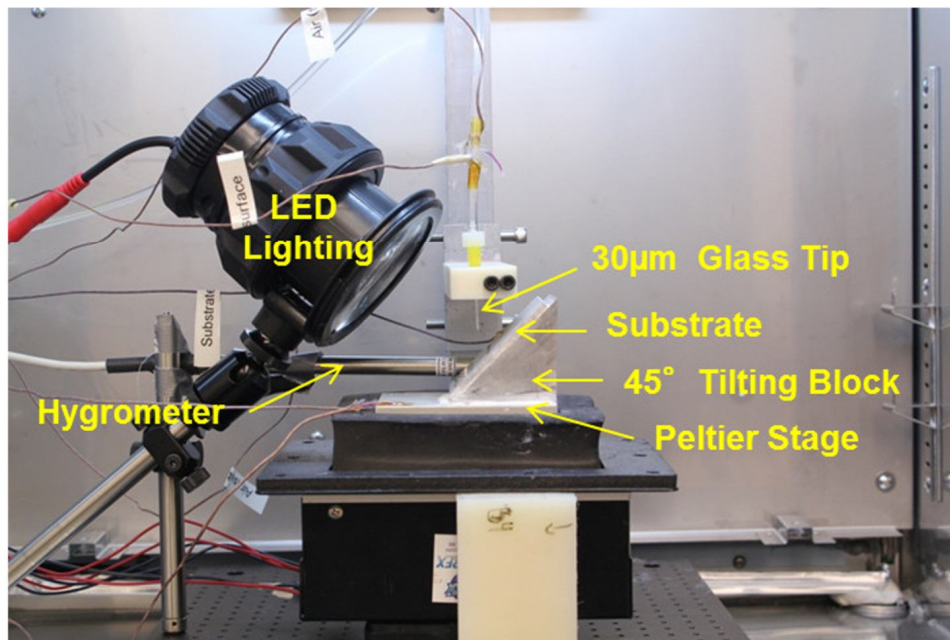
times at three different locations on the nanocomposite surface to provide averaged values of CA, ACA and RCA.

4.2.2 Experimental Set-Up

As shown in Figure 4.1a, the surfaces were placed within a microprocessor controlled refrigerated incubator (MIR-154, Sanyo) which has a temperature range of -10°C to 60°C with an accuracy of $\pm 1.5^\circ\text{C}$ and on a 45° tilting block. A pre-pulled glass micropipette with a silanized 30 μm tip (WPI, Inc.) was attached to a Tygon[®] high purity tubing and also installed within the incubator. This set-up ensured that the incubator was able to cool/warm the temperature of the air, water and impact surface simultaneously to provide a thermally homogeneous environment. A thermoelectric cold/heat plate (C60, Tellurex, Inc.) was placed in direct contact with the 45° tilting block and superhydrophobic substrate so that the surface temperature of the substrate could be more precisely controlled. Temperatures of all the components were closely monitored from attached thermocouples. In addition, desiccants (DX0017, EMD Chemicals, Inc.) were placed within the incubator chamber to reduce the relative humidity to less than 20%. The relative humidity of the chamber was monitored using a fast response hygrometer (Model 4085, Control Company, Inc.) with an accuracy of $\pm 1.5\%$ RH. The described set-up provided an isothermal, low-



(a)



(b)

Figure 4.1 Experimental set-up for single drop oblique impact test (a) schematic and (b) picture of the set-up within the refrigerated incubator.

humidity environment for the experiments to be conducted. This is imperative since non-homogeneous thermal conditions coupled with high humidity will lead to condensation on the coating. As described in Section 3.3, this triggers a wetting transition of the surface from a Cassie to a Wenzel state and ultimately causing a loss in superhydrophobicity of the coating. A picture of the experimental set-up within the refrigerated incubator is shown in Figure 4.1b.

A syringe pump (NE-1000, Pump Systems, Inc.) located outside of the incubator was connected to the tubing and micropipette, provided the dispensing force needed to accurately release water or water-glycerol drops of desired sizes onto the surface of the substrates. The drop sizes dispensed with this experimental set-up were within the range of 1.3 to 1.9 mm in diameter. These drops were released at selected heights within the incubator to reach its targeted free-fall velocities right before impact on the surface of the inclined superhydrophobic coating. The determination of drop free-fall velocities at different fall distances (ranging from 5.0 cm to 30.5 cm) was based on the numerical model of van Boxel.⁷⁸ A high-speed camera (model M5, Integrated Design Tools, Inc.) with a macro lens (90 mm, Elicar) was used to capture the drop impact and rebound sequence through the glass window of the refrigerated incubator and at a frame rate of 1250 frames/s. The resolution of the acquired images was 512×224 pixels. A picture depicting the set-up of test apparatuses outside the refrigerated incubator is shown in Figure 4.2.

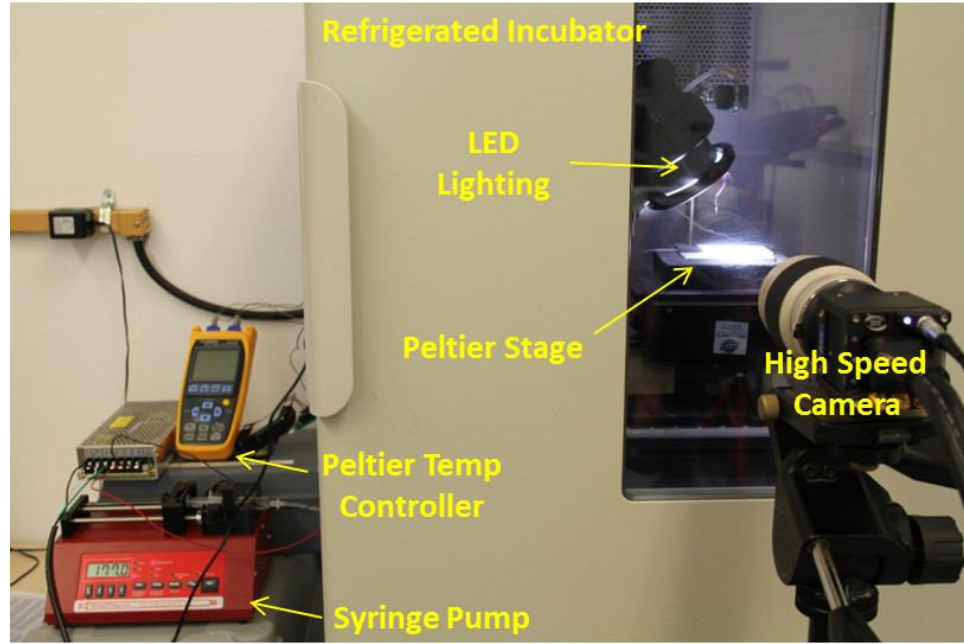


Figure 4.2 Set up of experimental apparatuses outside the refrigerated incubator.

4.2.3 Test Conditions

The test conditions were defined based on the key non-dimensional parameters conventionally cited for rebound dynamics⁷⁹: the Weber number and the Ohnesorge number. Since the droplet impacts herein are oblique, one may define the Weber number in terms of either a normal impact velocity (V_N) or a tangential impact velocity (V_T) as

$$We_N = \frac{\rho_P V_N^2 d}{\sigma} \quad (4.1)$$

$$We_T = \frac{\rho_P V_T^2 d}{\sigma} \quad (4.2)$$

where ρ_p , d and σ are the density, diameter and surface tension of the drop, respectively. These dimensionless parameters describe the balance of drop inertial forces (normal and tangential) with surface tension forces. A drop with a Weber number much greater than unity is expected to have substantial shape deformation since its surface tension will be relatively weak.

To include effects of viscosity, one may introduce the Ohnesorge number defined as

$$Oh = \frac{\mu_p}{\sqrt{\rho_p \sigma d}} \quad (4.3)$$

where μ_p is the viscosity of the drop, respectively. While this parameter is generally less than unity, even small values have been shown to indicate the influence of viscous stresses. Note that one may also define an impact Reynolds number based on the ratio of $We^{1/2}/Oh$. For the present tests, drop heights and drop liquids allowed a range of normal Weber numbers from 9 to 67 and Ohnesorge numbers from 0.0018 to 0.028 (and a commensurate range of impact Reynolds numbers from 413-2357). To achieve the above range of Ohnesorge numbers with water (and to determine if impact properties deviated significantly at sub-zero temperatures), the experiments were conducted in an isothermal environment where air temperatures were varied between -5°C and 50°C. The super-cooling of water below 0°C was made possible by using deionized water and passing them through high purity tubing which reduces

the level of impurities within the fluid, hence diminishing the possibility of heterogeneous ice nucleation once at freezing temperatures. Further increases of the Ohnesorge number was made possible by utilizing drops consisting of water-glycerol mixtures. These liquids were specifically chosen to achieve high viscosity yet retaining surface tensions similar to that of water. Thus, one may expect that such liquids will have similar CA values. This prediction was confirmed to be correct when CA measurements of all the test liquids yielded consistent values ranging between 155° and 160° . The water-glycerol mixtures were prepared by adding 99.5% glycerol to deionized water at weight percentages from 27% to 55%.⁸⁰ The combination of water heating/cooling and water-glycerol mixtures provided a set of test liquids with eleven different levels of viscosities ranging from 0.5 to 8.4 cP. The properties for this set of liquids under the present temperature test conditions are listed in Table 4.1 with values of viscosity, surface tension and density from previous studies.⁸¹⁻⁸³

	Water					Water Glycerol Mixtures					
% wt of Glycerol	0	0	0	0	0	27	32	37	47	50	55
Temp ($^\circ\text{C}$)	50	25	10	0	-5	20	20	20	20	20	20
Viscosity, μ (cP)	0.547	0.890	1.307	1.792	2.144	2.28	2.74	3.35	5.32	6.00	8.40
Surface Tension, σ (mN/m)	67.90	71.97	74.30	75.71	76.37	70.47	70.12	69.78	68.93	68.66	68.22
Density, ρ (kg/m^3)	988.0	997.1	999.8	999.8	999.0	1065.0	1078.0	1091.4	1118.2	1126.3	1140.1

Table 4.1 Viscosity, density, surface tension and temperature values of test liquids used in the present experiments.

To complete the test matrix characterization, the ACA and RCA of all the test liquids were measured at room temperature on the nanocomposite surface. In general, the CA and ACA were very similar for a given liquid and temperature. For the example case of water drop, the CA was measured to be 160° while the ACA was measured to be 163° . In fact, the ACA values for all the test liquids are about 160° as shown in Figure 4.3, which is consistent with keeping the surface tension of all the liquids approximately constant (to within 10%). This allows a fair and consistent assessment of the drop impact characteristics on the surface since they are substantially influenced by liquid surface tension (as indicated by the definition of Weber number). For the rebounding aspects of the drop impact, it is hypothesized that RCA and CAH can be important. For the water drop, the receding angle was measured to be 152° , yielding a CAH of 11° . This indicates that the nanocomposite surface was indeed superhydrophobic in terms of both CA and CAH. For the other liquids, Figure 4.3 shows that the receding angles decreased as drop viscosity increased. For example, the drop composed of 55% weight percentage water-glycerol mixture, yielded a receding angle which was 30° lower than the receding angle of a water drop.

Finally, a control hydrophilic surface was employed for comparison to the superhydrophobic surface. The hydrophilic surface was simply an aluminum substrate coated with the same polyurethane binder in the fabrication of the

nanocomposite superhydrophobic coating. The resulting polyurethane topcoat on aluminum yielded a static contact angle of 68° for a water drop.

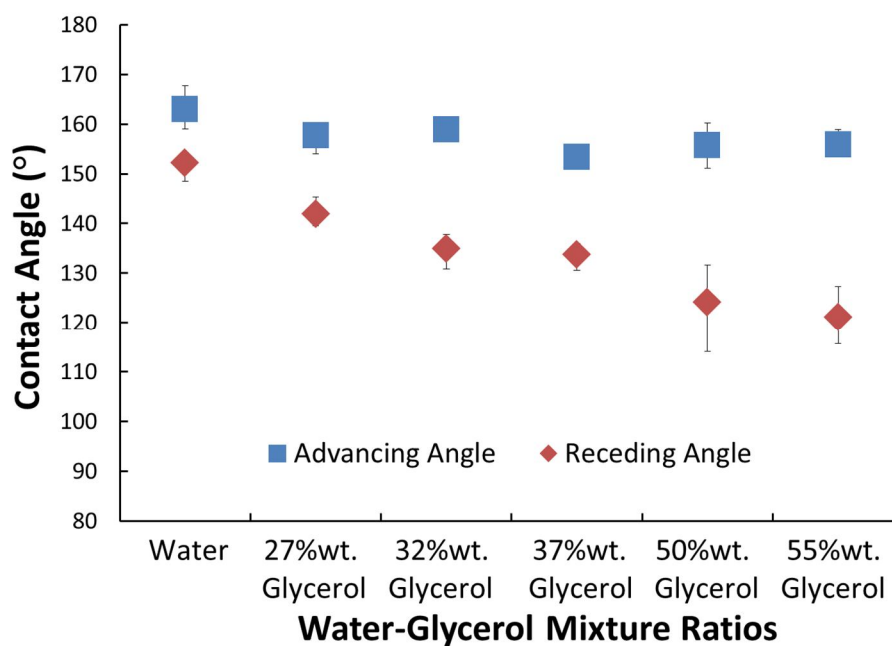


Figure 4.3 ACA and RCA measurements of the nanocomposite superhydrophobic surfaces for water and water-glycerol solutions at different viscosities.

4.3 Results and Discussion

Figure 4.4a shows the high speed images of a 1.3 mm diameter water drop at room temperature impinging on the inclined surface with the hydrophilic coating and the superhydrophobic coating. In each case, the series of images represents key events during the drop impact sequence. For the hydrophilic coating (Figure 4.4a), the drop sequences are categorized into five stages: 1) pre-impact, 2) collision, 3)

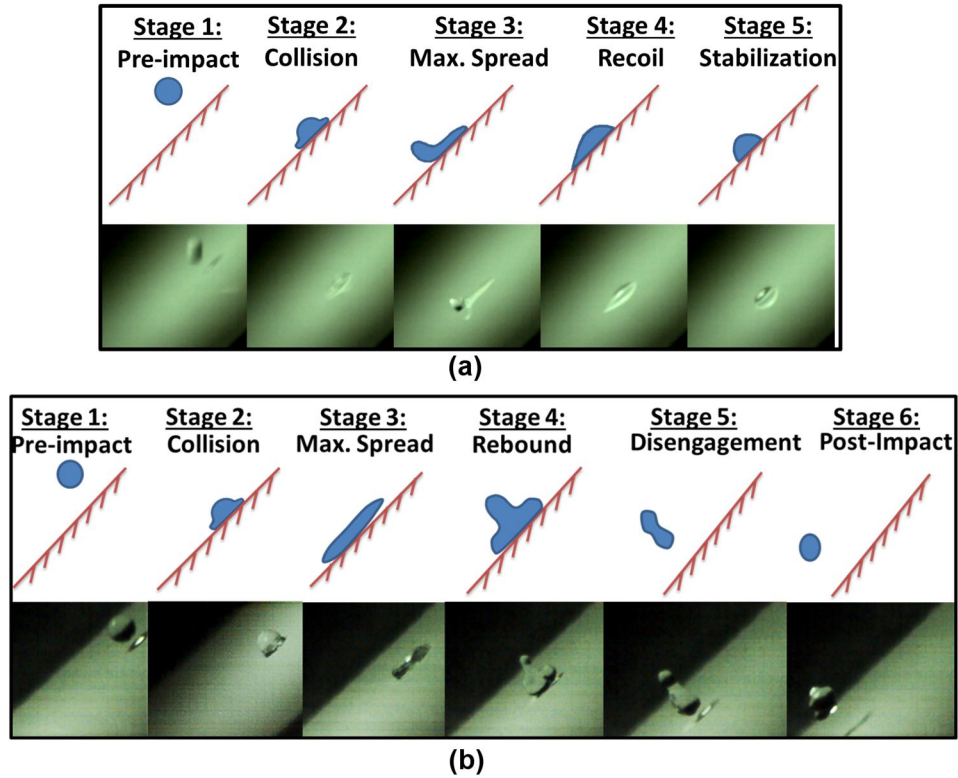


Figure 4.4 Categorization of water drop impact and rebound stages on an inclined (a) polyurethane topcoat surface ($We_N=11.5$) and (b) nanocomposite superhydrophobic coating ($We_N=23$).

maximum spread, 4) recoil, and 5) stabilization. Sketches of the drop shapes during these stages are also shown (above the photos) in Figure 4.4a. It can be observed that after the collision (Stage 2), the drop spreads on the surface (Stage 3) in an asymmetrical fashion, creating a bulge at the leading edge of the drop while leaving a thin trail of water at the back end, a phenomenological characteristic which was also observed by Šikalo *et al.*⁷⁵ This was due to high surface energy of the surface, which pinned the upstream part of the drop on the surface while the downstream side was driven down the inclination by kinetic energy associated with the tangential

component of impact velocity. The impact energy was then dissipated by a recoil motion (Stage 4) before eventually stabilizing (Stage 5).

The interaction of an impacting water drop on an inclined superhydrophobic surface is drastically different for the latter stages (stage 3 onwards) as compared to an inclined hydrophilic surface discussed above. As shown in Figure 4.4b, the drop impact and rebound sequences on the superhydrophobic surface could be categorized into six stages. 1) pre-impact, 2) collision, 3) maximum spread, 4) rebound, 5) disengagement and 6) post-impact stages.

The maximum spread stage occurred when the drop impinged and deformed to its largest extent along the surface (with length L_{max}). The rebound stage began the instance the drop receded from its maximum spread and ended when the drop was released from the surface, which correlates to the Worthington Jet formation.^{51,52} The drop would subsequently move into a transient stage called the disengagement stage. This stage typically existed for very short periods of time (~1-2 ms) and was often associated with complex shape dynamics. Finally, the drop transitioned into a post-impact stage. It should be noted that these six stages of impact and rebound sequences involved drop travel in both the vertical and horizontal direction. The drop slid on the surface while transitioning between stages 3 and 4 and travelled continuously down the inclination and away from its point of impact. In fact, the drop slid a distance of approximately five drop diameter lengths

over the contact period (i.e., between collision and disengagement). This is in contrast to an impact on a flat superhydrophobic surface where drops would impinge on a specific point on the surface and release from the same point on the surface.

Based on these phenomenological observations, the analysis of the impact and rebound dynamics on the inclined superhydrophobic surface are focused on: a) contact time and maximum spread and b) rebound outcome classifications and regime map.

4.3.1 Drop Contact Time & Maximum Spread on Surface

The drop contact time on the inclined superhydrophobic surface (τ_{cont}) was defined as the total time the drop was in contact with the surface, i.e., from collision to disengagement (Figure 4.4b). Richard *et al.*⁸⁴ studied these times for water drops impacting on a superhydrophobic horizontal surface and found that they scale closely with the drop capillary time scale (τ_{cap}) defined as

$$\tau_{cap} = \sqrt{\frac{\rho_p d^3}{\sigma}} \quad (4.4)$$

Figure 4.5 shows the contact times for the water and water-glycerol drops on the present inclined surface against the drop capillary time scale. The results showed that the contact time of both the water and water-glycerol mixture drops on an inclined surface corresponded reasonably well with measurements of drop contact

times for water drops on a horizontal surface. The linear curve fit for the water drops was within the range of experimental error (± 0.8 ms) of Richard's curve fit. This showed that the contact time was approximately equal to the capillary time scale ($\tau_{cont} \sim \tau_{cap}$) and independent of drop velocity as well as surface inclination. This result is somewhat surprising in the context of some of the other rebound characteristics to be described below where angle of inclination will influence drop spread and drop viscosity will dramatically change rebound dynamics. However, this result is consistent with a simple spring-like mechanism to describe the kinetic energy of the drop during impact as noted by Richard *et al.*⁸⁴ It should be noted

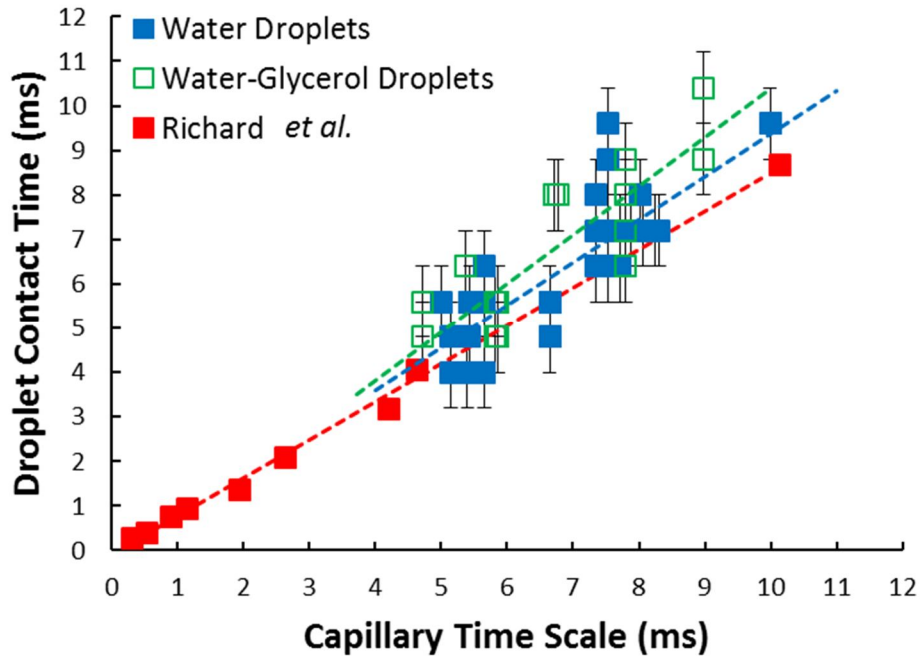


Figure 4.5 Drop contact times of all liquid drops at different viscosities on a superhydrophobic surface as a function of capillary time scale, where data from Richard *et al.* is for normal impacts and present data are for oblique impacts.

that the linear curve fit for water-glycerol mixture drop contact times (green dashed-line) diverged slightly from the water drops curve fit (blue dashed-line) which also diverged from Richard's⁸⁴ fit for normal impact (red dashed-line). This first difference may be attributed to the effect of receding angle and/or viscosity, while the second difference may be attributed to the effect of inclination. The mechanism for these subtle differences will be addressed later on. It should also be noted that the super-cooled drops impacting a surface below freezing did not nucleate, as they had a finite contact time and did not crystalize even in this unstable thermodynamic state.

Figure 4.6 shows the relationship between the non-dimensional maximum spread (L_{max}/d) of drops and its normal Weber number for all test liquids as well as measurements on horizontal surfaces acquired by Comeau *et al.*⁶⁷ and Clanet *et al.*⁶⁸. The result show a rise in maximum spread for current inclined and previous horizontal studies as We_N increases, regardless of drop viscosities. This was expected since the initial spreading of the drop is controlled primarily by kinetic energy redirection while its rebound will be more affected by viscous effects. However, the oblique impact measurements tend to diverge from the normal impact results for $We_N > 30$. The reason for this divergence is ascribed to asymmetric effects that stretch the drop in a downward tangential direction, thus promoting the spread of

the drop. Consideration of the rebound dynamics, as discussed below, would however indicate that the inclined case requires special consideration.

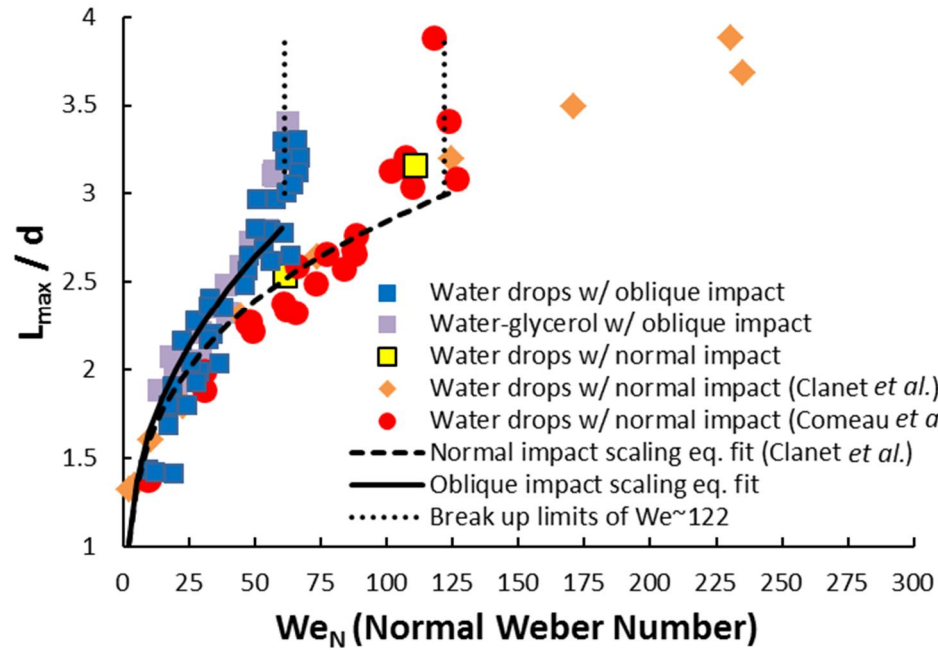


Figure 4.6 The relationship between non-dimensional maximum spread of drops on superhydrophobic surfaces with normal Weber number, comparing drops at various viscosities impacting on an inclined surface with water drops on a horizontal surface from current data as well as from Comeau *et al.* and Clanet *et al.*

To investigate the differences of oblique and normal impact and rebound properties at high Weber numbers, additional tests were considered with the surface kept horizontal. Two horizontal cases were investigated, one with the same We_N and one with the same impact Weber number (We) as an oblique impact. The high-speed images obtained from these two cases are shown in Figure 4.7. It can be observed that the maximum spread of the drop (which occurred at a time of 3.2 ms) for the

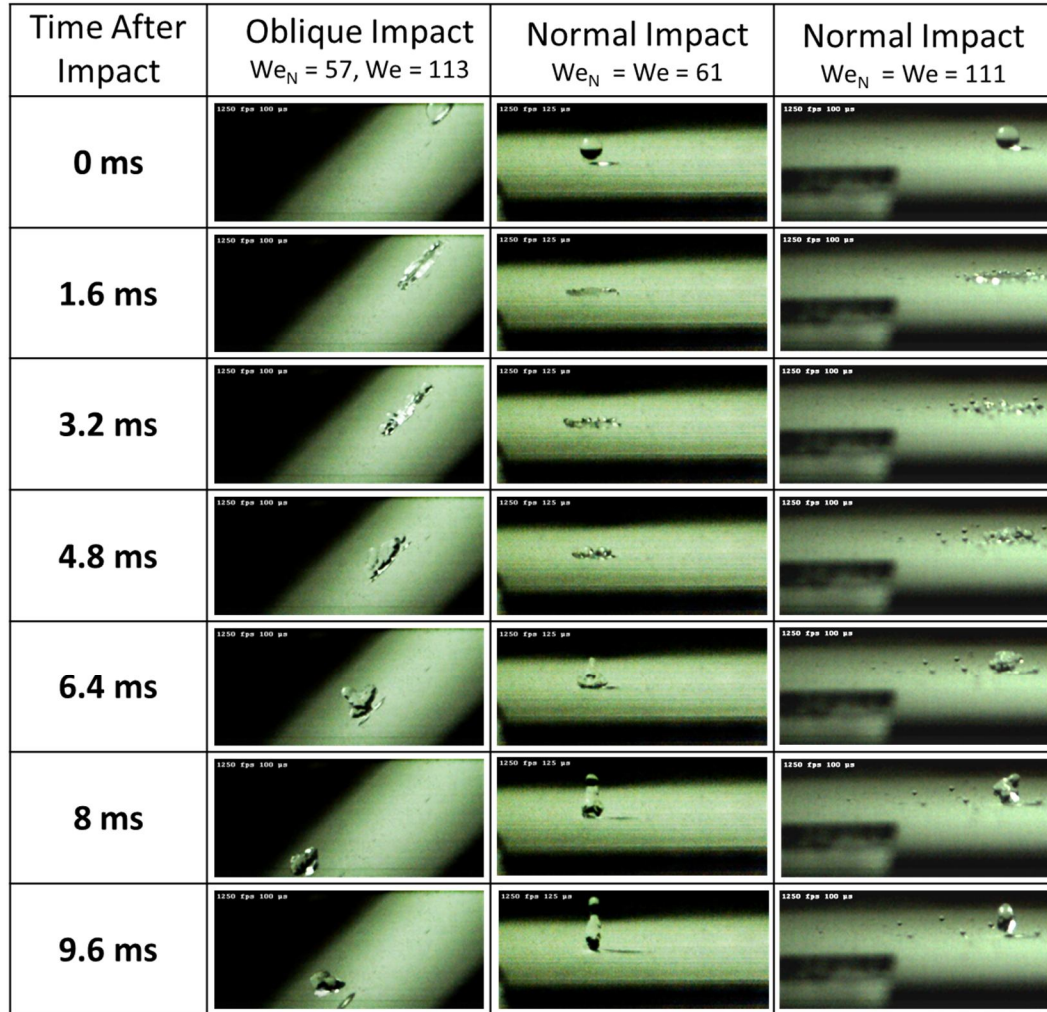


Figure 4.7 Comparison of high-speed images acquired for a water drop impact and rebound on an inclined superhydrophobic surface at $We_N=57$ and $We=113$, horizontal superhydrophobic surface at $We=We_N=61$ and horizontal superhydrophobic surface at $We = We_N = 111$.

oblique impact case more closely matches the horizontal case with a similar We_N of 61. However, as shown in Figure 4.6, the measurement of the drop maximum spread for this horizontal impact case showed a correlation with the normal impact scaling equation fit by Clanet *et al.* as well as measurements performed by Comeau *et al.*, a divergence that was consistent when normal Weber number is employed. As

expected, due to its high inertial energy from the impact velocity, the impingement of the horizontal case of $We=111$ in Figure 4.7 resulted in an immediate break-up upon contact with the surface. The drop maximum spread for this impact condition also coincided with measurements obtained by Comeau *et al.* (Figure 4.6). On the other hand, the rebound outcomes for the oblique impact case were found to be different than either of the horizontal impact cases. For example, at $t=6.4$ ms, the oblique and normal impact cases with We_N of about 60 both show a similar Worthington jet rebound.^{51,52} However, by 9.6 ms, the outcomes are significantly different among all three cases (full rebound for the oblique impact case, but jetting or break-up for the normal impact cases). These rebound dynamics were investigated and discussed extensively in the next section.

Since the conditions for $We_N > 30$ indicate tangential momentum effects may be important, one may seek to relate the influence of the tangential velocity of the droplet spread. A first order influence can be obtained by assuming that the spreading period is half the contact time and that the spreading velocity is equal to the impact tangential velocity. The net shift can be then expressed as $\Delta_{LE} \approx \frac{1}{2} \tau_{cont} V_T$. If this shift is normalized by the drop diameter and the τ_{cont} is assumed to equal the capillary time (based on Figure 4.5), the result can be expressed in terms of the tangential Weber number. If one further assumes a second order correction with a constant C_I , the square of the normalized shift can be expressed as Equation 4.5.

$$\left(\frac{\Delta LE}{d}\right)^2 \approx \frac{1}{2} We_T + C_1 We_T^2 \quad (4.5)$$

One may also apply a similar model for the trailing edge, but with a different constant (C_2). Hence, the net change of the drop maximum spread due tangential momentum is prescribed as

$$\left(\frac{\Delta LE - \Delta TE}{d}\right)^2 \approx (C_1 - C_2) We_T^2 \quad (4.6)$$

By defining C_3 as $(C_1 - C_2)^{1/2}$, the net change could be combined with Clanet *et al.*⁶⁸ normal impact equation fit shown in Figure 4.6 to give an oblique impact fit of

$$\left(\frac{L_{\max}}{d}\right) = 0.9 We_N^{1/4} + C_3 We_T \quad \text{for } We_N < 60 \quad (4.7)$$







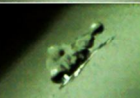




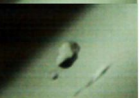

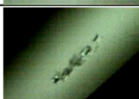


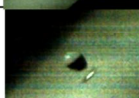

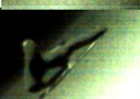


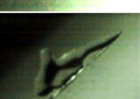


This oblique fit relates drop maximum spread for $We_N < 30$ to first order effects and We_T effects (for $We_N > 30$) as second order effects. Since the angle of inclination for this study is 45° , $We_T = We_N$. Hence, this can be applied to the data on Figure 4.6 for which C_3 was determined to be approximately 0.005 which reasonably describes the oblique results as shown by the solid line for We_N less than 60. For normal Weber numbers greater than 60, as will be shown later, the drops tend to break-up which lead to rapid increases in L_{\max}/d as shown by the vertical dotted line in Figure 4.6. It is interesting to note that the horizontal impact cases (for both present and previous experiments) did not lead to such break up, which indicates that the asymmetry introduced by an inclined surface tends to accelerate the break-up condition when

normal Weber numbers are considered. The introduction of break-up physics thereby renders Equation 4.7 to be generally invalid for higher normal Weber numbers on the 45 degree inclined surface. However, when impact Weber numbers are considered, the break-up limits for the inclined and horizontal surface (measurements from Comeau *et al.*) generally coincide at $We \sim 122$ (Figure 4.6). It should be noted though that the break-up limits could vary. For example, measurements from Clanet *et al.* did not experience drop break-up, even at a maximum impact Weber number of 235. This suggests that the break-up physics is sensitive towards the surface features and roughness of the superhydrophobic surface, a hypothesis that was also supported by Chen *et al.*⁷¹

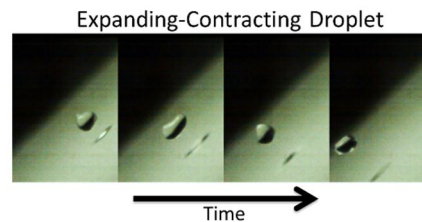
4.3.2 Rebound Outcome Classifications and Regime Map

Immediately after spreading to its maximum extent on an inclined superhydrophobic coating, a drop would recede to form a jet before disengaging and releasing itself from the surface. These rebound dynamics, which consist of stages 4-6 shown in Figure 4.4b, were a strong function of not only the impact height (Weber number) but also the liquid properties (Ohnesorge number). In particular, high-speed images acquired for the eleven test liquids impacting as drops on the superhydrophobic inclined surface revealed eight different outcome cases for the

rebound, disengagement and post-impact stages. As shown in Figure 4.8 with example images and Figure 4.9 with sketches, these outcomes were categorized as symmetric, asymmetric, irregular, irregular with breakup, bulbous, tail impingement and tail impingement with breakup.

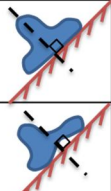


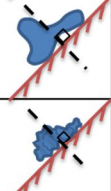


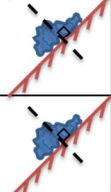


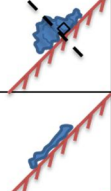

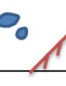



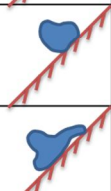


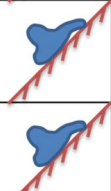


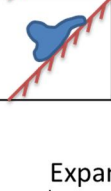


	Stage 3: Rebound		Stage 4: Disengagement		Stage 5: Post Impact	
Case 1: Symmetric	Symmetric Jet		Pillar		Expanding-Contracting	
Case 2: Asymmetric	Asymmetric Jet		Pillar		Expanding-Contracting	
Case 3: Irregular	Irregular Jet		Non-Pillar Ovaloid		Expanding-Contracting	
Case 4: Irregular with Breakup	Irregular Jet		Non-Pillar Ovaloid		Breakup	
Case 5: Immediate Breakup	Max Spread		Breakup Upon Surface		Breakup	
Case 6: Bulbous	Bulbous Jet		Non-Pillar Ovaloid		Expanding-Contracting	
Case 7: Tail Impingement	Asymmetric Jet		Elongation		Expanding-Contracting	
Case 8: Tail Impingement with Breakup	Asymmetric Jet		Elongation		Breakup	

(a)



(b)

Figure 4.8 (a) Classification of high-speed images of drop rebound, disengagement and post-impact outcomes after impingement on an inclined superhydrophobic surface and (b) sequence of images depicting an expanding-contracting drop during the post-impact stage

	Stage 3: Rebound	Stage 4: Disengagement	Stage 5: Post Impact	Symbol
Case 1: Symmetric	Symmetric Jet 	Pillar 	Expanding-Contracting 	◆
Case 2: Asymmetric	Asymmetric Jet 	Pillar 	Expanding-Contracting 	◇
Case 3: Irregular	Irregular Jet 	Non-Pillar Ovaloid 	Expanding-Contracting 	□
Case 4: Irregular with Breakup	Irregular Jet 	Non-Pillar Ovaloid 	Breakup 	×
Case 5: Immediate Breakup	Max Spread 	Breakup Upon Surface 	Breakup 	★
Case 6: Bulbous	Bulbous Jet 	Non-Pillar Ovaloid 	Expanding-Contracting 	●
Case 7: Tail Impingement	Asymmetric Jet 	Elongation 	Expanding-Contracting 	▲
Case 8: Tail Impingement with Breakup	Asymmetric Jet 	Elongation 	Breakup 	▲

(a)

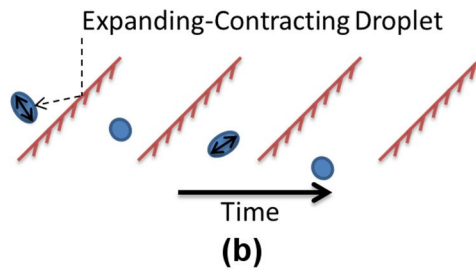


Figure 4.9 (a) Sketches of drop shapes and outcomes for the stages of rebound, disengagement and post impact based on images classified in Figure 4.9, and (b) sketches of drop shapes depicting an expanding-contracting drop during the post-impact stage.

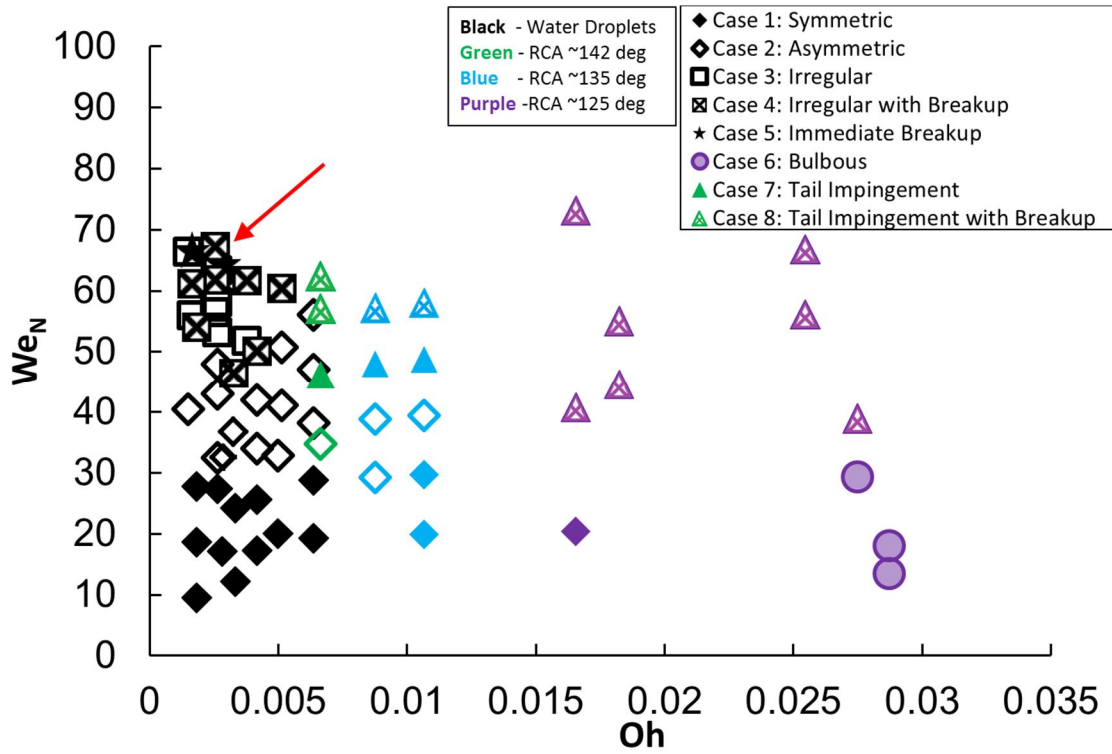


Figure 4.10 Regime map depicting the rebounding outcomes of an oblique drop impact on the superhydrophobic surface as a function of We_N and Oh , with red arrow indicating outcome variability at high We_N and low Oh

To understand the mechanisms behind these drop rebound scenarios, a regime map was plotted in Figure 4.10 in terms of normal Weber number and Ohnesorge number (similar to that of Schiaffino and Sonin⁷⁹ for normal impact outcomes). The black and colored symbols on the regime map represent water and water-glycerol mixture drops, respectively. Figure 4.10 shows that water drops with $We_N < 30$ and $Oh < 0.006$ exhibited a symmetric outcome. This case 1 outcome (as defined by first row of Figures 4.8a and 4.9a) includes a symmetric Worthington jet during rebound

leading to a pillar structure at the disengagement stage before expanding and contracting in the post-impact sequence (Fig. 4.8b and 4.9b). Due to the low inertial energy and low viscous damping, the inclination of the surface did not affect the drop rebound dynamics, a similar rebound outcome that was similar to a drop impacting a horizontal surface. However, as the impact energy relative to surface tension increased further ($30 < We_N < 45$ and $Oh < 0.006$), the effect of the surface inclination on drop rebound was more apparent resulting in the *asymmetric* outcome (Case 2 of Figs. 4.8a and 4.9a). Specifically, tangential momentum stretched the receding jet in the downward tangential direction to distort the drop in an asymmetrically. The transitional normal Weber number between the symmetric and asymmetric cases ($We_N > 30$) also coincided with the point of divergence between the drop inclined and horizontal drop spread previously shown in Figure 4.6. This confirms that tangential momentum effects become important for $We_N > 30$ on superhydrophobic surfaces. It is interesting to note that the transition between symmetric and asymmetric outcomes was observed for the super-cooled drops and for the glycerol-water mixtures to Oh values as high as 0.012.

At yet higher Weber numbers for water drop impact ($We_N > 45$ and $Oh < 0.006$), the reduced influence of surface tension allows the relatively strong inertial forces to amplify instabilities within the drop so that the drop become *irregular* in shape (Case 3) and even sometimes lead to *break up* (Case 4). As shown

in Figure 4.8a, the drop surfaces in these two cases were covered with wave-like features that would either leave the surface as a singular expanding-contracting drop or breakup into satellite drops. In general, break-up (partial or immediate (Case 5)) tended to occur for $We_N > 60$ for all Oh values on the inclined surface, which was consistent with the rapid rise on L_{max}/d as noted in Figure 4.6. However, it can also be seen that multiple outcomes for these high Weber numbers were observed at low Oh values as shown by the red arrow. In particular, three different outcomes were noted in this regime: irregular, irregular with breakup and immediate breakup. Note that a normal impact on a superhydrophobic surface generally does not result in break-up in this range of normal Weber numbers.⁶⁸ This indicates that the surface inclination substantially promotes asymmetry and instabilities that can promote break-up.

As noted in the Figure 4.10 regime map, the water-glycerol mixture drop rebound dynamics for $We_N < 40$ and $Oh > 0.006$ did not result in any immediate break-up outcomes. This is attributed to the dissipation of inertial forces by the larger viscous effects, therefore inhibiting the drop from disintegration. In addition, this regime resulted in the appearance of two other outcomes as shown in Figure 4.10: tail impingement (Case 7) and tail impingement with break-up (Case 8). These two cases are depicted in Figures 4.8a and 4.9a whereby the asymmetric jet rebound was modified to include a substantial impinged tail section which was dragged

downwards along the inclination as the drop attempted to release itself from the surface. This caused the entire drop to elongate. It would however eventually overcome this adherence and release itself either as an individual expanding-contracting drop (Figures 4.8b and 4.9b) or breakup into smaller satellite drops.

There may be a tendency to correlate the occurrence of tail impingement outcomes to the higher viscosity of the fluid, but the results at $Oh=0.06$ shows significant differences between the water and water-glycerol mixtures. As such, the difference in these outcomes is best explained by the difference in RCA (see Figure 4.3) as all other non-dimensional quantities were held approximately fixed. This decrease in RCA altered the rebounding characteristics since the ability of the surface to repel the liquid was compromised, a finding also reported by Antonini *et al.*⁸⁵ The increase in contact time shown in Figure 4.6 is also consistent with this tail impingement phenomenon, which can be traced back to a combination of decreased RCA and oblique angle impact. This observation of increasing rebound time with decreasing RCA was also noted by Antonini *et al.*⁸⁵ However, it can be seen that viscous effects are also important as demonstrated by the appearance of a bulbous shape outcome for an Oh of 0.027 (and $We_N < 30$). This same outcome did not appear for drops with a lower viscosity (Oh of 0.017) at the same RCA. While this regime map sheds new light on the impact of impact velocity, surface inclination angle, drop viscosity, and RCA, it is also clear that additional experiments (variable

drop sizes, speeds, impact angles, etc.) are needed to allow a more comprehensive assessment of the combined controlling parameters on drop outcome.

4.4 Conclusions

A detailed study on the impact and rebound dynamics of a drop at various viscosities (by heating and supercooling water as well as using water-glycerol mixtures) on an 45° inclined nanocomposite superhydrophobic was presented under isothermal conditions at a wide range of normal Weber numbers (9 to 67) and Ohnesorge numbers (0.0018 to 0.028). It was discovered that although the ACA of the water-glycerol drop stayed generally constant, its RCA decreased as the amount of glycerol in the solution increased. The impact of the drop on the superhydrophobic surface could be separated into six stages, i.e., pre-impact, collision, maximum spread, rebound, disengagement and post-impact. Drop contact times were found to be generally independent of drop velocity or surface inclination. However, due to decreased RCA, water-glycerol mixture drops experienced slightly longer contact times. Impacting super-cooled drops did not nucleate, hence the surface can be considered as ice-phobic under these test conditions.

The effect of surface inclination was more evident in terms of droplet spread and rebound outcomes. Regardless of drop viscosities, for We_N of 30 and less, measurements of the non-dimensional maximum spread of an oblique impacting drop

were found to match normal impact results from past studies. The measurements would however diverge at We_N exceeding 30. This was attributed to tangential momentum that stretched the drop downwards in the tangential direction to enhance the spread of the drop. An oblique impact equation fit for L_{max}/d was therefore proposed based on an approximation of the second order spread effects induced by the tangential momentum. However, this equation fit was found to only describe L_{max}/d for We_N of less than 60. At higher We_N conditions, a partial or immediate break-up was caused by asymmetry effects from the inclination which therefore led to a rapid increase in L_{max}/d .

The rebound dynamics from all test liquids were categorized into eight outcomes, i.e., symmetric, asymmetric, irregular, irregular with breakup, immediate breakup, bulbous, tail impingement and tail impingement with breakup. A regime map was created where these eight outcomes were plotted as a function of normal Weber and Ohnesorge numbers. It was found that both viscosity and RCA could alter a drop's rebound characteristics.

Chapter 5

Ice Adhesion Strength with a Thick “Defect”

5.1 Introduction

This chapter focuses on the ice adhesion study of hydrophobic and superhydrophobic surfaces under icing conditions typically encountered by aerospace applications. As previously described, the hypothesis of anti-wetting coatings as icephobic materials is based on the premise that water droplets will be repelled from a superhydrophobic surface in icing conditions before crystallization can occur. Although the precise definition of the term “icephobic” is still being debated among researchers, it is generally agreed that icephobicity refers to the ability of a surface to prevent ice accretion and adhesion.⁸⁶

However, to date, there have been no studies that report a complete prevention of ice accretion on a superhydrophobic surface. Cao *et al.*⁸⁷ performed an

experiment where a satellite dish was treated with a superhydrophobic composite and exposed to naturally occurring freezing rain. A significant reduction of ice accretion was observed but fragments of the ice still remained on the surface. Mischenko *et al.*⁸⁸ conducted a super-cooled drop impact study on a freezing superhydrophobic surface. The surface was able to repel the impinging drops at temperatures as low as -15°C. However, at extreme temperatures (-25°C or lower), ice accreted. Farhadi *et al.*⁸⁹ subjected several superhydrophobic coatings to a super-cooled icing cloud in a wind tunnel and discovered that ice would form on the surfaces, albeit at a lower adhesion strength. Various other investigations also exposed superhydrophobic surfaces to icing conditions and reported similar observations, i.e., ice accretion was delayed but would eventually occur after an extended period of time.^{86,90-97} One of the few cases that reported complete ice prevention involved the use of an electrical heater to assist in ice shedding on a superhydrophobic surface.⁹⁸ Therefore, it is clear from these studies that the current designs of superhydrophobic surfaces cannot inherently thwart the occurrence of ice formation.

Hence, the use of superhydrophobic surfaces as an ice mitigation tool has recently shifted from the prevention of ice accretion to the reduction of surface ice adhesion strength. This is especially relevant for aerospace applications such as wind turbines, aircraft surfaces, as well as aircraft engines. The reasoning is that, even

with the formation of ice on these surfaces, aerodynamic or centrifugal forces could potentially overcome its adhesion strength and release it from the superhydrophobic surface. Extensive studies of ice adhesion strength on surfaces have been performed since the 1950s with results revealing the capability of hydrophobic materials to reduce ice adhesion strength.⁹⁹⁻¹⁰⁶ This is due to the low surface energy of hydrophobic materials. With the recent advent of superhydrophobic surfaces, the hypothesis is that the ice adhesion strength could be further decreased on these surfaces due to the reduced liquid-surface contact area when in a Cassie wetting state.¹⁴ This hypothesis was investigated by numerous researchers with varying success. In general, a significant reduction in ice adhesion strength (lower than hydrophobic materials) was observed for the majority of investigations.¹⁰⁷⁻¹¹⁶ However, there were also a few studies that reported an *increase* in ice adhesion on a superhydrophobic surface as compared to hydrophilic samples.^{117,118} These conflicting reports are hypothesized to be due to inconsistent ice accretion processes. The majority of these studies relied on “static” methods, which involve the placement and freezing of either a drop or water columns on superhydrophobic surfaces.^{108,117,118} Although these methods do result in ice formation, they do not represent the typical process of atmospheric ice accretion, i.e., the impingement and instantaneous nucleation of a cloud of super-cooled droplets (20-100 μm in diameter) on target surfaces in freezing environmental conditions. The dynamics of these two ice

accretion processes are clearly different. In fact, “static” methods involving water columns subject the superhydrophobic surface to a hydrostatic force that cause water to penetrate into the surface micro-asperities, triggering a wetting transition from a Cassie to Wenzel wetting state and hence resulting in a stronger ice adhesion.

Researchers have also attempted to correlate surface wettability (CA, CAH, RCA) as well as surface roughness parameters of hydrophobic and superhydrophobic surfaces to ice adhesion strength. A consensus on the adverse effects of surface roughness on ice adhesion across all surfaces (hydrophilic to superhydrophobic) has been reached.^{102,104,106,111,113,119,120} However, there have been disagreements over the role of surface wettability parameters on ice adhesion strength. Some have reported that the relationship between CA and ice adhesion strength is linearly proportional,^{104,107,108,110,116} while others have failed to observe any correlations.^{97,100,117,118} Recently, these studies were extended to include dynamic angles, with Kulinich *et al.*^{97,111,112} reporting a good correlation between CAH and superhydrophobic ice adhesion. However, Meuler *et al.*¹⁰⁵ contended that the effect of RCA on hydrophobic ice adhesion was stronger than that of CAH. The inconsistencies of these reports show a lack of understanding of the effect of these various surface wettability and roughness parameters on ice adhesion strength, especially on superhydrophobic surfaces.

Therefore, the goal of this study was to conduct a comprehensive experimental investigation of ice adhesion strength on a wide range of hydrophobic and superhydrophobic surfaces in environmental conditions typical of aerospace icing. This was accomplished by accreting ice on test substrates under the impact of a cloud of super-cooled droplets at an ambient temperature of -20°C . The accreted ice was then removed from the surface *in situ* using pressurized air in a tensile direction. Ice fracture energies were then calculated and the relationships between the surface wettability and roughness parameters and ice adhesion were studied in detail.

5.2 Experimental Methods

5.2.1 Experimental Set-Up

The ice adhesion experiment performed in this study was based on an ice fracture test devised by Andrews *et al.*¹²¹⁻¹²³ It was designed to be a plane-strain, mode-1 (tensile loading), fracture toughness test. The principle behind the test is as follows: a plastic, non-adhering disc is placed on an access port of a test substrate to serve as a totally enclosed defect. Once ice has accreted on the test substrate, air pressure can be applied through the access port and on the defect for the initiation and propagation of the ice fracture.¹²² The critical pressure to the point of ice fracture is called the *fracture pressure* and can be converted to a critical energy release rate called the *fracture energy*.¹²²

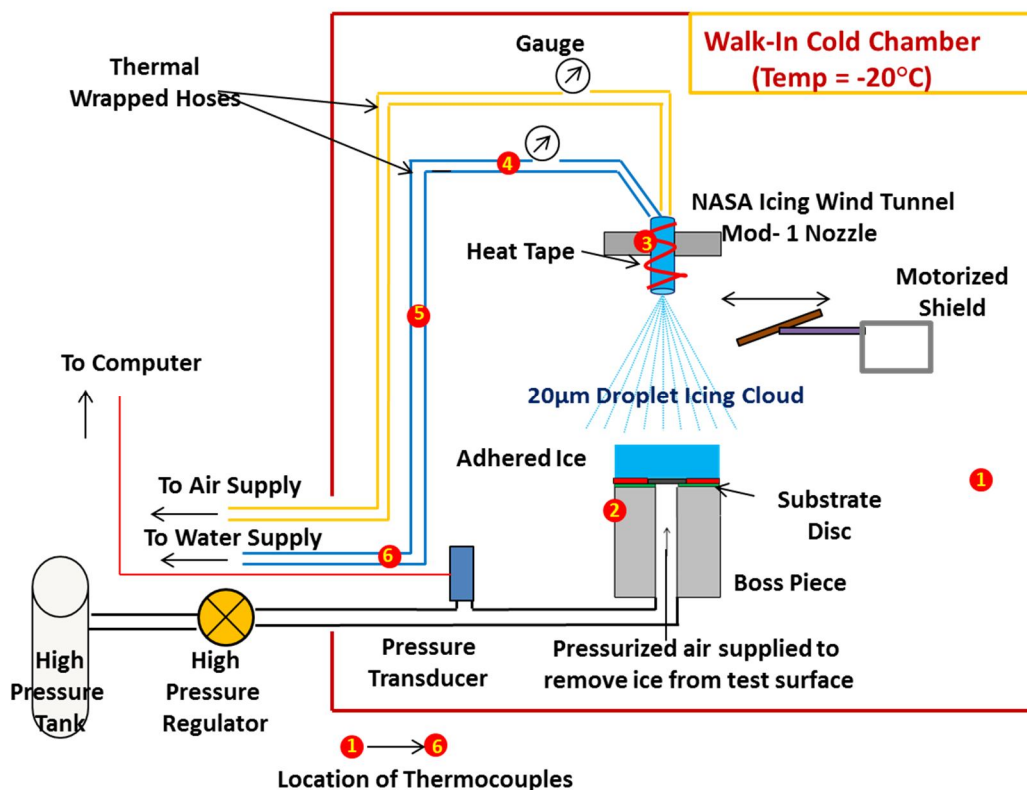


Figure 5.1 Schematic of the experimental set-up.

As shown in a schematic in Figure 5.1, an experiment was carefully designed based on the above principles. Hydrophobic and superhydrophobic coatings were applied on the surface of a substrate disc. Two types of disc substrate materials were used: aluminum and titanium alloy 6-4. The latter material is commonly used in aerospace applications due to its high strength to weight ratio and excellent corrosion resistance.¹²⁴ These disc substrates (30 mm in diameter) were attached to a supporting aluminum piece, called a boss piece either via hot melt adhesive or by screw attachments sealed with an O-ring. The whole test piece was then secured on a vertical pipe and placed in a walk-in cold chamber (Leer, USA) to be positioned



Figure 5.2 Picture of the walk-in cold chamber used in the ice adhesion experiment.

under an air atomizing nozzle. A picture of this walk-in cold chamber is shown in Figure 5.2.

The air atomizing nozzle (Mod-1) was acquired from the NASA Glenn Icing Research Facility and was specifically designed to produce a spray consisting of 20 μm diameter water droplets. It was protected by heat tape to prevent any remnants of water in the nozzle from freezing. The distance between the spray nozzle and the substrate disc was selected (78 cm) on the basis of preliminary optimization tests to determine the required height of the water droplets to super-cool before impacting the coating. This is of particular importance since the accuracy of the ice adhesion measurements depend substantially on the consistency and quality of ice accretion

on the test substrate. Deionized water (cooled separately to 5°C) and air for the Mod-1 nozzle were supplied from a water pump (PO101X, Berns Corp. USA) and air compressor (1.5 hp, Craftsman) installed outside of the cold chamber and connected to the nozzle via thermal wrapped hoses through the chamber access hole. The thermal protection is required to prevent the formation of ice within the hoses which would potentially impede the flow of air and water. The use of deionized water is also critical as impurities in the water can potentially result in a large variation in ice adhesion strength.¹²⁵ It should also be noted from Figure 5.1 that a retractable motorized shield was positioned in between the spray nozzle and the substrate disc to control the timing of spray impact on the substrates. This was to ensure that the ice would only accrete from super-cooled water at steady-state temperatures. A more detailed description of the role of this shield, as well as its method of application during the test process, will be provided in the next section. As shown in Figure 5.3, pictures of this motorized shield are shown along with the rest of the experimental set-up within the walk-in cold chamber.

Six thermocouples were attached to various locations on the experimental set-up to measure the temperature of air, substrate, spray nozzle and water tube. These locations are indicated on Figure 5.1. Once the cold chamber was cooled to -20°C, the spray was initiated at a water and air pressure of 448 kPa (65 psi) and 138 kPa (20 psi), respectively. This resulted in the accretion of ice (10 mm thick) on the

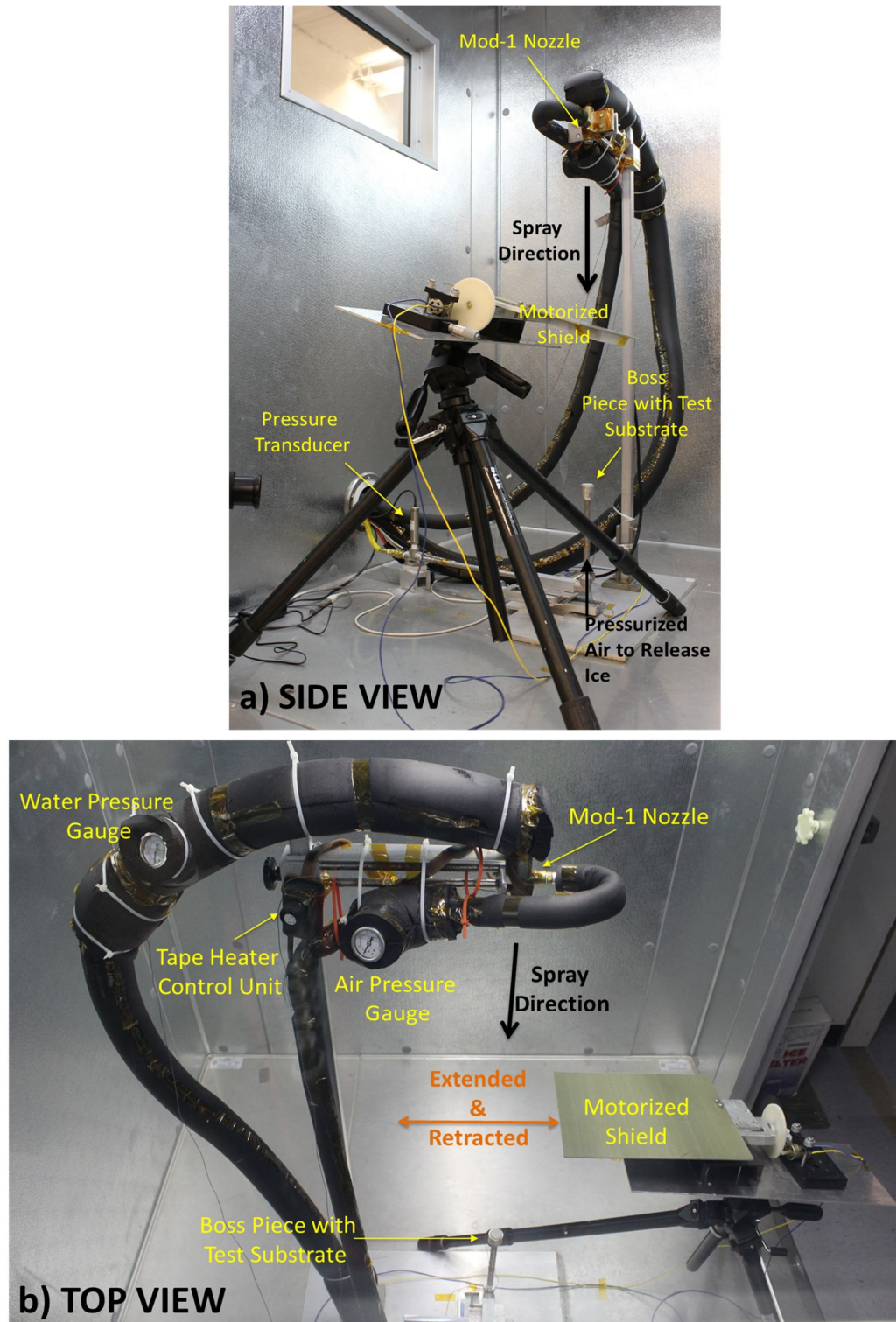


Figure 5.3 Pictures of the experimental set-up in the walk-in cold chamber. (a) side view and (b) top view.

substrate of the disc and polytetrafluoroethylene (PTFE) “defect” disc (1 mm thick, 6.35 mm diameter) which was placed on top of the substrate disc access hole. The selection of air and water pressures was based on calibration curves provided by NASA Glenn for the production of 20 μm droplets.¹²⁶ A picture of the Mod-1 nozzle and its calibration curves are shown in Figure 5.4a and b.

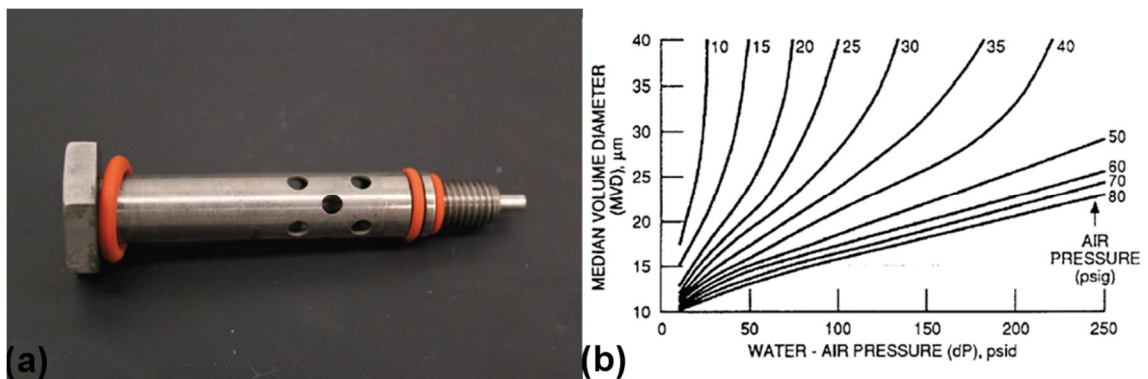


Figure 5.4 NASA Icing Wind Tunnel Mod-1 nozzle. (a) picture of the nozzle and (b) calibration air and water pressure curves of the nozzle to produce desired droplet sizes.

After the accretion of ice (10 mm thick) was completed, the ice fracture process was performed *in situ* by manually supplying pressurized air at a rate of approximately 14 kPa/sec (2 psi/sec) from a compressed air tank located outside of the freezer to the boss piece and through the hole in the substrate disc until the accreted ice was fractured and removed from the surface. This pressure was recorded via a high frequency pressure transducer as the ice fracture pressure of the substrate. A picture of ice accretion on a substrate disc is shown in Figure 5.5, along with

pictures of aluminum and titanium 6-4 substrate discs attached to their respective boss pieces prior to ice accretion. Note the placement and position of the PTFE “defect” disc on the substrates.

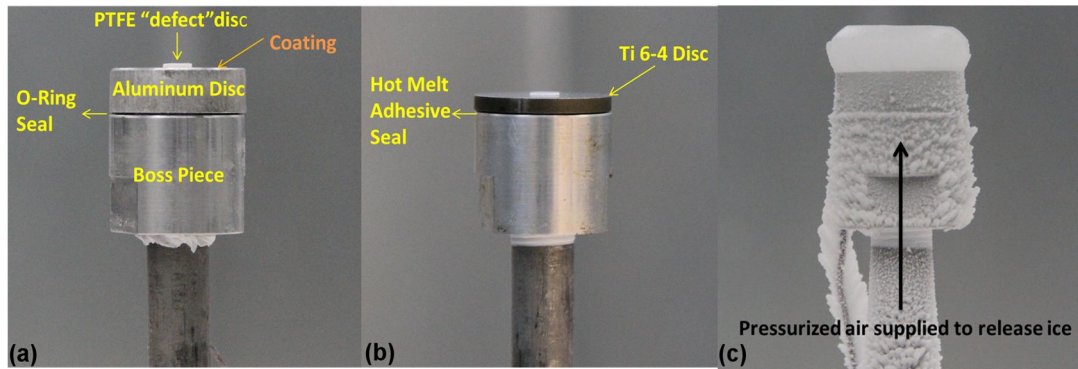


Figure 5.5 Design of the boss piece attached with test substrate discs. (a) aluminum substrate disc, (b) Ti 6-4 substrate disc and (c) ice accretion on an aluminum substrate disc.

5.2.2 Tested Coatings

The surfaces which are subjected to this ice adhesion test include substrates with a wide range of surface wettabilities and were separated into four categories: (A) control surfaces, (B) hydrophobic coatings, (C) hydrophobic surface finish, and (D) superhydrophobic coatings. These categories with their respective coatings are listed in the next page:

A Control surfaces

- i) Titanium 6-4 as-received
- ii) Titanium 6-4 shot-peened
- iii) Aluminum as-received

B Hydrophobic coatings

- i) *Luna* A1 on titanium 6-4 shot-peened disc
- ii) *Luna* A2 on titanium 6-4 shot-peened disc
- iii) *Luna* B4 on titanium 6-4 shot-peened disc
- iv) Rolls-Royce proprietary coating 1 on titanium 6-4 shot-peened disc (RR1)
- v) Rolls-Royce proprietary coating 2 on titanium 6-4 shot-peened disc (RR2)

C Hydrophobic surface finish

- i) *Cytop* surface treatment on aluminum disc
- ii) *Aculon* (1 hr & 8 hr dip coat) surface treatment on aluminum disc

D Superhydrophobic coatings (commercial and UVA nanocomposite surface)

- i) UVA SH-1 on aluminum disc
- ii) UVA SH-3 on aluminum disc
- iii) UVA SH-8 on aluminum disc
- iv) *NeverWet* on aluminum disc
- v) *Hydrobead* on aluminum disc

The surface wettability parameters (CA, CAH, RCA) of all the coatings (categories A-D) described in this section were measured at three separate locations on the substrate using a goniometer (Model 290, Ramé Hart, USA) to provide

averaged wettability values. In addition to as-received aluminum and titanium 6-4 control substrates, a titanium 6-4 shot-peened control surface was also tested (Figure 5.6).

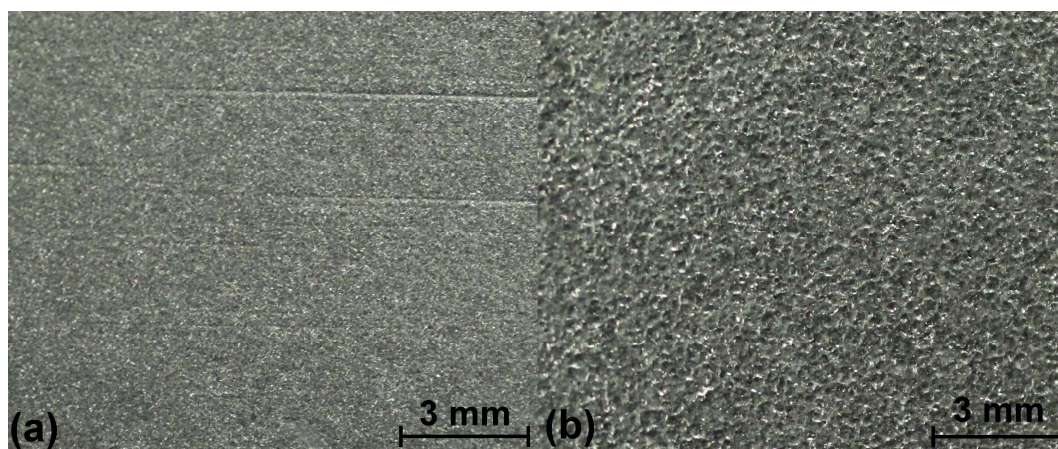


Figure 5.6 Optical microscope pictures of a titanium 6-4 surface. (a) as-received and (b) shot-peened.

This shot-peening process was performed by Metal Improvements Co, Derby, UK, and involved the impact of the titanium surface with glass beads to create a roughened surface finish. This is a procedure commonly conducted on blades and discs in turbine engines to improve their fatigue strength.¹²⁷ The effect of particle impingement on the surface is clearly observed. For the classification of hydrophobic coatings, commercial hydrophobic coatings (coating A1, A2 and B4) from Luna Innovations Inc. were applied on shot-peened titanium substrate discs. These coatings were translucent, which resulted in test substrates of similar visual appearance to an uncoated titanium shot-peened surface. In addition to hydrophobic

coatings, commercial hydrophobic surface finishes were also tested. These include formulations from *Cytop* and *Aculon*. *Cytop* is a transparent fluoropolymer product from Bellex International Corporation intended for optical and semiconductor applications. This coating was applied on as-received aluminum substrate discs via spin-coating. Similar to *Cytop*, *Aculon* is a transparent hydrophobic surface finish and was dip coated on aluminum substrates. Two different dip coating duration lengths were conducted; one for 1 hour and the other for 8 hours. The resulting surface finishes had different levels of surface wettability. The 1-hour dip coated surface had a CA of 105° and RCA of 71° , compared to a CA of 115° and RCA of 99° for the 8-hour dip coat. It should be noted that surface finishes from both *Cytop* and *Aculon* were fragile. Substantial loss of hydrophobicity occurred if physical contact was made with the surface finish, e.g., touching or rubbing the surface with fingers.

The superhydrophobic coatings that were tested in this experiment include commercial coatings as well as nanocomposite coatings fabricated via spray deposition techniques. The commercial coatings were *NeverWet* and *Hydrobead*, both of which were fabricated using two-step spray coating processes. In addition, three different superhydrophobic nanocomposite coating formulations were developed to produce surface finishes with arithmetic mean surface roughness (S_a) values of approximately $8\text{ }\mu\text{m}$ (SH-8), $3\text{ }\mu\text{m}$ (SH-3), and $1\text{ }\mu\text{m}$ (SH-1). The goal was to investigate the effects of surface roughness of these superhydrophobic coatings on ice

adhesion strength. These coatings were fabricated with the same spray-casting process described in Chapter 1, with aluminum substrates lying on a motorized platform traversing longitudinally and laterally, while the spray nozzle was held stationary. The formulations, surface preparation and spray deposition parameters for each of the surfaces are listed in Table 5.1.

	SH-1	SH-3	SH-8
PU wt%	25	24	24
PCBTF	33	29	0
Acetone	33	29	58
Water	0	12	12
PMC	5	3	3
Silica	3	3	3
Mixing	Sonication	Vortex	Vortex
Surface Cleaning	Yes	No	No
Spray Distance	6.0 in.	4.5 in.	3.5 in.
Air Pressure	50 psi	30 psi	30 psi

Table 5.1 Nanocomposite formulations, surface preparation and spray deposition parameters for the fabrication of SH-1, SH-3 and SH-8 coatings.

The formulation for the SH-8 coating consisted of a single-stage two component urethane paint (Imron AF3500, Dupont, USA) mixed in a vial with silica nanopowder (637246, Sigma-Aldrich, USA), acetone, and waterborne perfluoroalkyl methacrylic copolymer (PMC) (Capstone ST-110 ~80 wt.% H₂O, Dupont, USA). This emulsion was vortex-mixed for several minutes and then sprayed onto aluminum (320-grit sanded to promote mechanical adhesion between coating and substrate) using a conventional siphon atomizing spray nozzle (1/4JCO series, Spray

Systems Co., USA) with an air pressure of 205 kPa (30 psi) and spray distance of 9 cm (3.5 in). The coating was then immediately heat cured at 100°C for 6 hours. This coating is similar to the one used for the study of oblique impact dynamics described in Chapter 4.

The same urethane paint, silica nanopowder, and waterborne PMC were vortex-mixed for the SH-3 formulation. However, instead of acetone, a commercial urethane reducer consisting of parachlorobenzotrifluoride and acetone at a 90/10 vol% blend (13775S Medium VOC-Exempt Reducer, Dupont, USA) was used. This formulation was vortex-mixed and spray-casted with the same air pressure as SH-8 and was also immediately heat cured. However, the spray distance was increased to 11 cm (4.5 in) for SH-3. This resulted in a coating with a S_a of approximately 3 μm .

For the case of SH-1, urethane paint and silica nanopowder were dispersed in the previously mentioned urethane reducer. However, the waterborne PMC was treated differently. In a separate vial, equal volumes of trifluoroacetic acid (O4901-500, Fisher, USA) and waterborne PMC were mixed. This caused the fluoropolymer to come out of solution. While the as-received waterborne PMC solution had a slightly hazy orange color, the orange color of the polymer as well as white surfactants that stabilize the as-received latex became clearly visible when out of solution. The elastic nature of the acrylic polymer was also clear. The solid fluoropolymer was then re-dispersed in urethane reducer and vortex- mixed into the

urethane paint/silica/reducer emulsion. The entire mixture was sonicated at 35% amplitude and a frequency of 20 kHz for two minutes with an ultrasonicator (Model VC750, Sonics & Materials, Inc., USA). Viscosity was measured to be 15 seconds using a Zahn #2 cup (Gardco EZ Cup). The stability of SH-1 was discovered to be better than the other two formulations (SH-3 and SH-8). Since the surfactants in the as-received fluoropolymer were not compatible with acetone, agitation was required to keep SH-8 and SH-3 from separating into two phases. However, using treatment techniques for the waterborne PMC described above, SH-1 remained stable without the need for agitation.

In addition to sanding, the aluminum substrate for the SH-1 coating was washed with isopropyl alcohol to remove any contaminants such as wax or grease from the surface. The SH-1 formulation was then sprayed using the spray nozzle at an air pressure of 345 kPa (50 psi) and spray-casting distance of 15 cm (6 in). Unlike SH-8 and SH-3, the SH-1 coating was then allowed to flash off (all of the solvent left on the substrate after spray-coating evaporated after a period of 40 minutes) before being heat cured.

Figure 5.7 shows the SEM images acquired for the SH-1, 3 and 8 coatings. For SH-1, the lower surface tension of the PMC/reducer solution (25 dyne/cm) than the as-received waterborne PMC solution (72 dyne/cm) allowed for better substrate wetting and a more unified film with cracking in the film decreased. Washing the

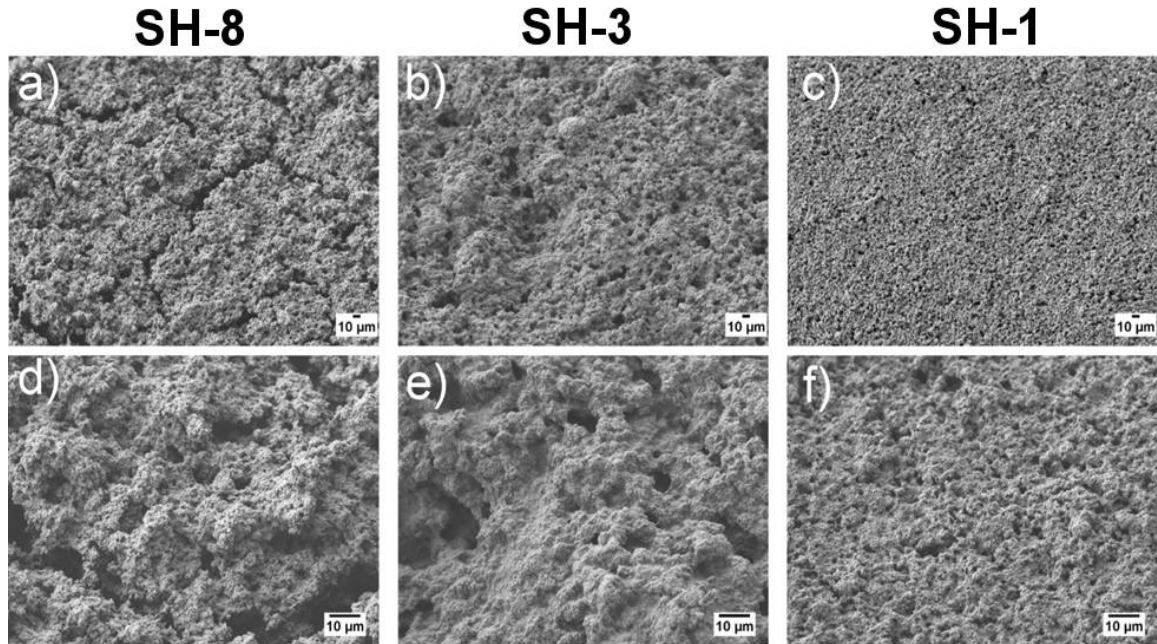


Figure 5.7 SEM images of (a) SH-8, (b) SH-3 and (c) SH-1. (d-f) are high magnification images of respective coatings. A reduction in surface cracking and increase in general homogeneity was observed from SH-8 to SH-1.

aluminum substrate with isopropyl alcohol before spraying also eliminated “craters” on the surface that are caused by contaminants that create uneven areas of surface tension. In addition, allowing the sprayed surface to flash off before heat curing allowed the surface to level as much as possible, and S_a was reduced to 1.7 μm . The morphology of SH-1, seen in Figure 5.7c, shows a much more uniform and homogeneous film, brought about by using a carrier fluid that allowed for leveling of the coating and wetting of the substrate before evaporation.

5.2.3 Test Procedures and Conditions

The design of this ice adhesion experiment provided the experimentalist the ability to remotely control and monitor the test (outside the walk-in cold chamber). This is advantageous because it allows the test to be performed at consistent temperatures, which in turn will result in ice accretion of consistent quality.

The test procedure was as follows: first, the PTFE “defect” disc was placed over the access hole of the substrate disc. The walk-in cold chamber was then turned on and set to reach a temperature of -23°C . The reason for setting the target temperature lower than the intended testing temperature (-20°C) was to compensate for the warming of air by a pre-test spray initiated once an air temperature of -21°C was reached. Water and air pressure of the pre-test spray were 450 kPa (65 psi) and 35 kPa (5 psi), respectively. This 3-minute procedure was conducted to allow the temperature of water in the system to reach steady-state conditions. This is of importance since varying water temperatures will affect the degree of droplet supercooling as it travels from the nozzle exit to the substrate surface, which in turn will affect the type of ice formation on the test coating.

To prevent this pre-test spray from impacting the substrate disc, the shield shown in Figure 5.3 was extended. The air pressure was further increased to an operating air pressure of 138 kPa (20 psi) at the end of this 3-minute procedure for

an additional minute, after which the shield was retracted for ice accretion to commence on the substrate disc. Once an ice thickness of 10 mm was formed, the shield was extended to stop the ice accretion process and the spray was turned off. Air was then supplied to the substrate disc and increasingly pressurized at a rate of 14 kPa/sec (2 psi/sec) until the point of ice fracture. Pictures in Figure 5.8 show the separate stages of ice accretion until a thickness of 10 mm, followed by its release by pressurized air.

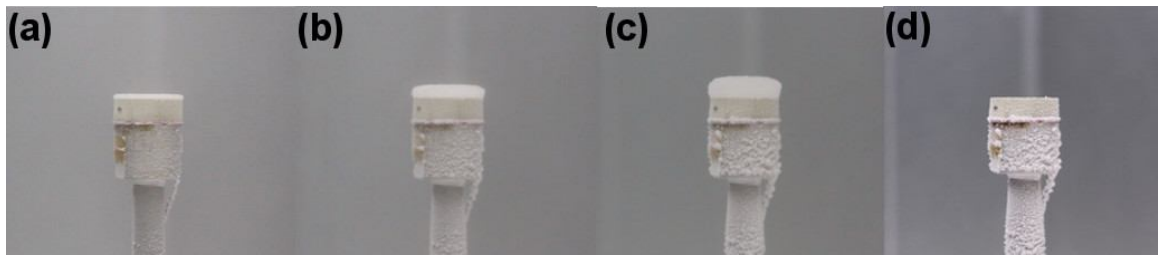


Figure 5.8 Stages of ice accretion on substrate disc followed by removal by pressurized air. (a) 2 mm thick ice after 20 seconds spray, (b) 6 mm thick ice after 80 seconds spray, (c) 10 mm thick ice after 135 seconds spray and (d) release of ice by pressurized air.

In the scenario of a mixed-mode ice fracture (where a portion of ice remained adhered to the test substrate), a picture of the test substrate was taken from the top-down perspective. Quantification of the area of adhered ice was then conducted and used for the calculation of fracture energy. Details of the fracture energy calculation are provided in the next section. Once this step was completed, the freezer was turned off and the water tube purged. This test procedure was repeated

three times for each coating so that an averaged ice fracture energy could be obtained. A time line summarizing the sequence of events of the experiment is shown in Figure 5.9.

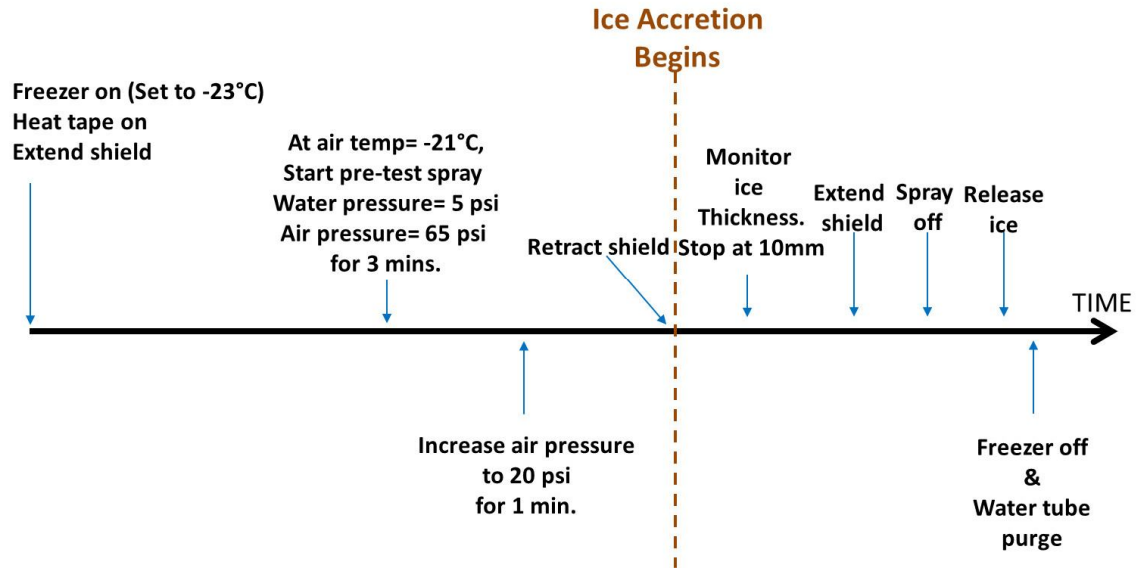


Figure 5.9 Sequence of the experiment procedures.

Figure 5.10 shows the typical temperature variations of the air, substrate disc, spray nozzle and water tube with respect to time, from the point where the walk-in cold chamber was turned on until the end of the experiment. The approximate locations at which these parameters were measured are shown in Figure 5.1. The temperature variations are divided into four segments based on previously described test procedures. In the first segment, the walk-in cold chamber was cooled from room temperature to its target temperature of -23°C .

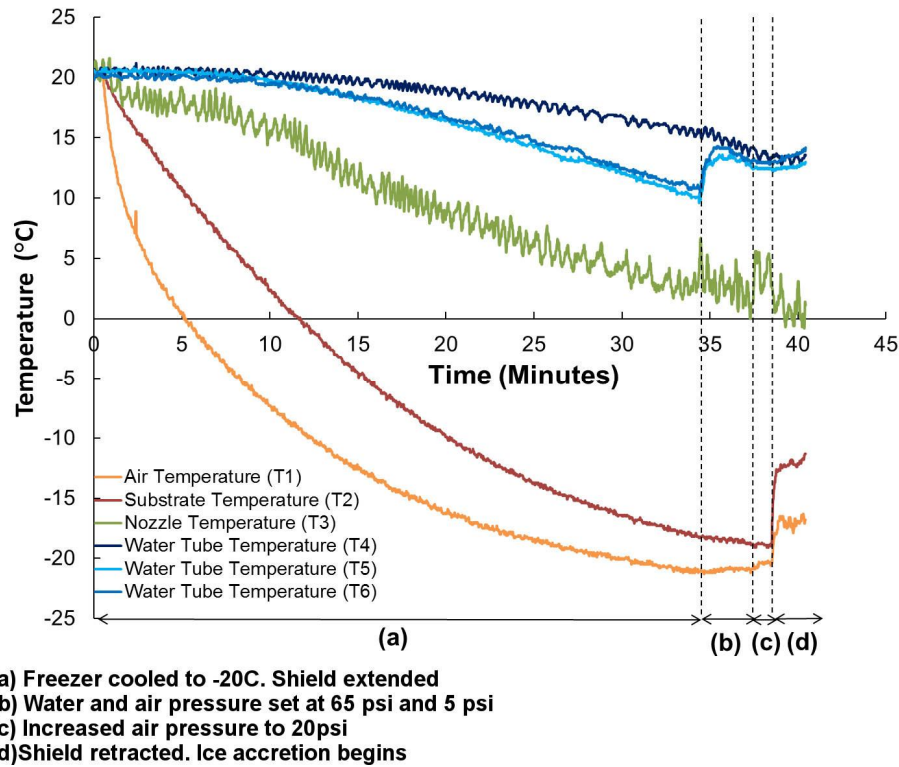


Figure 5.10 Temperature variation of air, substrate disc, spray nozzle and water tube with respect to time.

The temperature of water was assumed to be equivalent to the temperature of the water tube and was acquired at three separate locations (T4-T6 in Figure 5.1). In the second segment, the pre-test spray was initiated, causing the water temperatures to move toward steady-state conditions. Since the shield was extended, the substrate disc was not exposed to the pre-test spray and hence continued to cool. This trend continued in the third segment, where the air pressure was increased to reach operating conditions. In the fourth segment, the shield was retracted and the ice accretion process began. Water temperatures in this segment had reached steady-

state conditions. Due to the impact of super-cooled water droplets, the temperature of the substrate disc abruptly increased to approximately -13°C.

5.2.3 Calculation of Ice Fracture Energy

The process of ice removal from the substrate disc by air pressurization can either result in a cohesive or an adhesive fracture. Cohesive fracture refers to a failure through the ice structure, resulting in an adhesion of ice on the surface. On the other hand, an adhesive fracture denotes an ice-surface interfacial failure. In this study, fracture cases were either in a completely adhesive fracture mode or in a mixed-mode fracture (a combination of cohesive and adhesive failures). Generally, a mixed-mode fracture indicates a higher ice adhesion strength. Top-down pictures of the substrate disc depicting mixed-mode and full adhesive fracture are shown in Figure 5.11. The cohesive (2τ) and adhesive (ω) ice fracture energies were derived by Andrews and Stevenson¹²¹ to be Equation 5.1 and 5.2, respectively.

$$2\tau = \frac{P_c^2 c}{Ef_1 \left(\frac{h}{c} \right)} \quad (5.1)$$

$$\omega = \frac{P_c^2 c}{Ef_2 \left(\frac{h}{c} \right)} \quad (5.2)$$

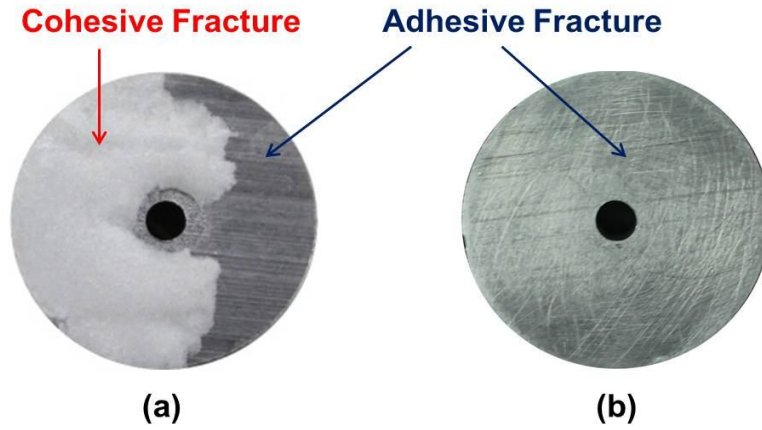


Figure 5.11 Top-down perspective of the substrate disc after ice fracture (a) mixed-mode fracture (cohesive + adhesive) on an as-received aluminum surface and (b) full adhesive fracture on an *Aculon* surface.

The constants f_1 and f_2 were defined as

$$f_1 = \frac{1}{1-\nu^2} \left\{ \frac{3}{32} \left[\left(\frac{c}{h} \right)^3 + \left(\frac{c}{h} \right) \frac{4}{1-\nu} \right] + \frac{1}{\pi} \right\}^{-1} \quad (5.3)$$

$$f_2 = \frac{1}{1-\nu^2} \left\{ \frac{3}{32} \left[\left(\frac{c}{h} \right)^3 + \left(\frac{c}{h} \right) \frac{4}{1-\nu} \right] + \frac{2}{\pi} \right\}^{-1} \quad (5.4)$$

where ν is the Poisson's ratio for ice (taken as 0.35),¹²² c is the radius of the “defect”, h is the height of ice accretion, E is the Young's modulus of ice (taken as 8.5 GNm^{-2} at temperatures above -20°C)¹²² and P_c is the critical air pressure required for ice fracture.

By quantifying the area of adhesive fracture of the substrate surface through image analysis of the top-down images (shown in Figure 5.11), the fracture energy can be determined as:

$$\text{Fracture Energy (J)} = \left(\frac{100 - \% \text{Area Ice Released}}{100} \times 2\tau \right) + \left(\frac{\% \text{Area Ice Released}}{100} \times \omega \right) \quad (5.5)$$

5.3 Results and Discussion

Figures 5.12 and 5.13 show the fracture pressure and energy of all the tested coatings arranged in decreasing order along the x-axis. A higher fracture pressure/energy indicates a stronger ice adhesion to the substrate and vice versa. It could be observed in Figure 5.12 that the control surfaces (aluminum and titanium 6-4 as-received) had the highest ice fracture pressures, while the majority of the hydrophobic surfaces recorded ice fracture pressures that were lower than the control surfaces. However, certain hydrophobic surfaces such as the RR2 and *Aculon* 1 hr coating showed higher ice adhesion strength as compared to the control surface of titanium 6-4 shot-peened. A larger variation in the ice adhesion strength for the superhydrophobic coatings was observed. While the UVA SH-3 and *Hydrobead* coating had relatively low ice fracture pressures, the UVA SH-8 coating depicted an ice adhesion strength that was as strong as the control surface of an aluminum as-

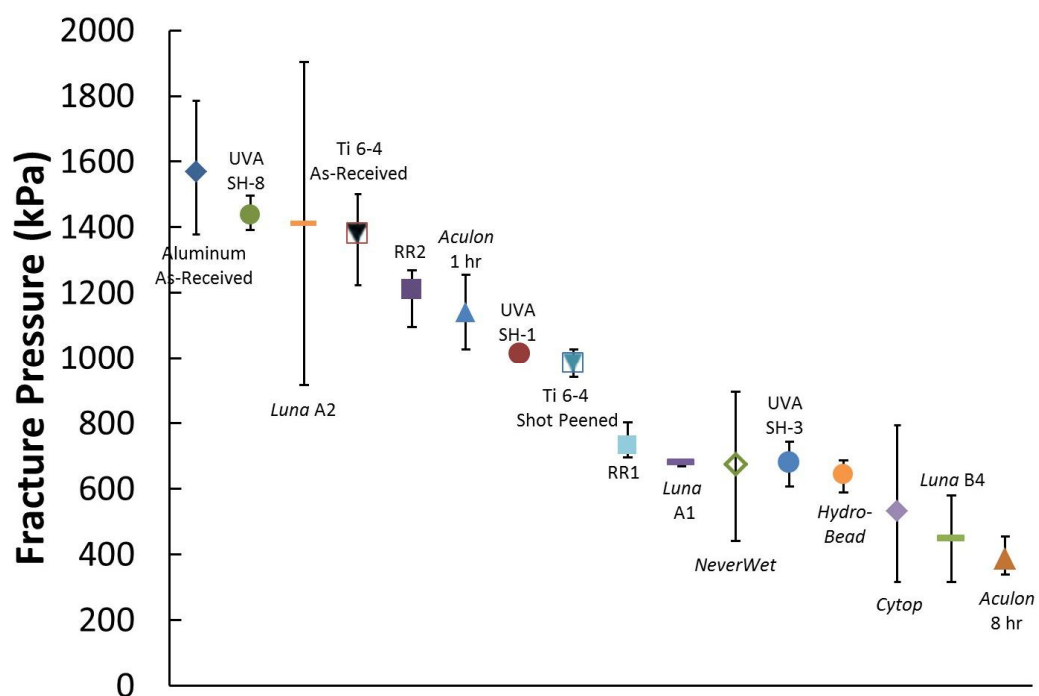


Figure 5.12 Ice fracture pressure of all tested coatings.

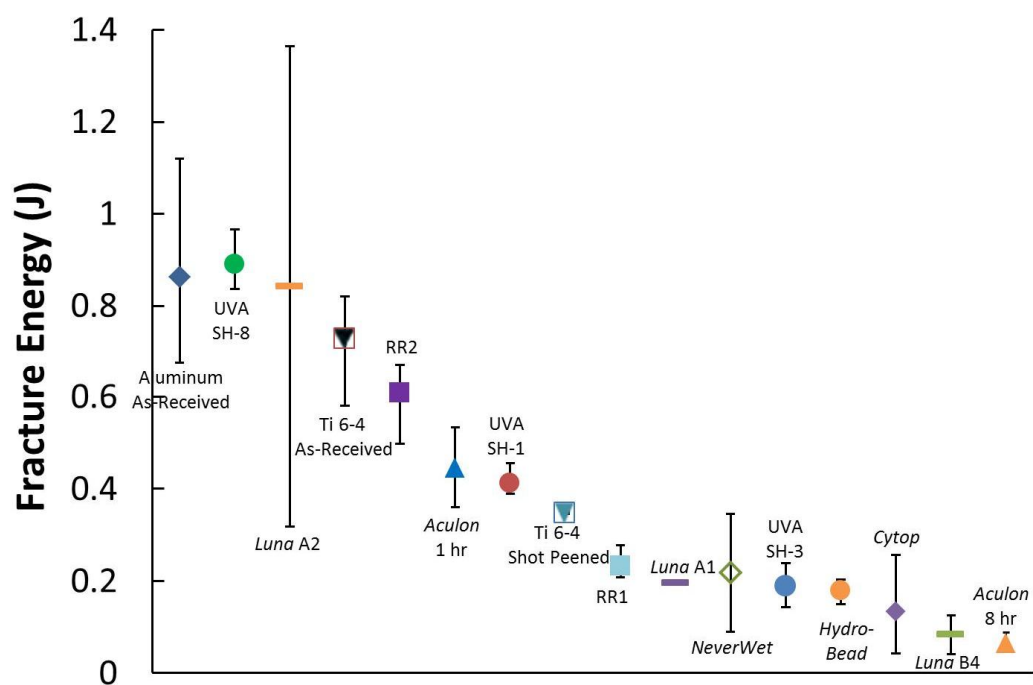


Figure 5.13 Ice fracture energy of all tested coatings.

received surface. This result could be attributed to the larger S_a of the SH-8 coating, which provided an increased surface area for the ice to latch itself on. However, the same explanation could not be applied on the UVA SH-1 coating. Even though it had the smallest S_a , its ice fracture pressure was higher than the UVA SH-3 coating. This result was unexpected and will be studied in further detail in Chapter 6.

For a coating to be considered an excellent ice-releasing surface, two conditions need to be met. In addition to low ice fracture energies, a high percentage area of adhesive fracture is desired. A coating with the above characteristics would be able to release a large amount of ice from its surface at a low fracture energy. Figure 5.14 was plotted to assess the ice release performances of each coating based on these two parameters. The figure can be categorized into excellent and poor ice-release regions located at the top left and bottom right hand corner of the figure, respectively. The boundaries of the excellent ice-release region were set at a fracture energy of less than 0.25 J and an percentage area of adhesive fracture of more than 80%. The position of the control substrates in the figure were also indicated for the ease of comparison with the rest of the coatings. Not surprisingly, since the ice adhesion strength of the control substrates was strong, they were located at an area which was close to the poor ice-release region indicated in Figure 5.14. Coatings that were identified to be excellent in ice-releasing performance consisted of a combination of hydrophobic (*Aculon* 8 hr & RR1) and superhydrophobic substrates

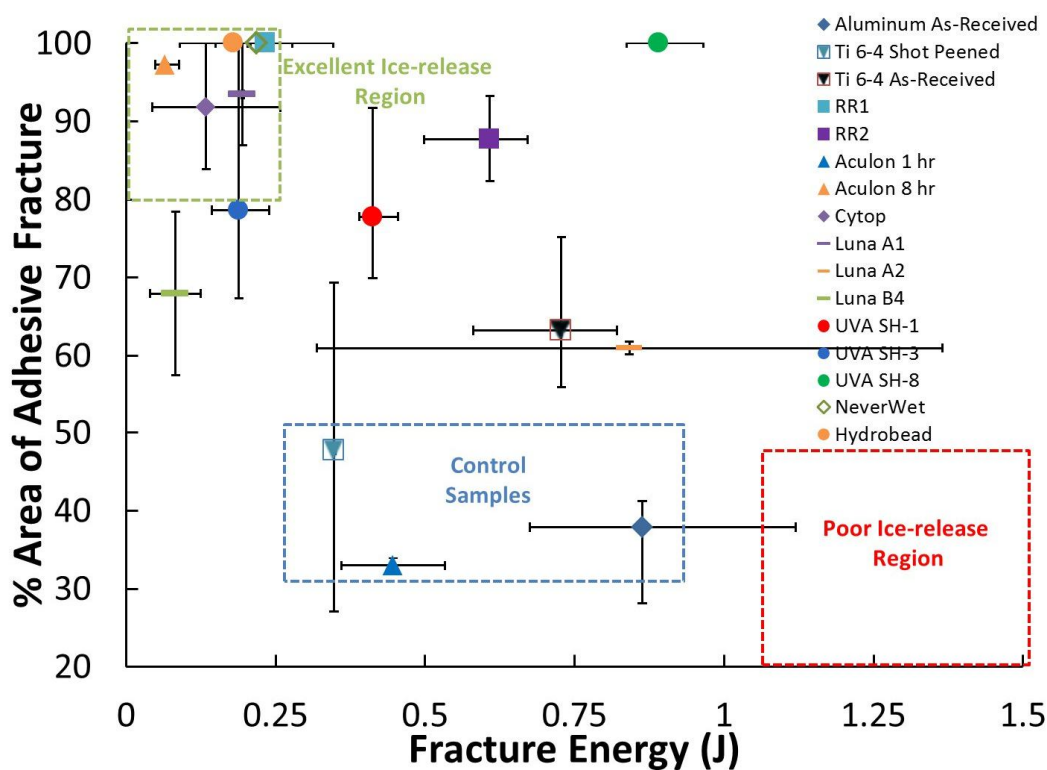


Figure 5.14 Percentage area of adhesive fracture of coatings plotted with respect to its fracture energy to identify coatings with desirable ice release performance.

(UVA SH-3, *NeverWet* & *Hydrobead*). The coating with the best ice-release performance was *Aculon* 8 hr with a fracture energy of less than 0.1 J for the release of close to 100% area of ice on the surface. This result was not surprising. The *Aculon* 8 hr had a surface finish resembling a layer of grease. As noted by Susoff *et al.*,¹¹⁷ these surfaces tend to have the lowest ice adhesion strength. However, it is fragile and has a limited lifetime and is therefore not suitable for implementation on realistic applications.

The correlation between the surface wettability parameters such as CA, CAH and RCA with ice fracture energy was investigated. This is shown in Figures 5.15 to

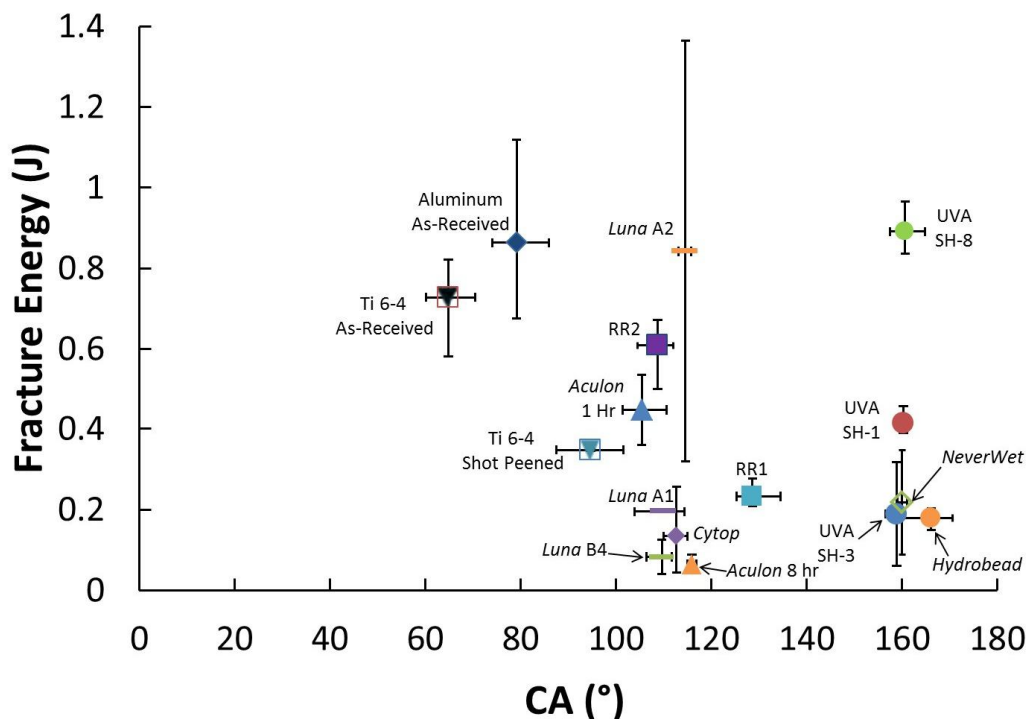


Figure 5.15 Effect of coating CA on ice fracture energy.

5.17 for all test coatings. It could be seen that significant scatter of data points was present in these figures. For example, in Figure 5.15, an increase in surface CA generally resulted in a lower ice fracture energy. However, a large variation in the fracture energy measurements was observed (from 0.1 to 0.8 J) for surfaces with CAs above 100°. Similar scatter of data points were observed for Figures 5.16 and 5.17 where dynamic angles (CAH and RCA) were plotted with respect to ice fracture energy. These scattered results highlight the need for a refinement of the experimental techniques and methods used in this investigation. This is necessary in order for a more consistent measurement of ice adhesion strength on the test substrates. This is the focus of Chapter 6.

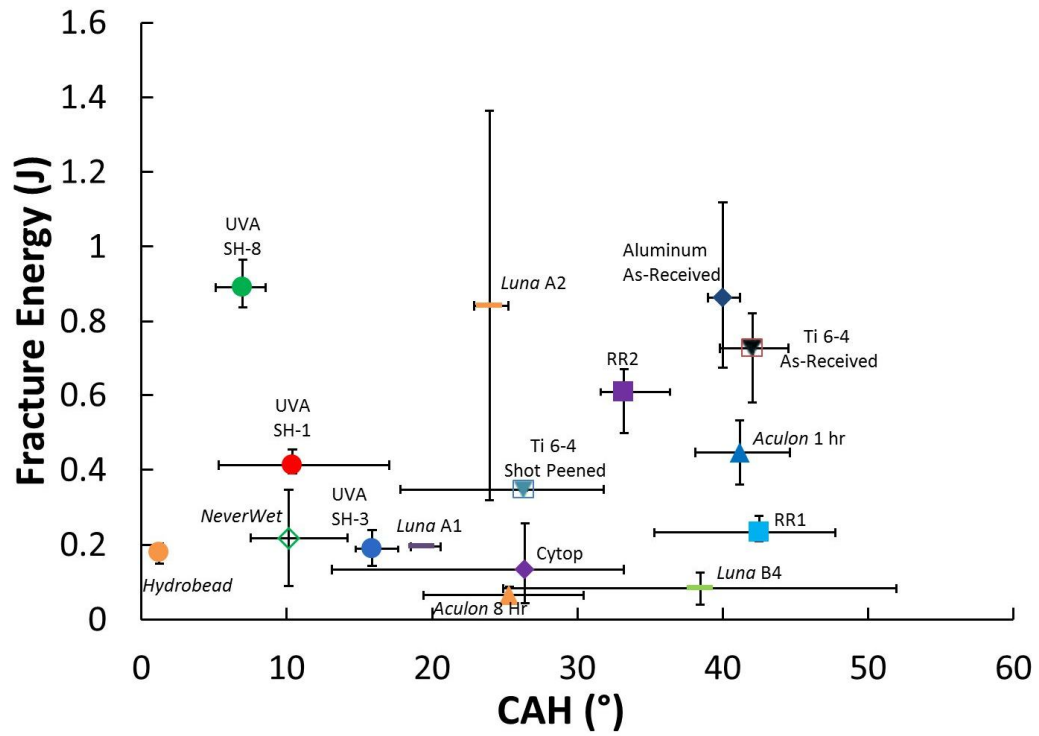


Figure 5.16 Effect of coating CAH on ice fracture energy.

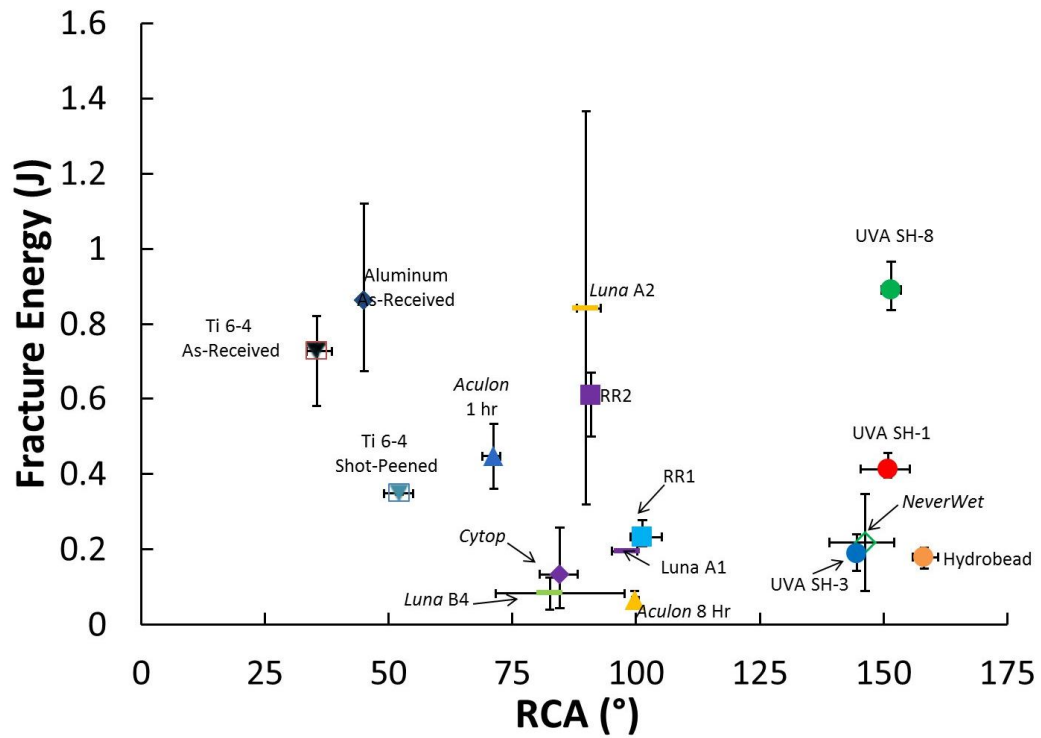


Figure 5.17 Effect of coating RCA on ice fracture energy.

5.4 Conclusions

The study of ice adhesion on hydrophobic and superhydrophobic surfaces was conducted by subjecting test substrates to a super-cooled spray consisting of 20 μm droplets in a walk-in cold chamber and at an air temperature of -20°C . The accreted ice was then removed by pressurized air in a tensile direction for a mode-1 fracture. The value of the critical ice fracture pressure was converted into an ice fracture energy, which was also a function of the percentage area of adhesive/cohesive failure on the surface. The coatings that were subjected to this test included aluminum and titanium 6-4 control surfaces as well as commercial hydrophobic coatings/surface finishes. In addition, nanocomposite superhydrophobic coatings at three different arithmetic mean roughnesses (S_a) were tested with two commercial superhydrophobic coatings. Results showed that in general, ice adhesion on hydrophobic and superhydrophobic coatings were lower than control surfaces. However, significant scattering of data points were observed when surface wettability parameters (CA, CAH, RCA) of the coatings were plotted with their ice fracture energies. This suggested that a refinement of the experimental methods used in this investigation was required. This is the focus in Chapter 6.

Chapter 6

Ice Adhesion Strength with a Thin “Defect”

6.1 Introduction

As described in Chapter 5, an experiment was conducted to measure the ice adhesion strength of hydrophobic and superhydrophobic coatings by exposing test substrates to a super-cooled icing spray consisting of 20 μm droplets in a walk-in cold chamber and at an air temperature of -20°C . Care was taken with the experimental methods (by precisely controlling the water and air temperatures) to ensure that the ice accretion was of consistent quality for all test substrates. However, the ice fracture energy results for these surfaces were found to be scattered. This is shown in Figures 5.15 to 5.17 where surface wettability parameters were determined to contain weak correlations with the ice fracture energies. In addition, the ice adhesion strength for a superhydrophobic nanocomposite surface with a 3 μm arithmetic mean surface roughness (S_a) was measured to be lower than a similar

coating but at an S_a of 1 μm . These results were unexpected. Therefore, a modification of the experimental methods was implemented and tests on down-selected and new coatings were conducted. The results were then analyzed with detailed surface topology measurements so that the factors and parameters controlling ice adhesion strength on hydrophobic and superhydrophobic surfaces could be better understood. This modified experiment and results are described in detail in this chapter.

6.2 Experimental Methods

6.2.1 Experimental Set-Up

A careful review of the current experimental methods compared with the techniques employed by Andrews & Lockington¹²² revealed that the scatter in ice fracture energy data points was due to an incorrect thickness of the “defect” disc. A 1 mm thick “defect” disc was used in the current experiment, as compared to a thickness of 250 μm employed by Andrews and Lockington.¹²² In addition, the 1 mm “defect” disc was not properly machined, resulting in a rough surface with edges that were slightly jagged. Since the role of the “defect” disc was to initiate and propagate the cracking of the accreted ice, the inconsistencies in its physical structure resulted

in variability of the air pressure that was required to release the ice from the surface of the substrate.

After a few iterations of trial and error, a PTFE “defect” disc with a thickness of 50 μm and a diameter of 7 mm was found to provide ice fracture energy measurements with the best repeatability. Multiple discs were fabricated by placing a 50 μm thick PTFE film (Goodfellow, USA) under a cork boring machine so that it could be pressed to the right dimension. The PTFE film was taped to a piece of paper which provided back support to the film and allowed the cutter to cleanly shear into the PTFE. This method of fabrication produced “defect” discs of consistent surface finish and quality.

The implementation of this new “defect” disc to the ice adhesion experiment, however, required a modification to the experimental set-up. This is due to the fact that the thin “defect” disc is delicate. If it were placed on the substrate disc and exposed to the super-cooled spray in accordance to the test procedures described in Section 5.2.3, it would most likely be removed from the substrate surface by the spray. In addition, these “defects” are not completely flat. There is a slight curve at the edge of the disc which leaves the access hole exposed to the icing spray. This could potentially cause ice accretion underneath the “defect” disc and in the areas within the access hole.

Therefore, the experimental set-up was modified from the one shown in Figure 5.1 to include a vacuum system to secure the thin “defect” disc on the substrate as well as to maintain proper coverage of the access hole. As shown schematically in Figure 6.1, this modification was performed on the air pressure delivery line. As compared to the previous set-up (Figure 6.1a), the modified set-up (Figure 6.1b) included a vacuum pump to provide a suction force to secure the thin “defect” disc in place. However, adjustment of this force was required to prevent the

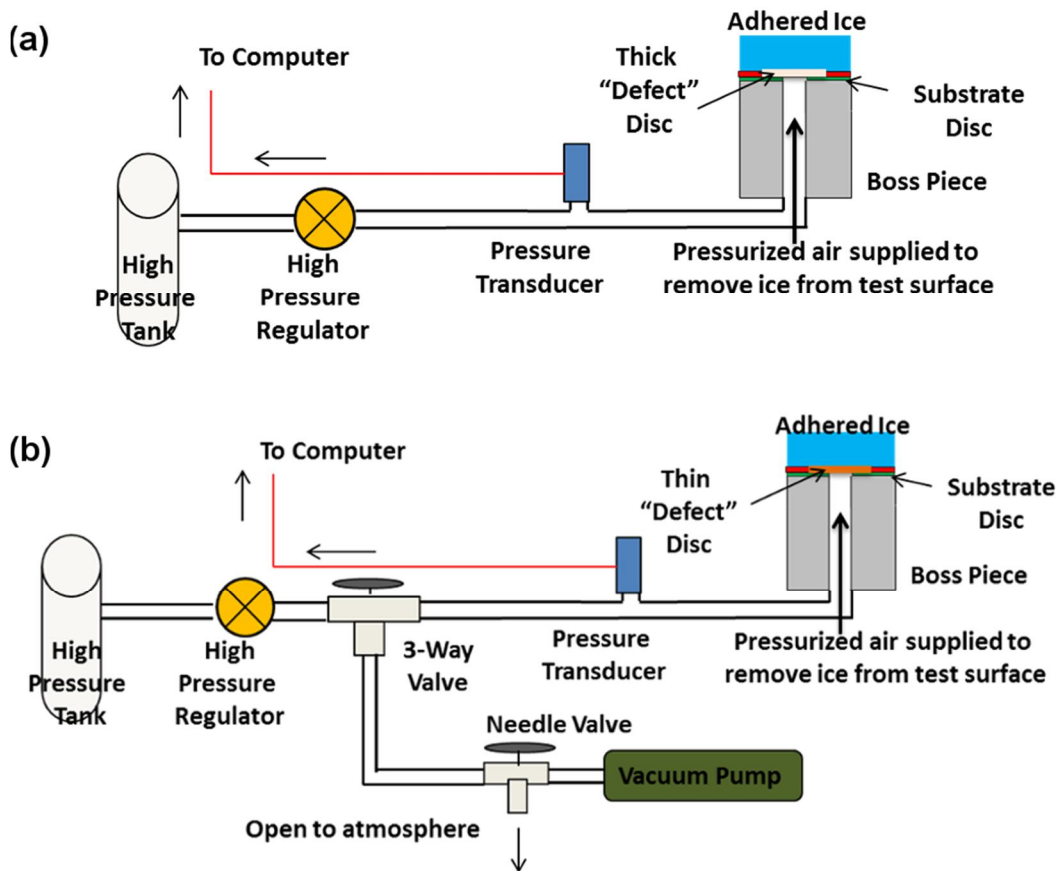


Figure 6.1 Schematic of the experimental set-up. (a) set-up for thick “defect” experiments and (b) modified set-up for thin “defect” disc experiments.

“defect” from being excessively pulled inward and into the access hole. Therefore, a needle valve with an open port to atmosphere was attached upstream of the vacuum pump. This allowed for the regulation of suction force disc so that it was secured “flat” over the access hole of the substrate disc. A picture of a properly attached thin “defect” disc on a substrate is shown in Figure 6.2. Since the same flow line was shared by the vacuum and ice fracture air pressurization system, a 3-way valve was installed. This allowed for the vacuum and ice fracture processes to be interchangeable.

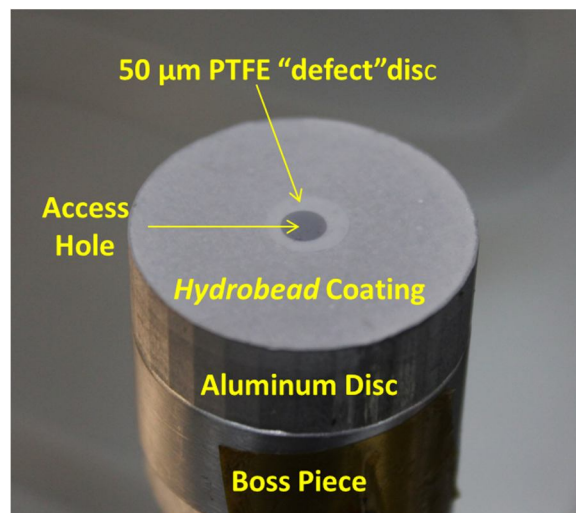


Figure 6.2 A 50 μm thick “defect” disc secured on a *Hydrobead* substrate disc by an adjusted suction force provided by a vacuum pump.

6.2.2 Modification of Test Procedures

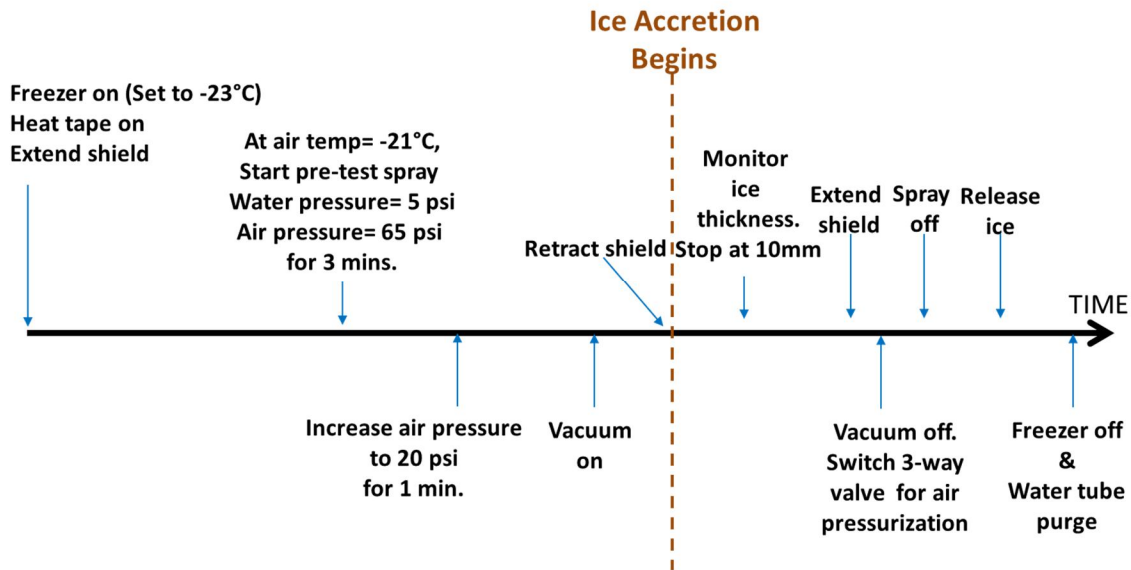


Figure 6.3 Sequence of the modified experiment procedures.

The implementation of a vacuum system in the experiment resulted in the need for a slight modification of test procedures that were previously described in Section 5.2.3. In general, the procedures were not substantially altered, e.g., a pre-test spray was still required for the water supply to reach steady-state temperatures as well as the retraction/extension of the shield to initiate/terminate the ice accretion process. However, additional steps were added to the procedures as shown in Figure 6.3. Namely, the vacuum pump was turned on 30 seconds before the shield was retracted. This was to ensure that the “defect” was held firmly in place. The vacuum system remained on until the ice accretion process was complete, after which it was turned off and the 3-way valve switched to allow for pressurized air to be

delivered to the substrate disc so that the ice could be fractured. As with the tests that were conducted with the thick “defects”, the experiment was conducted for three times for each coating.

6.2.3 Tested Coatings

Based on test results that were acquired using a thick “defect” in Chapter 5, coatings with good ice-release performance were down-selected and chosen to be re-tested with new iterations of thin “defect” ice adhesion experiments. As with coatings tested in Chapter 5, the substrates could be separated into four categories. These categories with their respective coatings are as listed:

A Control surfaces

- i) Titanium 6-4 as-received
- ii) Titanium 6-4 shot-peened
- iii) Aluminum as-received

B Hydrophobic coatings

- i) Rolls-Royce proprietary coating 1 on titanium 6-4 shot-peened disc (RR1)
- ii) Rolls-Royce proprietary coating 2 on titanium 6-4 shot-peened disc (RR2)
- iii) *Nusil* R-2180 coating on aluminum disc
- iv) Teflon PTFE coating (852G-201, Dupont) on aluminum disc

C Hydrophobic surface finish

- i) *Aculon* (8 hr. dip coat) surface treatment on aluminum disc

D Superhydrophobic coatings (commercial and UVA nanocomposite surfaces)

- i) UVA SH-a on aluminum disc
- ii) UVA SH-c on aluminum disc
- iii) UVA SH-d on aluminum disc
- iv) UVA ABS on aluminum disc
- v) *Hydrobead 1* on aluminum disc
- vi) *Hydrobead 2* on aluminum disc
- vii) Teflon PTFE SH (852G-201, Dupont) on aluminum disc

The wettability parameters (CA, CAH and RCA) for all 15 coatings in the test matrix were measured using a goniometer (Model 290, Ramé Hart). In addition, the surface features of the coatings were imaged using a confocal laser scanning microscope (Model 510 Meta, Zeiss) and re-constructed by a surface-imaging and metrology software (Mountains Map, Digital Surf) to provide a 3-D topology image representing an $800 \times 800 \mu\text{m}$ surface area. Quantitative surface roughness parameters such as arithmetic mean roughness (S_a), skewness (S_{sk}), kurtosis (S_{ku}) and autocorrelation length (S_{al}) were also derived from these topology images. This surface mapping technique was performed at three different locations on the substrate so that the variability of these roughness parameters across the surface could be determined.

Two new hydrophobic commercial coatings were introduced in the test matrix. These coatings were *Nusil* R-2180 and Dupont Teflon PTFE coating. *Nusil* R-2180 is a silicone-based, translucent coating targeted at aerospace applications and designed specifically for high ice-release performance. On the other hand, the Dupont Teflon PTFE coating is an industrial topcoat product. Primers were first coated on the substrates (SP-270, *Nusil* and 850G-314, Dupont) prior to the application of these hydrophobic products on the surfaces. While the *Nusil* R-2180 was spray-coated on an aluminum substrate disc, the Dupont coating was applied on the substrate disc with a paint brush.

A high number of superhydrophobic coatings were selected for testing. Although these coatings have similar CA, CAH and RCA, their surface topology parameters such as S_a , S_{sk} and S_{ku} were different. The goal was to study the effects of these roughness parameters on ice adhesion strength. Nanocomposite coatings (UVA SH-a, c and d) were manufactured according to the SH-1, 8 and 3 formulations and fabrication techniques previously described in Section 5.2.2, respectively. Another superhydrophobic coating was fabricated with the Dupont Teflon PTFE product. This was accomplished by spray-coating the product onto aluminum substrates to create a textured surface consisting of a low-surface-energy material, hence rendering the coating water-repellent. In addition, a new nanocomposite superhydrophobic coating (UVA ABS) was developed. This coating consisted of the

combination of acrylonitrile butadiene styrene (ABS) and hydrophobically modified fumed silica (HMFS) particles. A two-step spray deposition process was employed. The ABS was first sprayed on an aluminum substrate as a binder to create micro-scale roughness followed by the dispersion of HMFS on top of the ABS to introduce secondary roughness. Subsequent thermal curing above the glass transition temperature of ABS was performed. The curing promoted the bonding of the polymer and particles on the aluminum substrate to result in the formation of a nanocomposite superhydrophobic coating.

Two different versions of *Hydrobead* coating were tested. Although the fabrication process for these two coatings was identical, it was discovered that the roughness parameters from the resulting coatings were different. This was suspected to be due to sensitivity to spray-casting distance as well as environmental conditions such as temperature and humidity. These coatings of similar chemistry but varying surface features were named *Hydrobead 1* and *2*, respectively. SEM pictures of the ABS and *Hydrobead 2* coating are shown in Figure 6.4. The acquired images showed remarkable similarity between these two superhydrophobic surfaces. Surface asperities of similar shapes and sizes as well as the presence of minor crack lines were observed for both coatings at the 500 \times magnification (Figure 6.4a and b). The similarities between these two coatings were further preserved at a high magnification of 5000 \times (Figure 6.4c and d). Sub-micron features of similar profiles

were observed which confirmed the existence of hierarchal surface structures for both ABS and *Hydrobead* coatings.

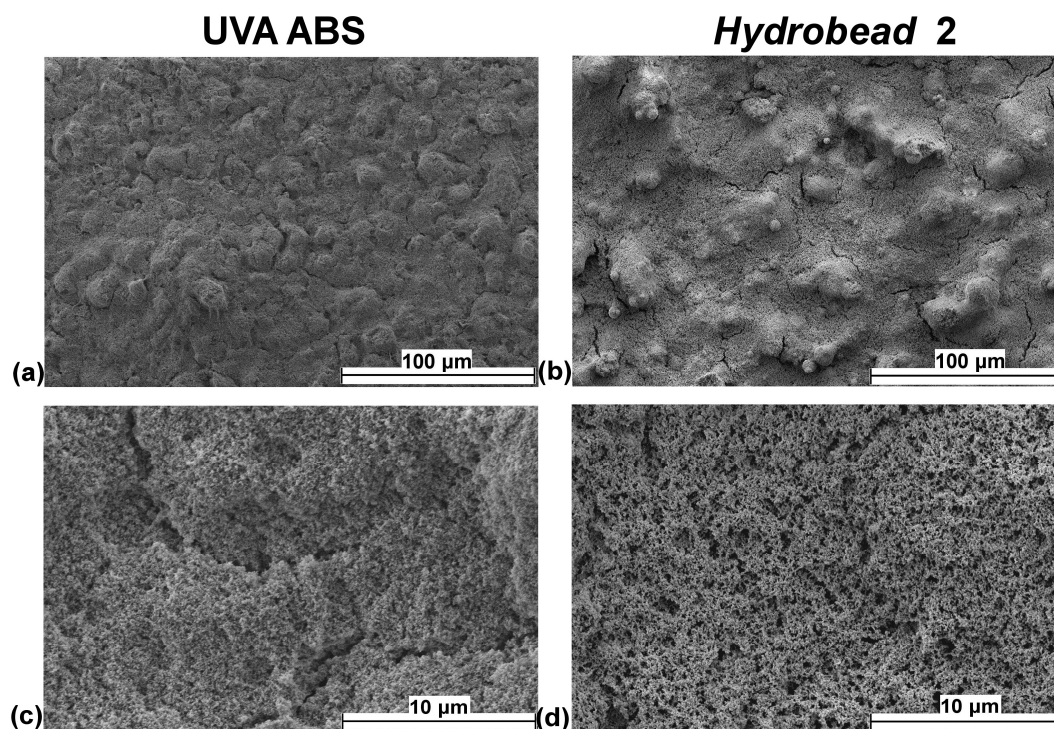


Figure 6.4 SEM images of (a) UVA ABS and (b) *Hydrobead 2* coating at 500 \times magnification. (c and d) are high magnification images of respective coatings at 5000 \times .

6.3 Results and Discussion

Ice fracture energies of all coatings were plotted with respect to surface wettability parameters of CA, CAH and RCA. This is shown in Figures 6.5 to 6.7, respectively. In addition, the averaged S_a of each coating was classified into six ranges and color-coded accordingly in these figures. Therefore, the effect of surface

wettability and S_a on ice fracture energy of the surface could be simultaneously studied. The S_a is defined in Equation 6.1 as:

$$S_a = \frac{1}{A} \iint_A |z(x, y)| dx dy \quad (6.1)$$

where A is the measured area and z the height of the surface features across the surface. This parameter provides a general description of height variations of the surface and hence is one of the most universally used roughness parameters.¹²⁸

It could be observed from Figure 6.5 that control and hydrophobic surfaces had a CA-ice fracture energy relationship that was different from superhydrophobic coatings. While ice fracture energy was found to generally decrease with increasing CA for control and hydrophobic surfaces, no correlation could be established between these two parameters for superhydrophobic surfaces. For example, CAs for all superhydrophobic surfaces were measured to be approximately 155°. However, the variability in their ice fracture energies was significant, ranging from less than 0.1 J to more 1 J. In addition, lower S_a (with the exception of the Teflon coating) was found to correlate with low ice adhesion strength for control and hydrophobic surfaces. This was to be expected since a higher S_a would result in a larger surface area for ice to attach to, which in turn led to an increase in ice adhesion strength. As with the CA, no correlation was found between S_a and ice fracture energy of superhydrophobic surfaces.

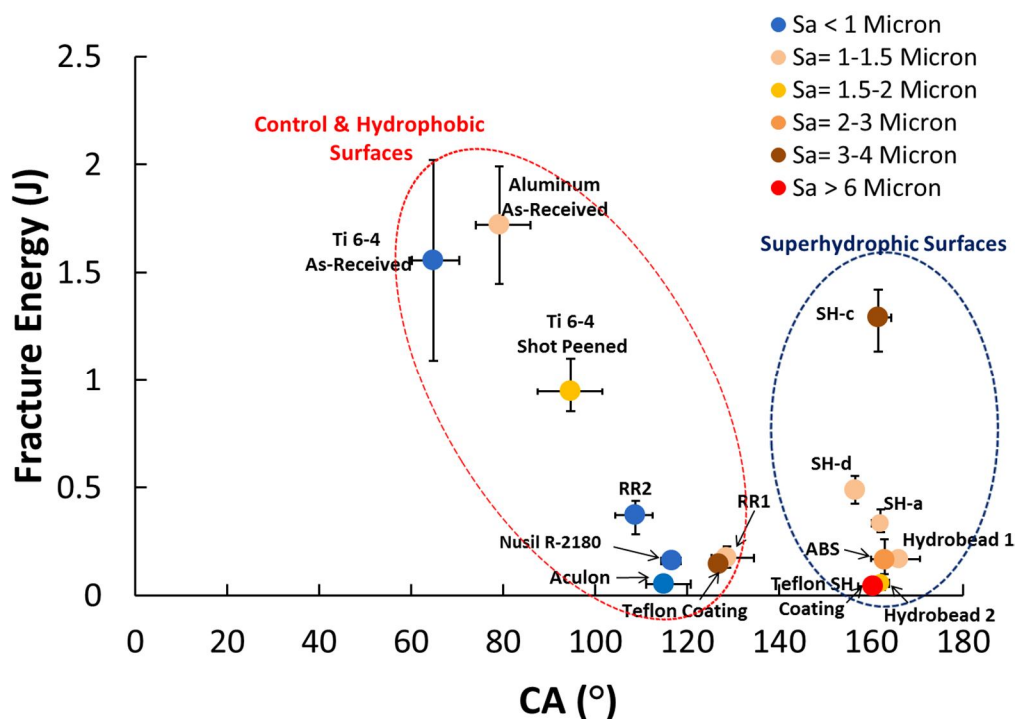


Figure 6.5 Effect of CA and averaged S_a (color-coded) on ice fracture energy of all tested coatings.

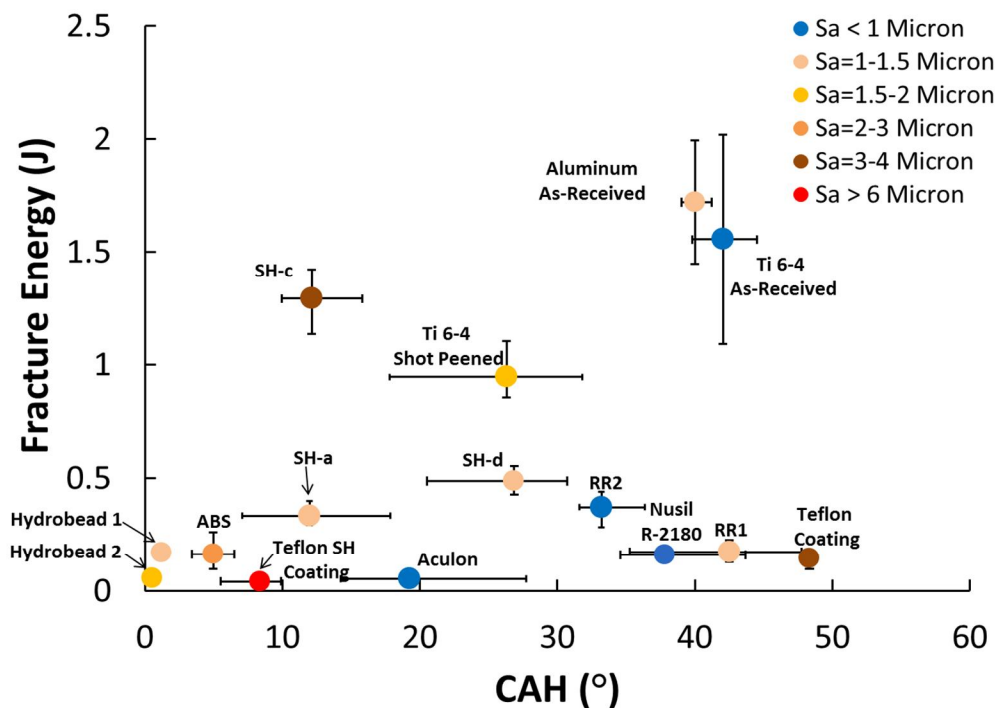


Figure 6.6 Effect of CAH and averaged S_a (color-coded) on ice fracture energy of all tested coatings.

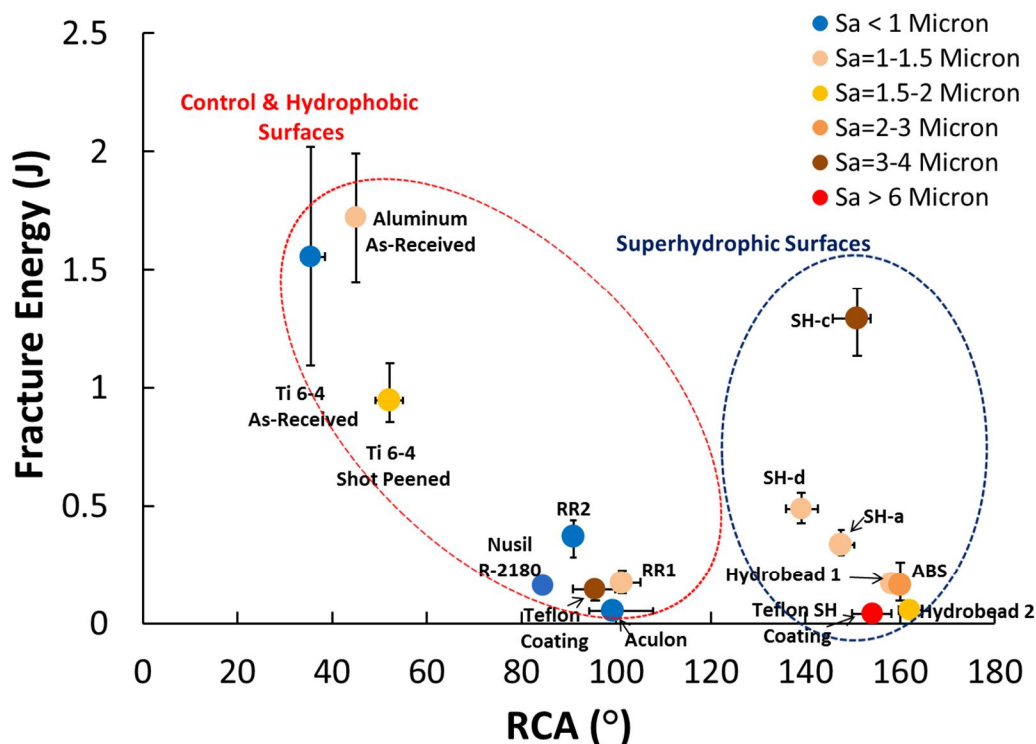


Figure 6.7 Effect of RCA and averaged S_a (color-coded) on ice fracture energy of all tested coatings.

A similar investigation was conducted to study the effects of dynamic wettability parameters (CAH and RCA) on ice adhesion strength. Different results were observed. As shown in Figure 6.6, no correlation between CAH and with ice fracture energy could be established (hydrophobic and superhydrophobic surfaces alike). However, ice adhesion was found to be a strong function of RCA for control and hydrophobic surfaces (Figure 6.7). These results were consistent with experimental observations of Meuler *et al.*,¹⁰⁵ who noted that ice adhesion strength for hydrophobic materials is not a strong function of CAH but rather RCA. This could be explained by the fact that the RCA is a parameter that quantifies the

affinity of a liquid to a surface under dynamic conditions. Therefore, a higher RCA indicates a high degree of water-repellency which translates to a low ice adhesion strength.

The RCA results for control and hydrophobic surfaces shown in Figure 6.7 could be further separated into two classifications: i.e., coatings applied on aluminum and on titanium 6-4 substrates. Since the substrates are of different materials, they also have different thermal conductivities. It is hypothesized that the ice adhesion strength could be a function of thermal conductivity, especially since there is a difference in temperature between the impacting super-cooled droplets and the freezing substrate. Hence, the RCA-fracture energy results for aluminum and titanium substrates were extracted from Figure 6.7 and plotted as two separate graphs as shown in Figures 6.8 and 6.9. It could be observed that the previous relationship of increasing RCA with decreasing fracture energy is preserved. In fact, results from these two figures strengthen the above correlation.

A similar extraction for superhydrophobic coatings from Figure 6.7 was performed and shown in Figure 6.10. It could be observed that ice adhesion also decreased with RCA. However, as compared to the results for hydrophobic surfaces (Figures 6.8 and 6.9), the correlation between RCA and fracture energy was not as strong. Since an important criterion for the creation of superhydrophobic surfaces is the introduction of surface texture on low-surface-energy materials to establish a

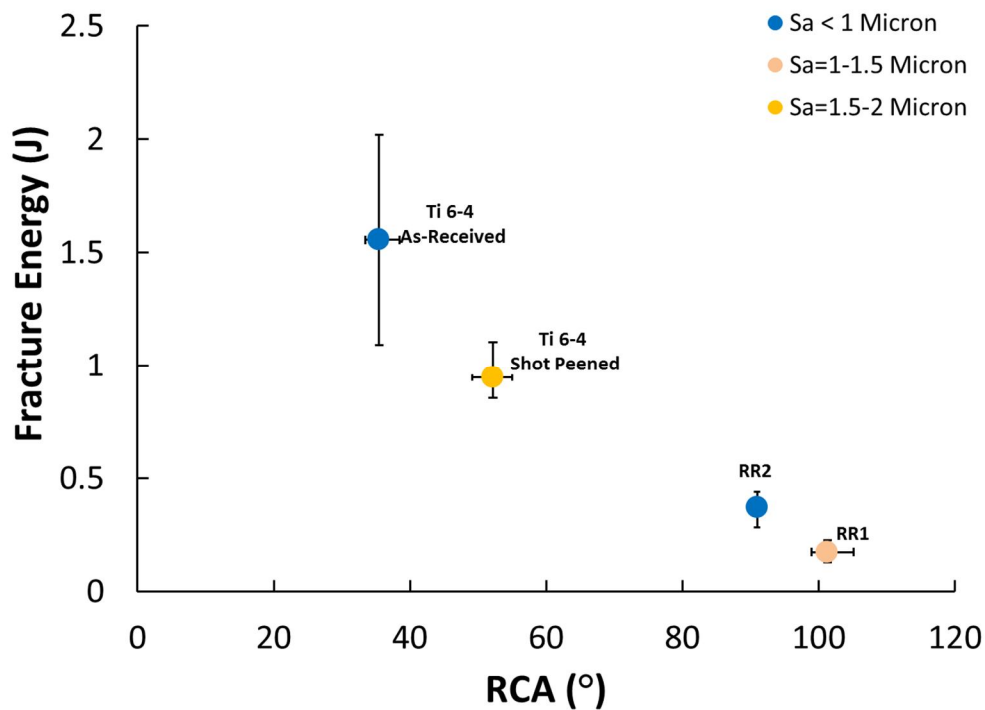


Figure 6.8 Effect of RCA and averaged S_a (color-coded) on ice fracture energy of hydrophobic coatings fabricated on titanium 6-4 substrates.

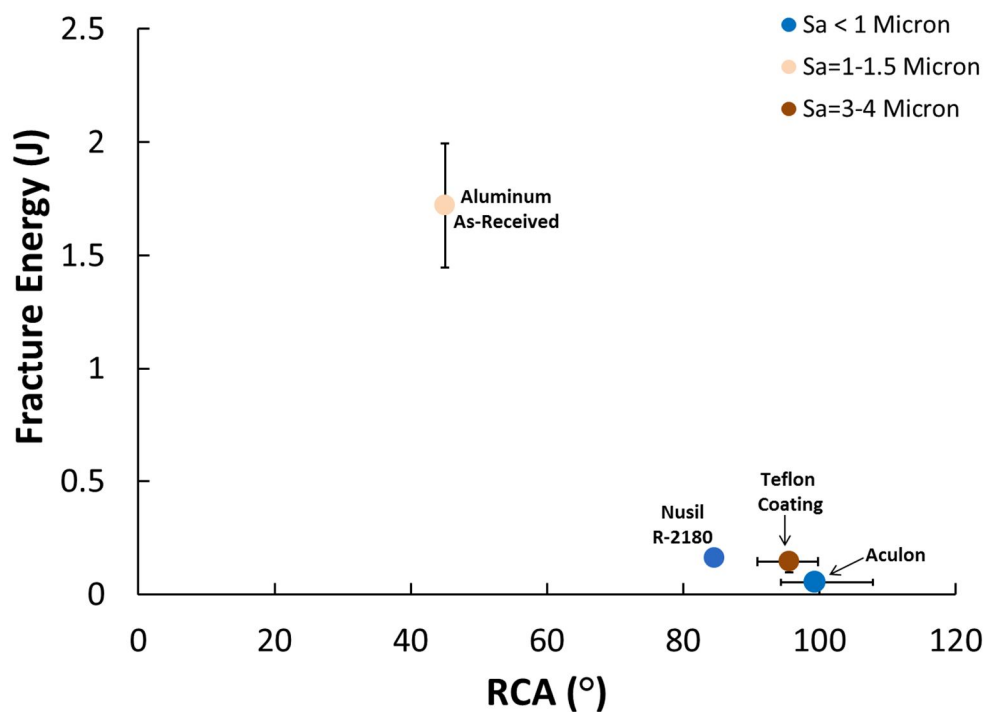


Figure 6.9 Effect of RCA and averaged S_a (color-coded) on ice fracture energy of hydrophobic coatings fabricated on aluminum substrates.

Cassie wetting state, one can assume that the surface roughness will have a significant impact on ice adhesion strength. Indeed, as shown in Figure 6.10, the superhydrophobic surface with the highest ice adhesions strength, SH-c, had a higher S_a (3-4 μm) compared to most of the coatings. However, a closer inspection of Figure

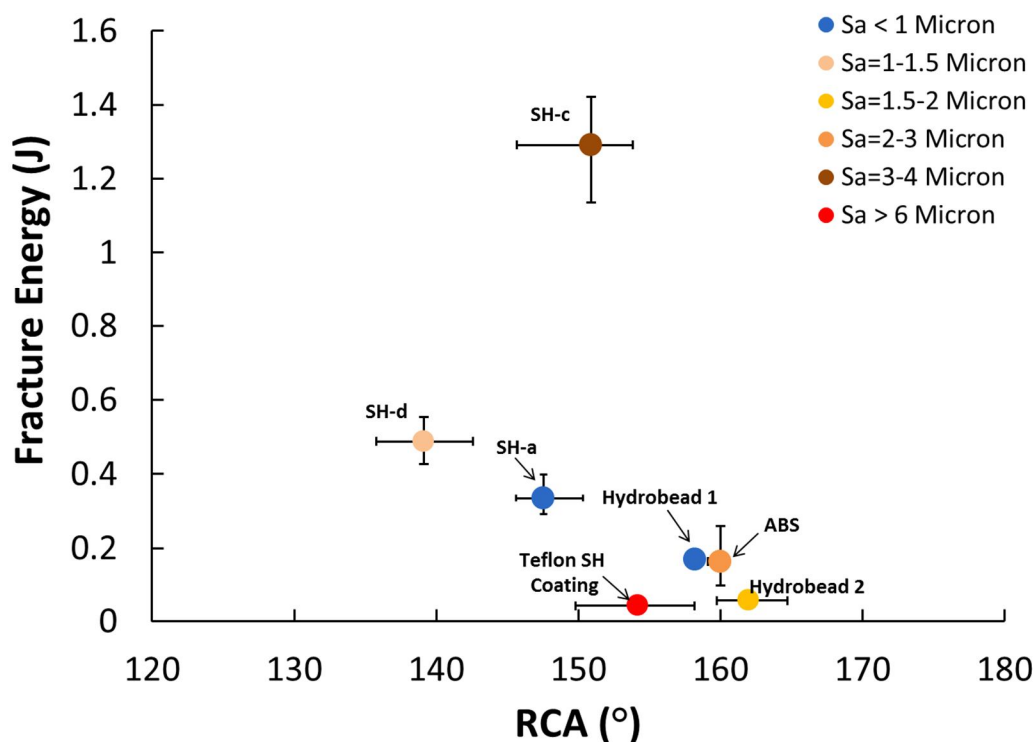


Figure 6.10 Effect of RCA and averaged S_a (color-coded) on ice fracture energy of superhydrophobic coatings fabricated on aluminum substrates.

6.10 revealed conflicting S_a trends. For example, the superhydrophobic surfaces with the lowest ice adhesion strength (Teflon SH and *Hydrobead 2*) had S_a values that were larger than SH-d, which had a stronger ice adhesion strength. This shows that the sole use of S_a is inadequate to quantify the effects of superhydrophobic surface roughness on ice adhesion. This was not unexpected. S_a merely describes the height

variations of a surface and does not provide information about the shape or wavelength of the measured features. It is also insensitive to small changes in profile.¹²⁸ Therefore, higher order surface roughness parameters were investigated.

The surface skewness (S_{sk}) is a parameter to measure the symmetry of the surface height distribution. It is mathematically defined as the third central moment of the profile height (z) distribution, measured over the assessment area.¹²⁸ This is shown in Equation 6.2.

$$S_{ssk} = \frac{1}{S_q^3} \left[\sqrt{\frac{1}{A} \iint_A z^3(x, y) dx dy} \right] \quad (6.2)$$

where S_q is the root mean squared (RMS) surface roughness (Equation 6.3).

$$S_q = \sqrt{\frac{1}{A} \iint_A z^2(x, y) dx dy} \quad (6.3)$$

This parameter indicates a positive S_{sk} for a surface with predominant high peaks. On the other hand, a surface with predominant deep valleys will have negative S_{sk} values. A surface with equal presence of peaks and valleys will have a normal distribution of heights with an S_{sk} of zero. Surface profile examples of positive and negative S_{sk} cases with its distribution curves are shown in Figure 6.11.

This figure was illustrated by Gadelmawla *et al.*¹²⁸

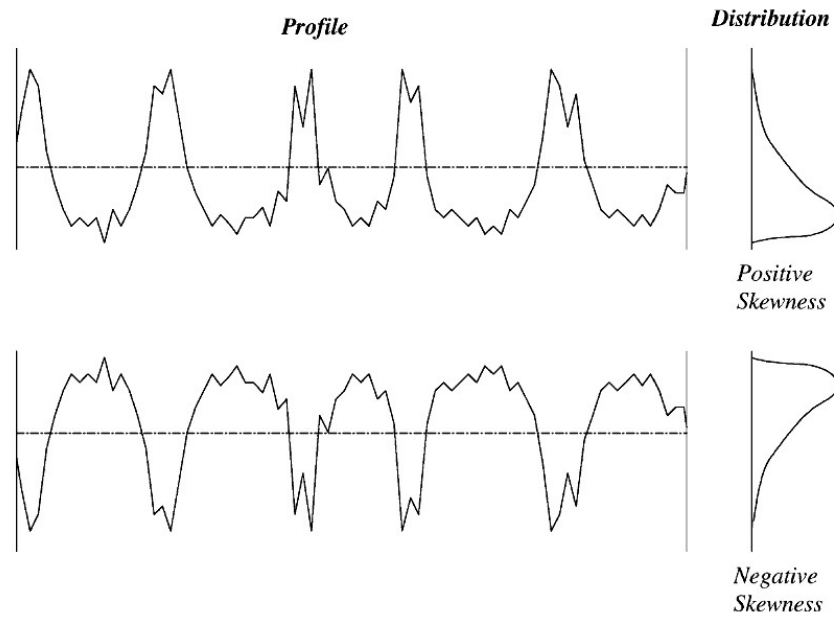


Figure 6.11 Profile examples of positive and negative S_{sk} with its height distribution curves.

The equation of 6.2 could be taken to an additional higher power to provide a surface kurtosis (S_{ku}). As shown in Equation 6.4, it is the fourth central moment of the profile height (z) distribution, measured over the assessment area.¹²⁸

$$S_{ku} = \frac{1}{S_q^4} \left[\sqrt{\frac{1}{A} \iint_A z^4(x, y) dx dy} \right] \quad (6.4)$$

A surface with inordinately high peaks and deep valleys will have a S_{ku} of > 3 while a gradually varying surface, free of extreme peaks or valleys will have a S_{ku} of < 3 . Surface profile examples of these S_{ku} cases with their distribution curves as prepared by Gadelmawla *et al.*¹²⁸ are shown in Figure 6.12.

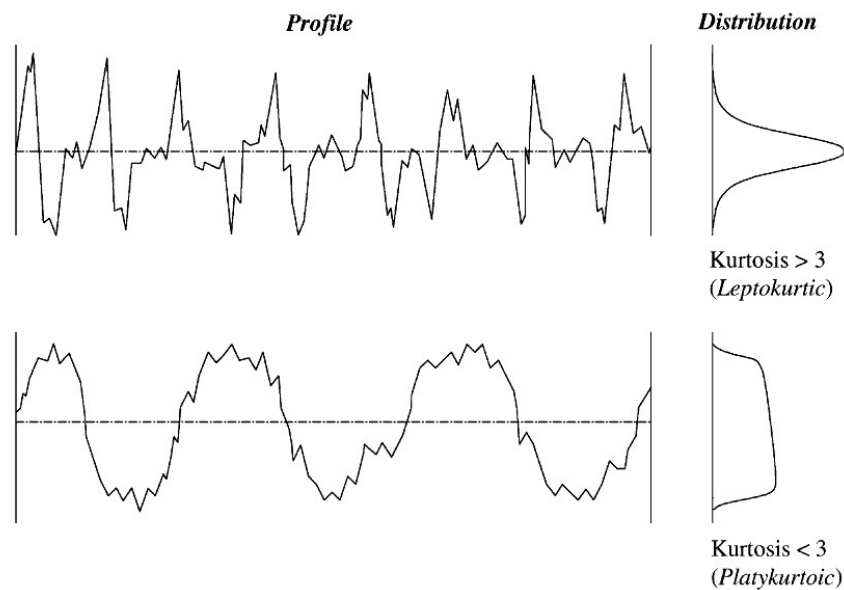


Figure 6.12 Profile examples of S_{ku} above and under 3, with its height distribution curves.

As shown in Figure 6.13, averaged S_{sk} of the superhydrophobic surfaces were color-coded accordingly with the RCA-fracture energy. The superhydrophobic coating with the strongest ice adhesion (SH-c) had a negative skewness (-1.4). This indicated the surface consisted predominantly of valleys. Therefore, it is hypothesized that the impact of super-cooled droplets on this surface would result in ice formation within these valleys which in turn increased the ice adhesion strength. This result was consistent with the observations of Kulinich and Farzaneh.¹¹³ However, no correlation between S_{sk} and ice fracture energy was observed for the rest of the superhydrophobic coatings.

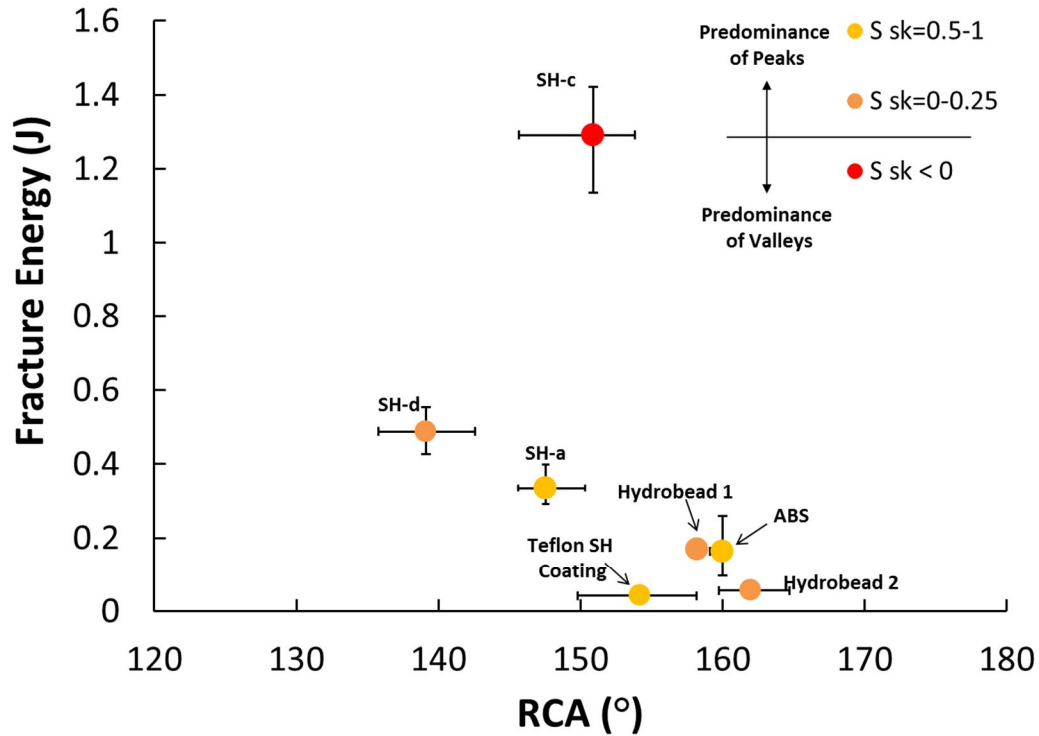


Figure 6.13 Effect of RCA and averaged S_{sk} (color-coded) on ice fracture energy of superhydrophobic coatings fabricated on aluminum substrates.

A similar investigation was conducted to study the effects of averaged S_{ku} of superhydrophobic surfaces on ice adhesion strength. (Figure 6.14) It was observed that the SH-c coating had a S_{ku} of over 5. This indicated that the valleys of the surface ($S_{sk} < 1$) were inordinately deep. Based on reasons described previously, this would result in a high ice adhesion strength. However, as with the S_{sk} study shown in Figure 6.13, there was no correlation between S_{ku} and the ice fracture energy for the remaining superhydrophobic coatings. The absence of correlation between S_{sk} and S_{ku} on ice adhesion strength was attributed to the fact that the variation of these values for the rest of the superhydrophobic coatings (with ice fracture energies < 0.6

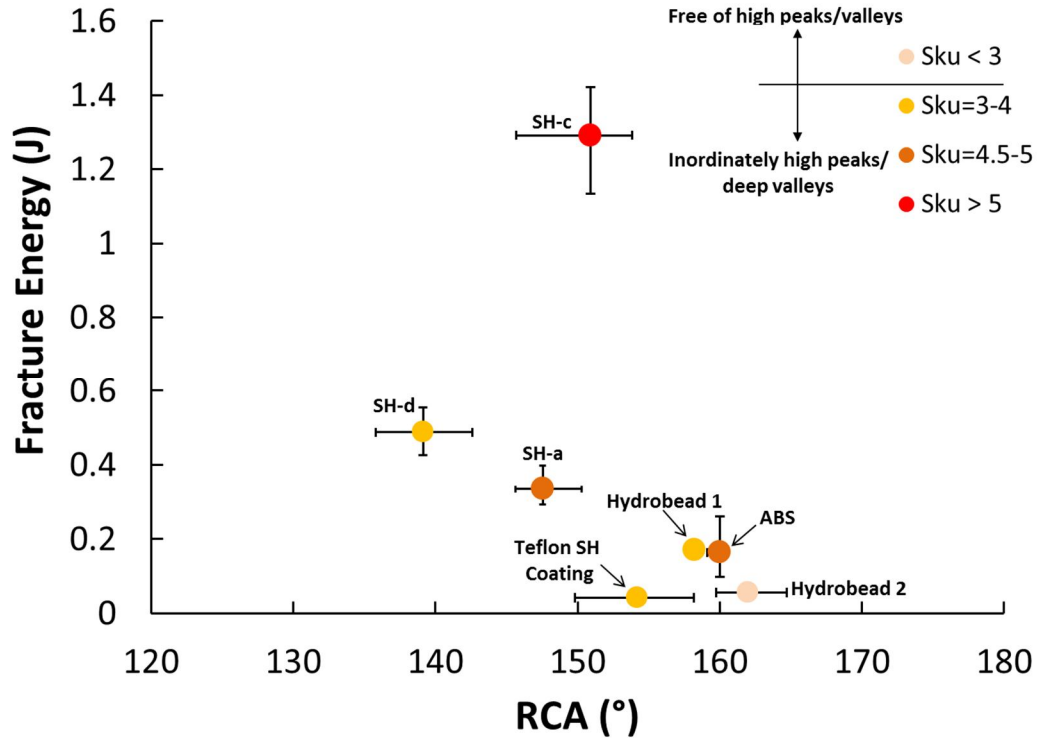


Figure 6.14 Effect of RCA and averaged S_{ku} (color-coded) on ice fracture energy of superhydrophobic coatings fabricated on aluminum substrates.

J) was small. As shown in Table 6.1, the S_{sk} and S_{ku} values for these superhydrophobic coatings ranged from 0.06 to 0.73 and 2.79 to 4.69, respectively. This is compared to the study conducted by Kulinich and Farzaneh,¹¹³ who fabricated two superhydrophobic coatings of significant disparity in S_{sk} (-1.27 to 5.02) and S_{ku} (7.36 to 25.13). Results from their experiment showed a lower ice adhesion strength for the surface with higher S_{sk} and S_{ku} . Therefore, it was hypothesized that the range of the S_{sk} and S_{ku} values of current coatings was not sufficiently large to affect the ice adhesion strength. Nevertheless, this suggested the

presence of additional roughness parameters that could affect the ice adhesion strength of the superhydrophobic surfaces.

	Teflon SH	Hydro. 1	Hydro. 2	ABS	SH-d	SH-a	Kulinich Spray Coat	Kulinich Spin Coat
S_a	8.35 μm	1.23 μm	1.87 μm	2.43 μm	1.17 μm	1.16 μm	419 nm	257 nm
S_{sk}	0.68	0.13	0.17	0.91	0.06	0.73	-1.27	5.02
S_{ku}	3.36	3.35	2.79	4.69	3.60	4.58	7.36	25.13

Table 6.1 S_a , S_{sk} and S_{ku} values for superhydrophobic surfaces with ice fracture energies of less than 0.6 J, as compared to superhydrophobic surfaces from Kulinich and Farzaneh.

While S_a , S_{sk} and S_{ku} describe the amplitude (height) characteristics of the surface features, the autocorrelation length (S_{al}) is a roughness parameter that describes the spatial relationship between surface features. This is defined in Equation 6.5 as

$$S_{al} = \underset{t_x, t_y \in R}{\text{MIN}} \sqrt{t_x^2 + t_y^2} \text{ where } R = \left\{ (t_x, t_y) : ACF(t_x, t_y) \leq 0.2 \right\} \quad (6.5)$$

where t_x and t_y are the autocorrelation functions in the x and y directions. The autocorrelation function (ACF) is a measure of how similar the textures are at given distances from the original location. It is obtained by mathematically multiplying two surfaces separated by a relative lateral displacement together to yield functions which quantify the degree of overlap. If the ACF is near unity for a given amount of

lateral shift, the texture is similar along that direction. On the other hand, if ACF is close to zero, the surfaces are then different and bear no similarity to the original measurement location.¹²⁹ The autocorrelation length (S_{al}) specified in Equation 6.5 is the spatial distance which has the fastest decay in ACF to a value of 0.2. Hence, this parameter provides a quantification of feature wavelengths on a surface. A high S_{al} indicates that the textures on a surface are separated further apart (high wavelengths) as compared to a low S_{al} which signifies features that are located closer together.

For example, S_{al} was measured on two test substrates consisting of pillar features of similar size and heights but at different inter-pillar distance spacing (28 μm and 90 μm). These surfaces were imaged with a laser confocal microscope to yield 3D topology images (as shown in Figure 6.15) as well as S_a and S_{al} measurements. It could be observed that although these two surfaces had similar roughness levels (2.8 μm vs. 3.1 μm), their S_{al} values were significantly different. This was to be expected since the pillars of these two surfaces were of the same heights. However, since the pillars were spaced at different distances, a higher S_{al} value was measured for the surface with larger inter-pillar distance and vice-versa. This shows the effectiveness of the S_{al} parameter in characterizing the spatial relationship of surface textures.

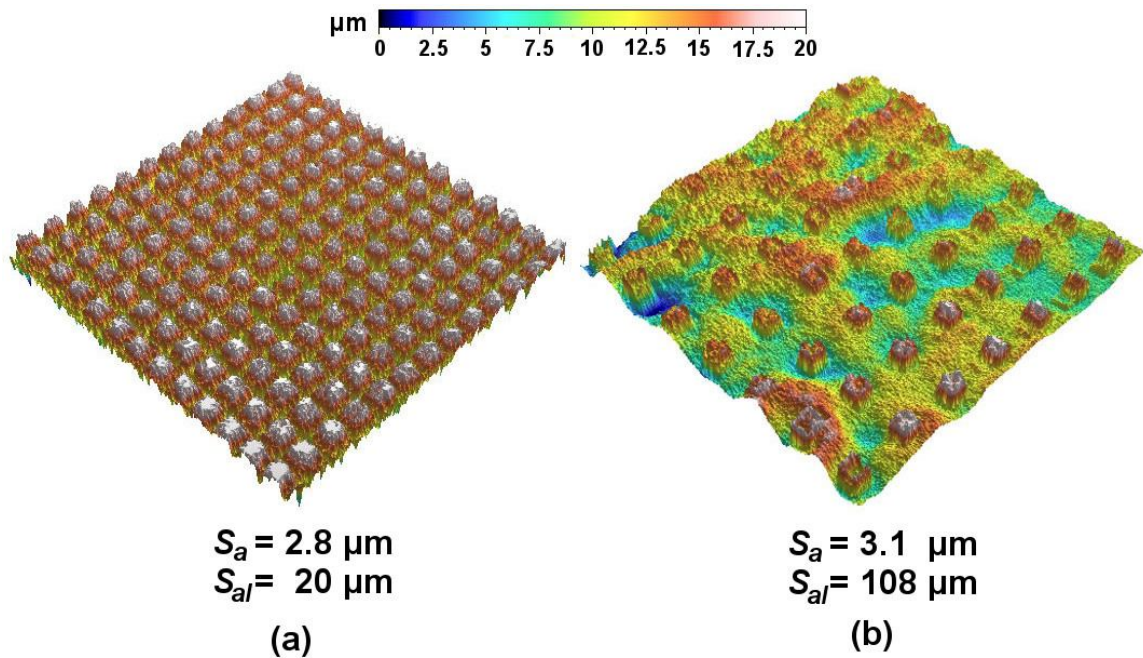


Figure 6.15 3D topology image of pillar surfaces with S_a and S_{al} measurements. (a) inter-pillar distance of 28 μm and (b) inter-pillar distance of 90 μm .

Figure 6.16 shows the effect of S_{al} and S_{sk} on the ice fracture energy of the superhydrophobic coatings. A good correlation between S_{al} and the ice fracture energy was established, i.e., increasing S_{al} of the surface generally leads to an increase in ice adhesion strength. This is due to the effect of super-cooled water droplet impact on the superhydrophobic surfaces. These droplets travel at a certain speed and, upon impact with the superhydrophobic surface, exert a Bernoulli pressure on the surface texture. If this pressure is greater than the capillary pressure of the surface textures, the water droplets will penetrate into the surface asperities, triggering a transition from a Cassie wetting state to a Wenzel wetting state before freezing.¹³⁰ This would cause an increase in the ice adhesion strength since the ice

has a larger surface area to adhere to. Therefore, the control of capillary pressure of the surface texture is crucial towards maintaining a strong resistance against droplet penetration. This capillary pressure is a strong function of spatial distances between surface features.¹³⁰⁻¹³² In a study conducted by Extrand,¹³¹ reducing the spatial distance of posts by two orders of magnitude was found to result in an increase of capillary pressure by the same amount. It is due to this reason that superhydrophobic surfaces with high S_{al} (Figure 6.16) were found to record stronger ice adhesion strength as compared to coatings with a lower S_{al} .

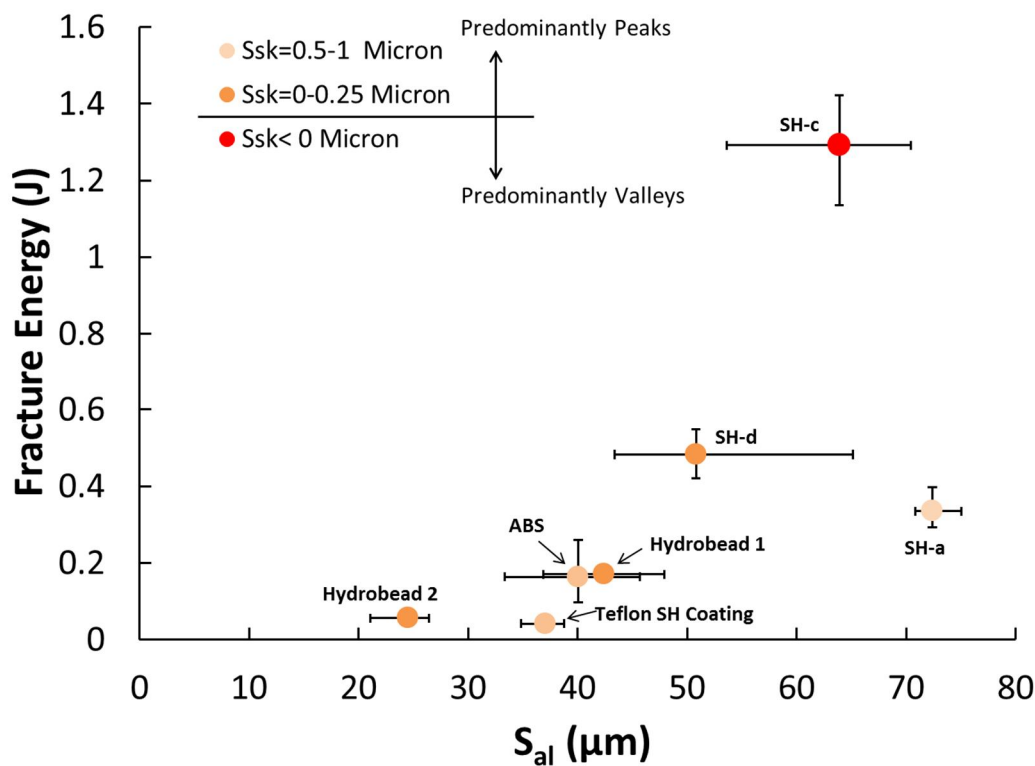


Figure 6.16 Effect of S_{al} and S_{sk} on ice fracture energy of superhydrophobic coatings fabricated on aluminum substrates.

As shown in Figure 6.17 where 3D topology images of superhydrophobic coatings of increasing ice adhesion strength (*Hydrobead* 2, SH-d and SH-a) were compared, one could observe the differences in the order and spatial distances of surface features between these respective coatings. While the *Hydrobead* 2 coating had features that were prevalent and spaced at close distances from each other, the surface features of SH-d and SH-a coatings were sparser and spaced increasingly further apart. The increasing spatial distances between the surface features of the respective coatings were indicated by the increasing S_{al} values that were measured and labeled accordingly.

This S_{al} effect was further investigated on superhydrophobic surfaces (SH-1, 3 and 8) that were previously tested with thick “defects” (as described in Chapter 5). As with Figure 6.16, the ice fracture energies of these surfaces were plotted with respect to S_{al} and shown in Figure 6.18. It could be observed that the correlation of S_{al} with ice fracture energy was maintained. The SH-3 coating which had the lowest S_{al} was found to have the lowest fracture energy, followed by SH-1 and SH-8. This confirmed the effect of S_{al} on ice adhesion strength of superhydrophobic surfaces.

The results from Figures 6.16 and 6.18 suggest that the effects of S_a and S_{ku} on ice adhesion strength, when compared to S_{al} , are secondary. This is due to the fact that when icing occurs on a superhydrophobic surface in a Cassie-Baxter wetting state (at low S_{al}), the formation of ice will be isolated on the tips of the features

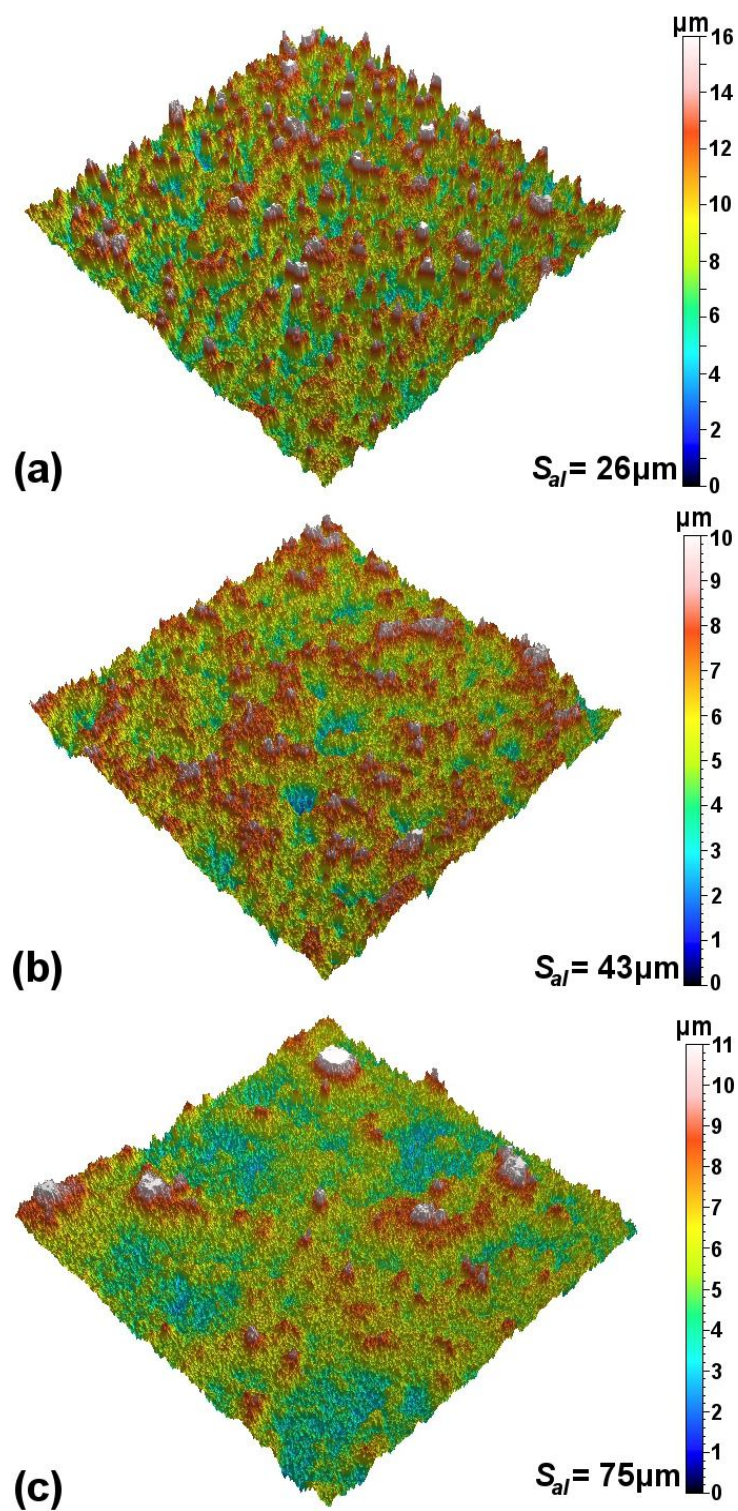


Figure 6.17 3D topography images of superhydrophobic coatings with S_{al} measurements (a) *Hydrobead 2* (b) SH-d and (c) SH-a.

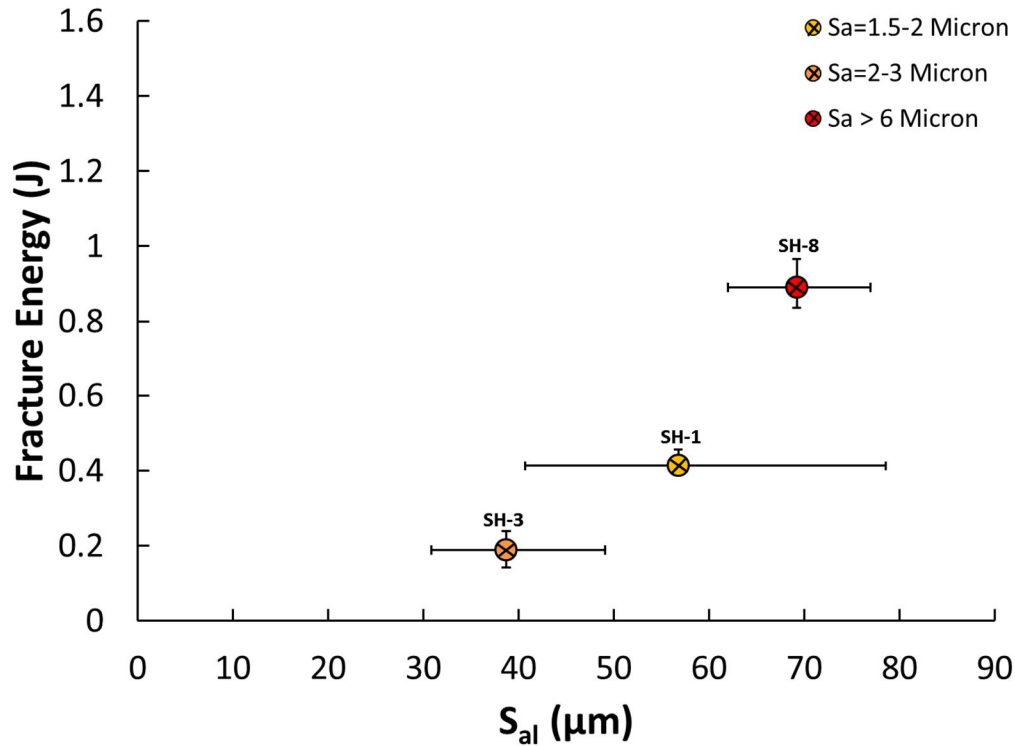


Figure 6.18 Effect of S_{al} and S_a on ice fracture energy of superhydrophobic coatings SH-1, 3 and 5 fabricated for tests described in Chapter 5.

without infiltrating into the asperities of the surface, which in turn drastically reduces the ice adhesion strength. In this case, the shape and variation of the feature heights do not influence the ice adhesion strength as ice does not make physical contact with the surface area of the inner asperities. This is shown for the coatings of *Hydrobead* 2 and Teflon SH in Figure 6.16. Even though there was a significant difference in S_a between these two coatings, their ice fracture energies were equally low. However, if the super-cooled water droplets penetrate into the cavities of the surface features to result in a Wenzel wetting state (high S_{al}), ice nucleation will occur within the asperities. In such conditions, the degree of surface roughness will

affect the extent of ice adhesion strength. For example, the superhydrophobic coating of SH-c and SH-a shown in Figure 6.16 were both of high S_{al} and thus could be predicted to be in a Wenzel wetting state during super-cooled ice formation. However, due to the fact that the SH-c coating had a higher S_a (Figure 6.16), larger S_{ku} (Figure 6.14), and a more negative S_{sk} (Figure 6.13) as compared to SH-a, this meant that the features of SH-c coating was rougher with more inordinately deep valleys. Hence, the ice had a larger surface area to bond to which resulted in a higher ice adhesion strength than SH-a. A 3D topology image depicting the rough surface features and the presence of deep valleys of the SH-c superhydrophobic coating is shown in Figure 6.19.

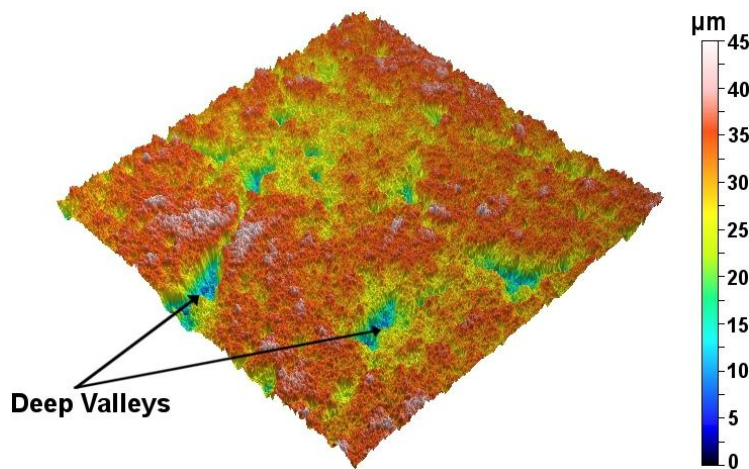


Figure 6.19 3D topology image of SH-c superhydrophobic coating. The image shows a rough surface with deep valleys.

6.4 Conclusions

A study of ice adhesion strength on hydrophobic and superhydrophobic surfaces was conducted based on a super-cooled water droplet impact experiment that was slightly modified from the one described in Chapter 5. In the previous experiment, the “defect” disc was found to introduce variability in test results. Hence, it was replaced with a thinner 50 μm “defect” disc for current tests which was determined to produce more consistent ice adhesion measurements. 15 different surfaces comprising of control, hydrophobic (commercial) and superhydrophobic surfaces (commercial & UVA nanocomposite) were tested. Results showed that the hydrophobic and superhydrophobic surfaces depicted different correlations between surface wettability parameters and ice adhesion strength. For hydrophobic surfaces, CA and RCA were determined to be a strong function of ice adhesion strength. Increasing CA and RCA with low S_a generally resulted in low ice adhesion strength. However, no correlation was found between CAH and hydrophobic ice fracture energies.

On the other hand, it was determined that ice adhesion strength for superhydrophobic surfaces correlated weakly with RCA (increasing RCA generally led to decreased ice adhesion strength) but did not correlate with CA and CAH. The effect of surface roughness parameters such as S_a , S_{sk} , S_{ku} and S_{al} on superhydrophobic ice adhesion strength was investigated. It was discovered that low

S_{al} values would result in low ice adhesion strength, vice-versa. This is due to the fact that the micron-sized features on low S_{al} surfaces are closely spaced which creates a high capillary pressure between the surface asperities. Therefore, it is able to resist the penetration of impacting super-cooled droplets to result in ice formation at a Cassie wetting state. In such scenarios, ice adhesion strength will be low since the formation of ice is limited at the tip of the features. However, if the surface asperities are infiltrated with water droplets (high S_{al} surfaces), the ice adhesion strength will be affected by secondary effects from S_a , S_{sk} , S_{ku} . In such conditions, surfaces that are rougher (high S_a) and filled with inordinately deep valleys (negative S_{sk}) will result in stronger ice adhesions strengths.

In conclusion, ice adhesion strength of certain superhydrophobic coatings (*Hydrobead 2*, ABS) were measured to be slightly lower than hydrophobic coatings and therefore could be considered as better ice-release surfaces. However, careful attention needs to be given to the fabrication techniques so that coatings of consistently low S_{al} could be produced. This is of importance since uncontrolled fabrication processes could result in huge variations of S_{al} and significantly increase ice adhesion strength.

Chapter 7

Microscopic Receding Angle Dynamics

7.1 Introduction

The study of drop impact and rebound dynamics (Chapter 4) as well as ice adhesion (Chapter 5 & 6) on superhydrophobic coatings revealed the significance of the receding angle in determining the degree of water and ice-repellency of these surfaces. Although apparent receding angles under dynamic conditions have been well studied, the microscopic receding contact line dynamics are not well understood. The study of receding line dynamics at the microscopic level could provide a deeper understanding of the characteristics of this wetting parameter, which could lead to a more successful implementation of superhydrophobic surfaces in anti-icing applications. This is the focus of this chapter.

Under the Cassier-Baxter and Wenzel wetting models, the affinity of water to a surface can be quantified by the CA, an equilibrium angle characterizing the three

phase contact line of water, surface and air. However, it has been universally agreed by researchers (and shown by current ice adhesion results in Chapter 6) that the sole use of CA is insufficient to describe the wettability of the surface¹³³⁻¹³⁷, especially within the context of practical applications of superhydrophobic surfaces such as self-cleaning. This was confirmed by Wang *et al.*¹³⁸ and Bhushan *et al.*¹³⁹ who reported the possibility of various non-wetting scenarios which include the Cassie, Wenzel, “gecko” and “rose petal effect” states. In all these cases, CA’s remain high. However, the mobility of a water drop on these surfaces varies. For example, a surface synthesized by Bhushan *et al.*¹³⁹ depicting a “petal effect” had a high CA of 152° but also displayed strong adhesion, to the point where a drop would stick to the surface even when tilted at 90 degrees. It is therefore clear that additional parameters would be required to quantify the state of superhydrophobicity of a surface.

To accomplish this, dynamic angles such as the ACA and RCA angles were prescribed.¹⁴⁰⁻¹⁴³ Consider the case where a drop rolls on a tilted superhydrophobic surface. For the drop to move forward, the leading edge of the droplet has to advance, creating an angle on the three-phase contact line called the advancing angle. On the other hand, the trailing edge of the drop retreats from the surface to form the receding angle. Both the advancing and receding contact line motions are highly dynamic, transitioning from one metastable state to another and have been extensively studied using theoretical¹⁴¹⁻¹⁴⁴, experimental^{134,145-154} and computational

methods¹⁵⁵⁻¹⁵⁷. Researchers have observed that the advancing three-phase contact line on superhydrophobic surfaces consisting of pillar geometries does not move, but rather descends upon its adjacent pillar to wet the top of the pillar surface.^{142-147,155}

The receding contact line on the other hand is forced to detach from one pillar to another in a discrete fashion, creating a pinning-depinning motion. Although the occurrence of this receding contact line detachment has been well documented¹⁴⁴⁻¹⁵², questions still remain on the precise dynamics and degree in which the receding line disjoins from one pillar to another. In fact, researchers have hypothesized conflicting scenarios for the receding mechanism. Gao and McCarthy¹⁴⁸ suggested that the contact line remains pinned on the entire pillar top until it instantly detaches to move towards the next pillar, after which it relaxes. Dorrer and R  he¹⁴⁶ proposed that the contact line remains pinned only on the very edge of the pillar before following a similar detachment and relaxation motion. Krumpfer *et al.*¹⁴⁵ hypothesized that the receding line would detach in a near vertical (tensile) manner to rupture the capillary bridge before leaving small sessile droplets on the de-wetted posts. However, Extrand¹⁴³ speculated that the contact line would travel along the pillar top in a horizontal direction prior to pinning at the edge and detachment. The inconsistency in these hypotheses signified the need for experimental measurements to validate these predictions, a necessity that was acknowledged by Patankar¹⁴⁴.

This was recently accomplished by Paxson and Varanasi¹⁵⁸, who were able to experimentally measure the dynamic behavior and angle of the microscopic receding contact lines along with its capillary bridge. A self-similar depinning mechanism of the drop at different length scales was also observed. However, due to poor temporal resolution, they were unable to resolve the depinning dynamics of the contact line. Hence, the exact dynamic behavior of the receding line remains unknown. Understanding the depinning mechanisms would not only improve our fundamental comprehension of adhesion and wettability of superhydrophobic surfaces at the microscopic level but would also have profound implications on practical applications such as anti-icing.

In this study, we present to the best of our knowledge, a first experimental investigation to measure the microscopic receding contact line dynamics of superhydrophobic surfaces with textured pillar and irregular surface features at micron length scales and at microsecond temporal resolution. The pillar superhydrophobic surfaces consisted of square micron-sized pillars spray coated with sub-micron PTFE particles while the irregular superhydrophobic surface was a nanocomposite coating. A drop was set in motion on these surfaces so that its three-phase receding contact line dynamics could be recorded using a high-speed camera for qualitative and quantitative analysis.

7.2 Experimental Methods

7.2.1 Fabrication of Textured Pillar Surface

The fabrication of textured pillar surface pillars involved various steps: spin-coating of photoresist SU-8 3050 (Microchem. USA) on a silicon wafer, soft-baking of the material followed by UV exposure with mask aligner, post-exposure baking and finally washed for development.^{159,160} Secondary roughness was then created by spray coating poly(tetrafluoroethylene) (PTFE) particles on the pillar tops. The concept of creating secondary roughness on top of a pillar surface for the creation of anti-wetting materials was also used by Gao *et al.*¹⁴⁸, Steele *et al.*¹⁶¹ and Cao *et al.*¹⁶². The existence of these two length scales on the pillar surfaces have been shown to relieve receding contact line pinning¹⁴⁸ and was hence utilized for this experiment.

The photoresist was first dispensed directly from the bottle onto a silicon wafer and spin-coated in two subsequent steps: (a) at 500 rpm for 10 s with spinning acceleration of 100 rpm/s and (b) at 4,000 rpm for 30 s with spinning acceleration of 300 rpm/s. The samples were then soft-baked at 100°C for 20 min on a hotplate, resulting in a film thickness of 33 μm . A soda lime mask of square-shaped patterns (42 μm) from Deltamask, Netherlands, at various inter-square distances of 63, 90, 105 and 120 μm were used for the exposure of the spin-coated samples. Patterning was performed by exposing the spin-coated material to UV radiation with a Karl-Suss MA6 mask aligner in hard contact mode with an i-line mercury lamp. An

exposure dose of 323 mJ was used to fully polymerize the SU-8 layer. The exposure was followed by a post-exposure bake on a hotplate at 65°C for 1 min and at 95°C for 5 min, in order to achieve complete cross-linking of the resist. The samples were then allowed to cool down in order to improve adhesion of SU-8 to the silicon wafer. Subsequently, the samples were washed with a SU-8 developer followed by rinsing with 2-propanol. As a result, four samples consisting of 33 μ m height, 42 μ m width square pillar structures at 63, 90, 105 and 120 μ m inter-pillar distances were obtained. A scanning electron microscope (SEM) image of a pristine 63 μ m inter-pillar surface is shown in Figure 7.1a.

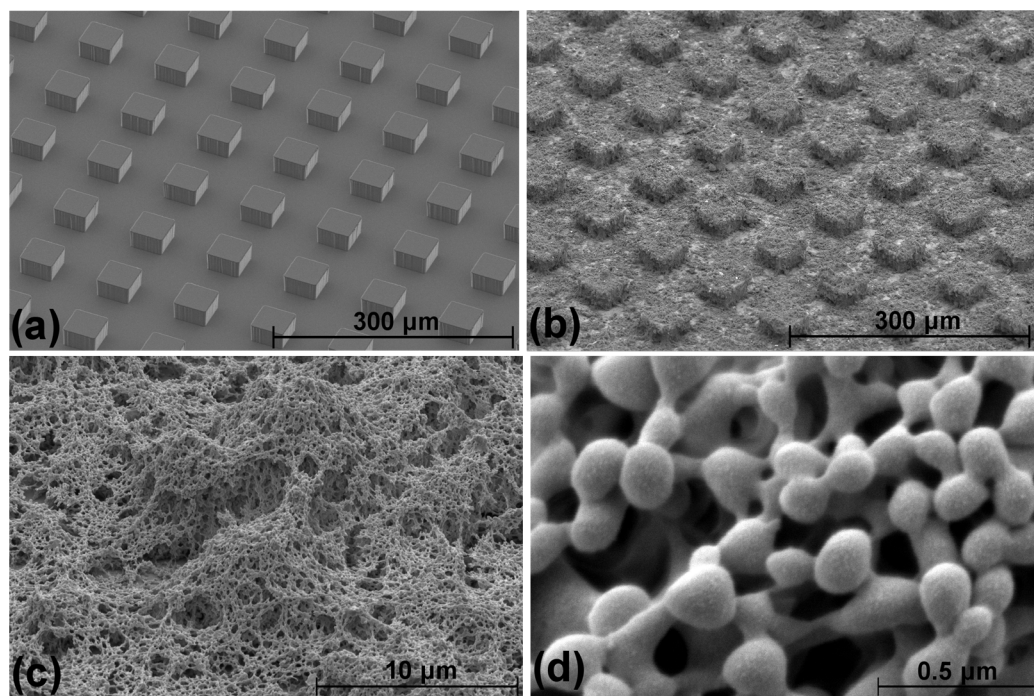


Figure 7.1 SEM images of a pillar surface at $L = 63\mu\text{m}$. (a) pristine surface prior to deposition of PTFE particles (b) superhydrophobic pillar surface after deposition of PTFE particles (c) 5000 \times magnified image of the PTFE particles on a pillar and (d) 80,000 \times magnified image of PTFE particles on a pillar.

3% wt. PTFE particles (200-300 nm diameter) were then dispersed in acetone via sonication and sprayed on top of the pristine SU-8-patterned pillars at approximately 10cm with an air-assisting nozzle. This process introduced submicron/nanoscale roughness on top of the pillars and rendered the surface superhydrophobic. The Scanning electron microscope (SEM) images of a surface (63 μm inter-pillar spacing) at pre- and post-spray are shown in Figures 7.1a and 7.1b, respectively. In addition, SEM images of the submicron particles on top of a single pillar are shown at two magnification levels in Figures 7.1c and 7.1d. The apparent equilibrium contact, advancing, receding and roll-off angles for the four pillar surfaces as well as for the unstructured superhydrophobic surface described in the next section were measured using a goniometer (Model 250, Ramé-Hart, USA) with a 10 μL water drop.

The apparent advancing and receding angles of the pillar surfaces in Table 7.1 showed different correlations with the length of inter-pillar spacing (L). The advancing angle remained independent of L and ranged between 160° to 166° for all pillar samples. However, the receding angle was found to increase with larger L distances. At a maximum L of 120 μm , the receding angle was measured to be 140° as compared to 127° for an L of 63 μm . These correlations were consistent with results reported from previous experimental and computational studies.^{133,134,146,156,163}

In addition, the roll-off angle of the surfaces were found to be inversely proportional

to L , a relation that was in agreement with the force balance equation for a drop at an inclination prescribed by Yeh *et al.*¹³³ It should be noted that these apparent angles were measured using the tilt method and acquired at the incipient of drop motion, a measurement method that is widely recognized and accepted by researchers.¹⁶⁴

Type	Interpillar Distance (μm)	Contact Angle ($^\circ$)	Advancing Angle ($^\circ$)	Receding Angle ($^\circ$)	Roll-Off Angle ($^\circ$)
Pillar	63	152.0	160.6	126.9	17.3
Pillar	90	152.0	162.2	137.5	16.1
Pillar	105	155.9	167.9	139.1	12.1
Pillar	120	156.3	166.1	140.4	8.9
Irregular	N/A	154.3	156.2	146.9	3.1

Table 7.1 Apparent measurements of the superhydrophobic performance of the textured pillar and nanocomposite surfaces.

7.2.2 Fabrication of the Nanocomposite Surface

As with all nanocomposite coatings used in this dissertation, the irregular superhydrophobic surface was created by spray-casting precursor solutions on aluminum substrates followed by thermosetting to produce the final nanocomposite coatings.

The nanocomposite formulation used for this experiment was similar to the one described in Section 2.2.1. The same amount of montmorillonite clay particles and waterborne fluorinated acrylic copolymer was used. However, the polyurethane

component of the formulation was not included. This formulation was spray-casted and heat cured to result in an approximately 100 μm thick superhydrophobic nanocomposite coating depicting irregular but hierarchal surface features. This is seen in the SEM images shown in Figures 7.2a and 7.2b which revealed a surface texture at different length scales, with sub-micron sized features embedded within micron sized structures.

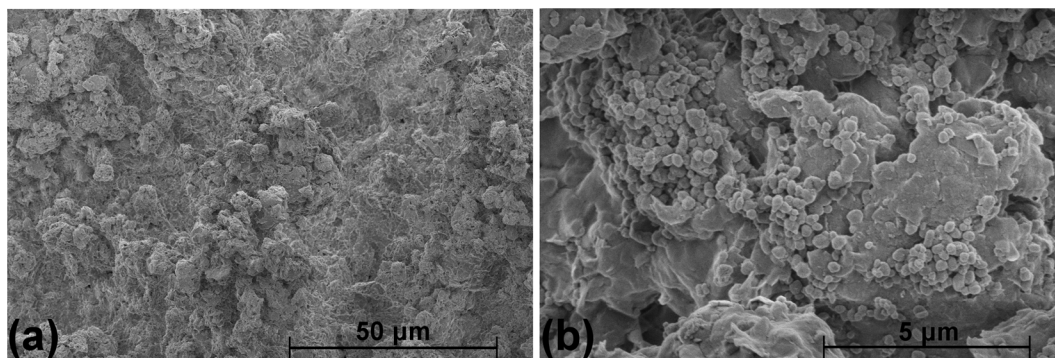


Figure 7.2 SEM images of a nanocomposite superhydrophobic surface. (a) 1000 \times magnified image and (b) 20,000 \times magnified image.

7.2.3 Experimental Set-Up

Schematics of the experimental set-ups are shown in Figure 7.3. As shown in the figure, there were two methods in which the drop was advanced and receded across the superhydrophobic surfaces. The first method (Figure 7.3.1) involved placing the textured pillar surface on a high precision rotation stage (PRM-1, Thorlabs, USA) and manually tilting it at an approximate rate of 3.5 degrees/s to

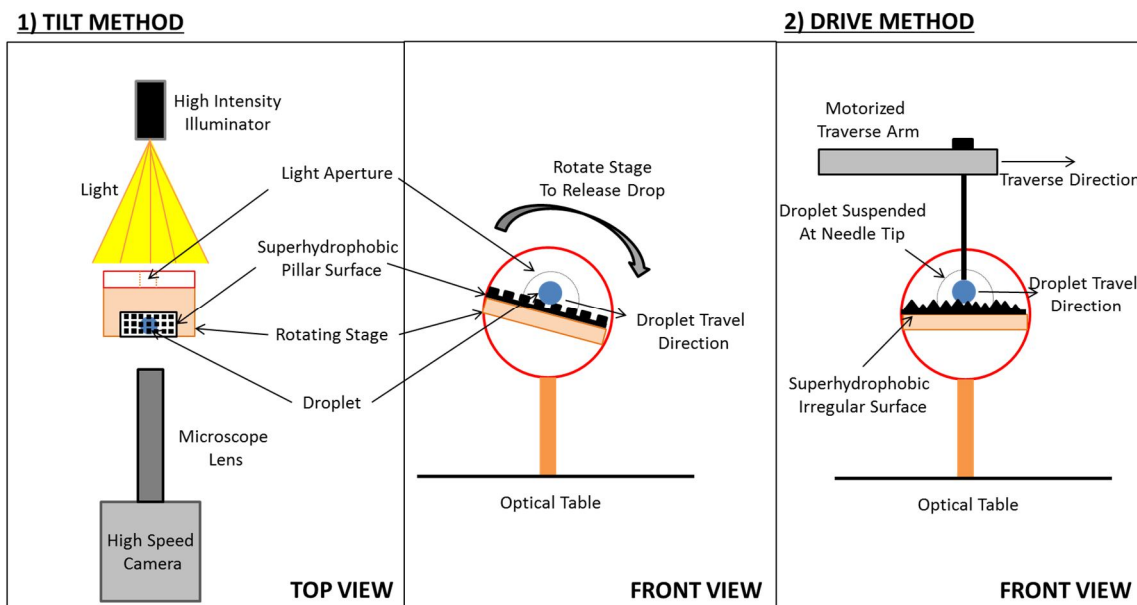


Figure 7.3 Schematic of the experimental setup depicting the tilt method and driving method.

allow a water drop (10 μL) to roll from the surface. High magnification optics coupled with high-speed imagery was utilized to record the dynamics of the microscopic receding angle while the droplet was traveling down the inclination. This was accomplished by attaching a microscope lens (6.5X UltraZoom fine focus with 2X F-mount adapter and 2X Lens attachment, Navitar, USA) to a high speed camera (Fastcam SA-4, Photron, Japan). Under the back-lighting of a high intensity fiber optic illuminator (MI-150, Dolan-Jenner, USA) and through the aperture of the rotating stage, high contrast images of the microscopic receding contact line motions on each pillar were acquired at 15,000 frames/s (66 μs between each frame). The entire set-up was constructed on top of an optical table to reduce external vibrations that could potentially introduce noise to the measurements.

However, due to difficulty in acquiring acceptable image resolution on the nanocomposite coating with the tilt method, the drop was suspended at the tip of a needle which was attached to a motorized traverse arm (Xslide, Velmex Inc., USA) and driven horizontally across the surface. This is shown in Figure 7.3.2. The speed of traverse was set at 5.8 cm/s and was prescribed based on preliminary measurements of the drop roll-off speed on the coating at tilt. Once the drop was in motion, the progression of the microscopic receding angle on the surface features were recorded using the same imaging techniques used for the pillar surfaces. This experimental technique involving a driven drop was also used in a recent receding angle study by Paxson and Varanasi.¹⁵⁸

7.3 Results and Discussion

7.3.1 Textured Pillar Surface

Figure 7.4 shows the images depicting the first and last 0.26 ms of the receding line motion on a single pillar for a surface with an L value of 63 μm . These images represent the key events during a single cycle of dynamic interaction between the receding line and the pillar. It can be observed that the receding line was initially (at $t=0$ s) relaxed and had a high contact angle. However, it rapidly (within 0.13 ms) transitioned into a stage where the contact line was stretched and pulled

inwards to form a concave shape as it traversed across the top of the pillar surface. The travel of the receding line between the duration of 0.26 ms and 1 ms was however limited, and only occurred over a small interface distance. Necking of the receding contact line would eventually start to occur after $t=1$ ms with the formation of instabilities on areas of the drop located within close proximity to the pillars and the pinned contact line. These instabilities were due to drop vibrations triggered by the de-pinning process of the receding contact line. They were depicted as bright slit lines on the images and were formed as a result of light penetration from the back-lighting. The receding line was further stretched until the very last moment at $t=1.26$ ms before the rupture and collapse of the capillary bridge. This caused the receding line to “snap” and advance to the adjacent pillar.

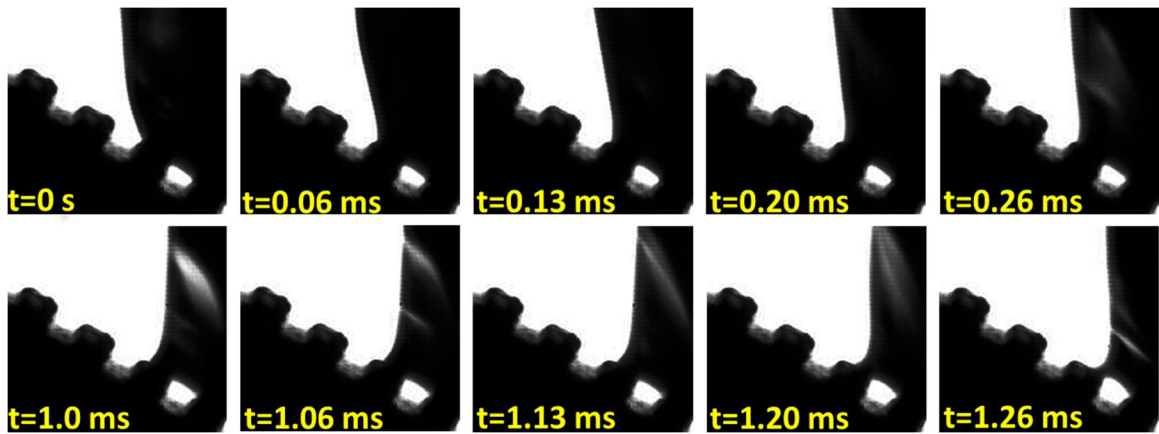


Figure 7.4 Sequence of images depicting the first and last 0.26 ms of the microscopic receding line motion on a pillar surface ($L=63\ \mu\text{m}$) while at tilt.

The dynamics of the receding line were analyzed in detail at the microscopic level by tracing it from the point where it intersects the pillar to a location along the length of the contact line situated approximately $10\text{ }\mu\text{m}$ away from the intersection. This was performed on all of the receding line images (recorded at a temporal resolution of $60\text{ }\mu\text{s}$) that were acquired on a single pillar in the experiment. They were then reconstructed in a single plot and superimposed on a pillar outline to represent the onset, progression and ultimately “snapping” of the receding line on a pillar in a precise two dimensional space. This is shown in Figure 7.5a and 7.5b for pillar surfaces with L values of 63 and $120\text{ }\mu\text{m}$, respectively. This deconstruction of the receding line motion provided detailed information about the variation of its microscopic three-phase angle as well as its spatial and temporal dynamics, all of which would be comprehensively analyzed herein. It should be noted that the receding direction in the figure is to the right. The values labeled in the figure indicate the corresponding initial and pre-snap receding lines with the higher value representing the number of frames required to capture the complete receding line motion on a pillar. The time required for the receding line to travel from its initial to a pre-snap position was also labeled. It can be observed that the receding line remained much longer on the pillar surface where $L=120\text{ }\mu\text{m}$ (Figure 7.5a), as compared to the one at $63\text{ }\mu\text{m}$ (Figure 7.5b), an observation that will be addressed in the later parts of this discussion.

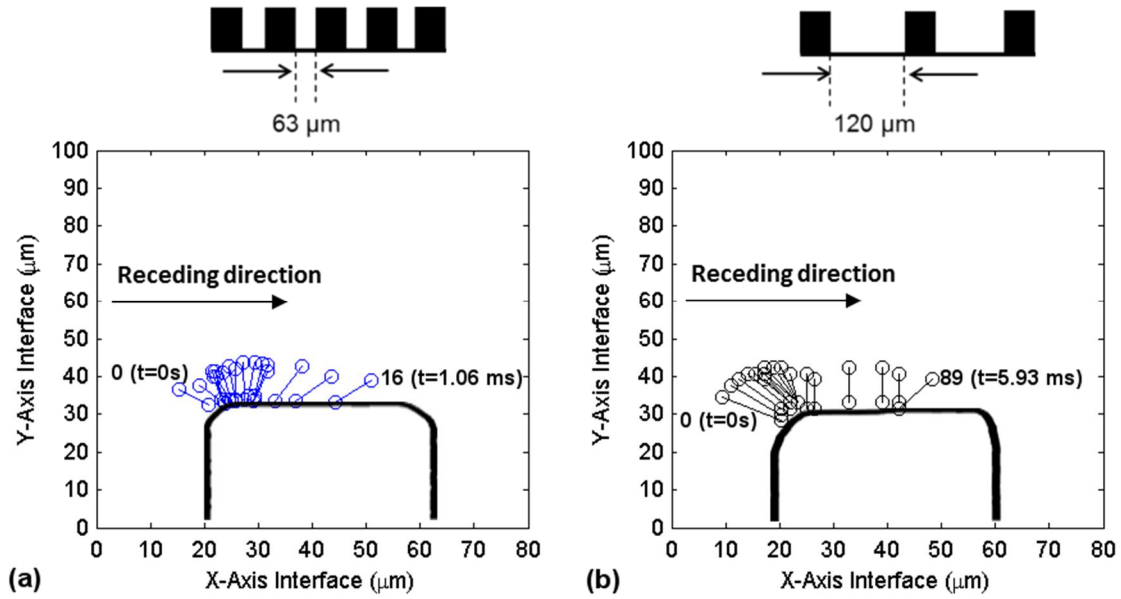


Figure 7.5 Sketches of the position of individual microscopic receding lines on a pillar from the receding line onset until point of “snapping” for surfaces (a) $L = 63 \mu\text{m}$ and (b) $L = 120 \mu\text{m}$.

Spatial analysis of the receding line motions in Figure 7.5a and 7.5b revealed no substantial differences in its travel path between pillar surfaces of $L = 63 \mu\text{m}$ and $120 \mu\text{m}$. At the onset of the receding motion, the three-phase line was in contact with the lower left edge of the pillar, after which it would quickly travel around the edge to arrive at the pillar top surface. The receding contact line would then move horizontally along the length of the pillar top in small increments (approximately $1 \mu\text{m}$ per frame) for an extended period of time. This resulted in a receding line travel that was concentrated on a horizontal area close to the left edge of the pillar. The receding line would however abruptly advance in larger increments and release itself from the pillar at approximately mid-distance between the left and right edges of the

pillar top surface. However, due to limitations in the temporal resolution of the camera, the precise location of receding line “snapping” could not be determined. There is a possibility that the microscopic receding line had further traveled (within the last 0.06 ms) to the right edge of the pillar before detachment at that location. In any case, there were substantial differences between the receding line spatial dynamics acquired in this experiment with hypotheses obtained from previous studies. Majority of the researchers have proposed a “stick-slip” motion of the microscopic receding line when traveling from pillar to pillar.^{140,144-146,148} However, based on current experimental observations, we propose that the receding dynamics of the microscopic receding line more closely resembled a “slide-snap” motion. Although Extrand¹⁴³ did correctly predict the “sliding” motion of the receding contact line, it was suggested that the receding line would be pinned at the edge before being gradually pinched and ruptured. This was not observed in the current experiment.

The microscopic receding line contact angles on the pillar surface as they progressed from one pillar to another were individually measured for four consecutive pillars and for all pillar surfaces ($L = 63, 90, 105$ and $120\ \mu\text{m}$). The angles were then plotted with respect to time as shown in Figure 7.6. Results show significant variation (90 degrees and above) between the angle measured at the onset of the receding motion (the maximum angle) and the angle measured right before the

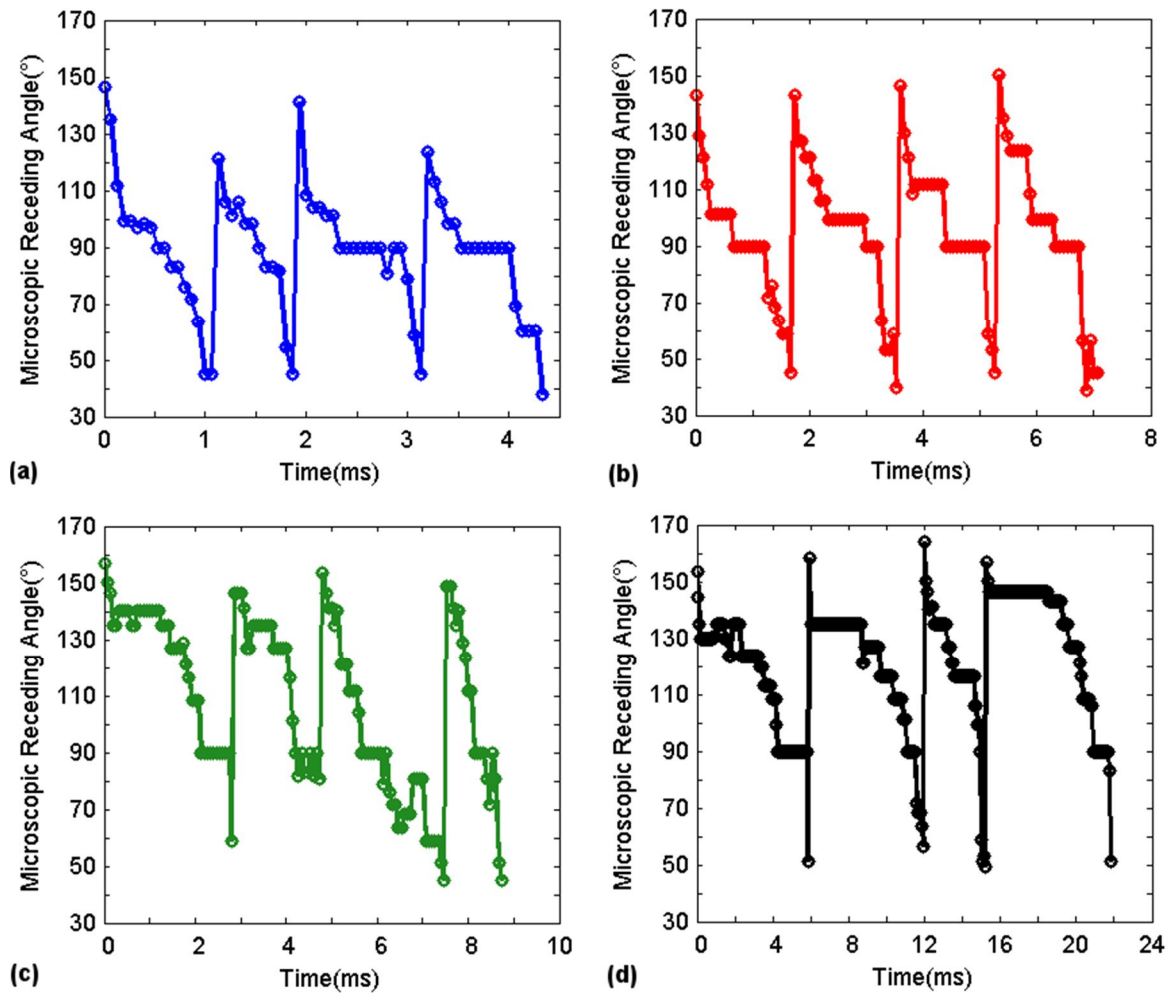


Figure 7.6 Measurements of the angles of each receding contact line as a function of time for a length of four pillars. Surfaces consist of (a) $L = 63 \mu\text{m}$ (b) $L = 90 \mu\text{m}$ (c) $L = 105 \mu\text{m}$ and (d) $L = 120 \mu\text{m}$.

snapping of the receding line (the minimum angle). After the detachment of the receding line from the pillar, the angle of the contact line would abruptly increase as a new cycle of receding line motion commenced on the adjacent pillar. These receding angle dynamics were observed to be reasonably repeatable for each pillar and for all surfaces ($L = 63\text{--}120 \mu\text{m}$). The low angles ($40\text{--}60^\circ$ for all surfaces) of the pre-snap receding angles suggest a strong affinity of the liquid on the textured

pillars. This is hypothesized to be due to the edge effects introduced by the textured pillars. This observation correlates with the study of Bhushan *et al.*¹⁶³ who reported the pinning of a drop at the pillar edges. If the pillars were hydrophobically functionalized to produce a smooth top surface, the pre-snap receding angles can be expected to be higher.

The microscopic receding angles from all four pillars were averaged and plotted with respect to its non-dimensional time, t^* , prescribed as $(t-t_0)/T$, where t , t_0 and T represents the current, initial and total duration of receding line travel on a single pillar, respectively. In addition, averaged apparent receding angles of the surfaces which were acquired at the apparent (millimeter) length scales were plotted with the microscopic results. This is shown in Figure 7.7 for all pillar surfaces. The differences in the receding angle between an apparent and microscopic measurement was observed to be substantial. While the initial measurements of the onset receding angle for the apparent and microscopic methods yielded similar values, it would however diverge as the receding line progressed across the pillar surface. This was not unexpected; the initial receding angle did not involve any complex motions and could be measured without difficulty regardless of length scales. However, once progressed, the macroscopic field of view was insufficient to accurately capture the intricate motions of the three-phase line on each pillar, resulting in a divergence. Therefore, while the fluctuation of the angles from a microscopic measurement would

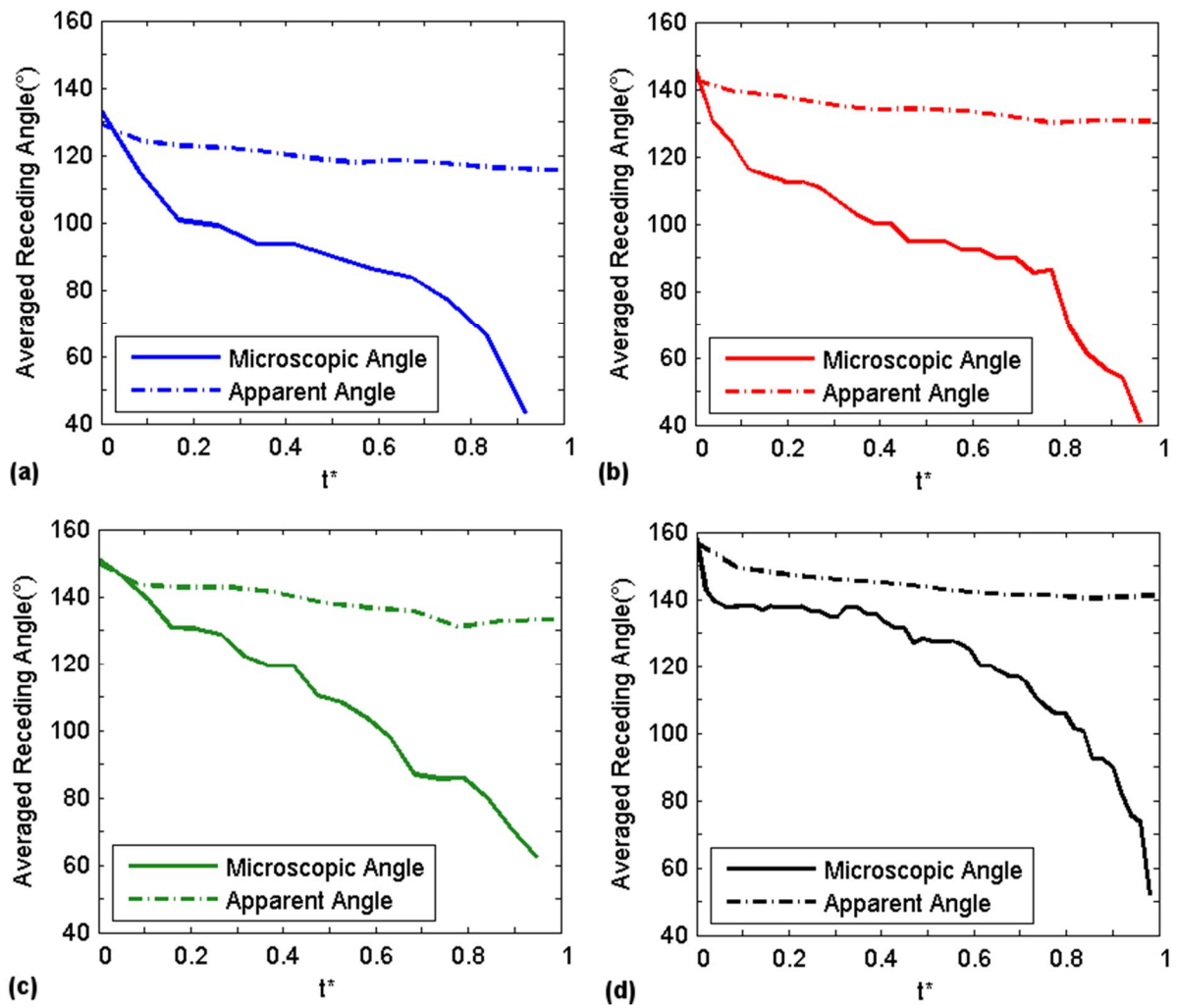


Figure 7.7 Averaged microscopic and apparent receding angles acquired for a distance of four pillars as a function of non-dimensional time ($t^* = (t - t_0)/T$) where t , t_0 and T represents the current, initial and total duration of receding line travel on a single pillar, respectively.

exceed 90° , the variation in apparent angles for all surfaces was consistently limited to within 20° . The variation in magnitude of the apparent angles was consistent with previous studies at similar length scales.^{152,157}

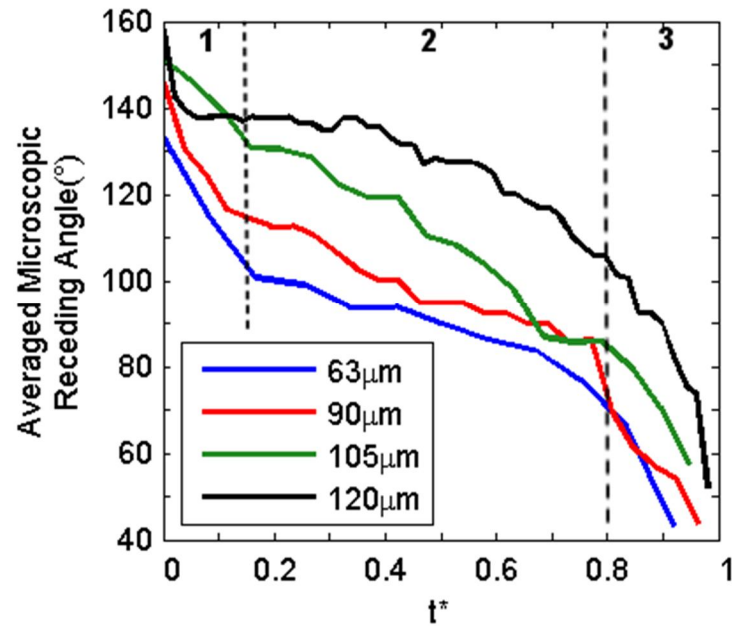


Figure 7.8 A comparison of the averaged microscopic receding angles for all pillar surfaces at varying L distances as a function of non-dimensional time ($t^* = (t - t_0)/T$) where t , t_0 and T represents the current, initial and total duration of receding line travel on a single pillar, respectively.

A comparison of the averaged microscopic receding angles for all pillar surfaces at different L values was conducted and shown in Figure 7.8. The dynamics of the receding angles as it travelled on the pillar top to the point of detachment could be categorized into events that occurred in three time segments. These segments were labeled as areas 1 to 3 in Figure 7.8. In the first segment, the receding contact angle decreased at a high rate of descent. However, at the second time segment which constituted approximately 65% of the total duration of receding line travel, the decrease would be much more gradual. Once in the third and final segment, the receding angles would sharply decrease again until the point of de-

pinning. It should be noted these time segments corresponded with the occurrence of the three receding line motion characteristics previously described for Figure 7.5a and b, i.e., a quick receding line travel around the left edge of the pillar, a short interface traverse distance on the pillar top and an abrupt receding line advancement in larger spatial increments until the point of detachment.

In addition, it could be observed that as L increased, the curve line shifted upwards, resulting in larger initial receding angles (at $T^* = 0$). The pre-snap receding angles ($T^* > 0.9$) also showed a tendency to increase with L . This was caused by the length of the capillary bridge. At smaller L distances, the shorter capillary bridge interacts with its adjacent capillary bridges and affects the deformation of the receding line.¹⁵⁸ This meant that the initial receding line on a pillar was unable to relax, and therefore had lower receding angles. This is in contrast to when pillars were spaced further apart and where interactions between pillars were kept to the minimum, which led to higher receding angles at the beginning of receding motion. A similar explanation could be made for the pre-snap receding lines; Receding lines were able to detach at larger angles at larger L 's, as compared to being stretched to a lower angle when under the influence of a nearby capillary bridge.¹⁵⁶ As previously mentioned, the apparent receding angles (Table 7.1) were also found to be linearly proportional to L , albeit at different magnitudes.

A measurement of the interface travel speed for apparent (macroscopic) and microscopic receding lines for all pillar surfaces was performed (Figure 7.9). These two travel speeds are defined in Equation 7.1 and 7.2.

$$V_{\text{apparent}} = \frac{4(W + L)}{\sum_{n=1}^4 t_n} \quad (7.1)$$

$$V_{\text{microscopic}} = \frac{4W}{\sum_{n=1}^4 t_n} \quad (7.2)$$

where W is the width of the pillar, L is the inter-pillar distance and t the time required to traverse specific pillars denoted by the subscript numbers. Therefore, the apparent interface travel speed was evaluated over a distance of 4 pillar widths and inter-pillar distances, while the microscopic interface travel speed was based on the average time required to travel a single pillar width.

Results in Figure 7.9 show a similar trend for both apparent and microscopic measurements, i.e., a decrease in interface speed with increasing L , albeit at different magnitudes. This was caused by the shorter duration of travel on a pillar with small L values, as compared to a longer travel duration on a pillar with large L values. This was previously observed in Figures 7.5a and 7.5b and could be attributed to the tangential component of the gravity force that is exerted on the drop. As reported in Table 7.1, the ROA of the $L=63 \mu\text{m}$ surface is a factor of two of the ROA of an

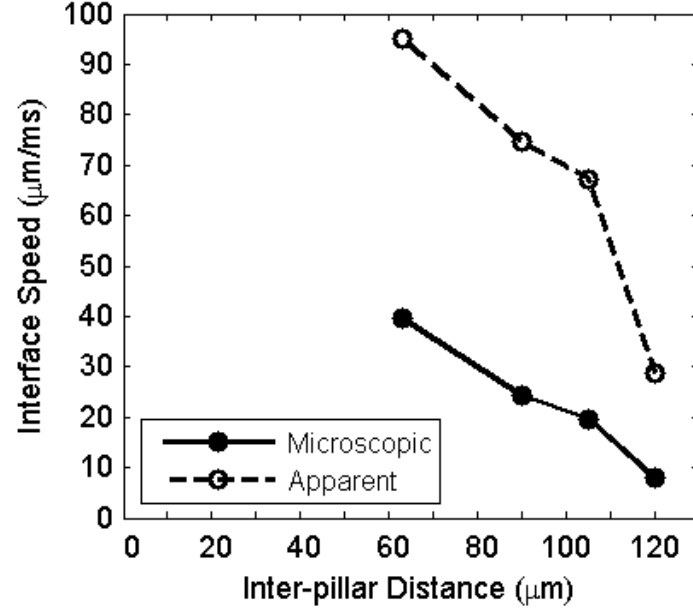


Figure 7.9 Averaged travel speed of the apparent and microscopic receding lines as a function of inter-pillar distance.

L=120 μm surface. As such, the drop on the L=63 μm surface was subjected to a stronger downward force and therefore released from the surface at higher speeds. This effect could also be showed by considering the force balance equation of a drop on a superhydrophobic surface described in Equation 7.3 where the tangential force exerted on the drop is balanced with its frictional force.

$$mg \sin(ROA) - \mu_{pillar} \phi_s mg \cos(ROA) = ma \quad (7.3)$$

where m is the mass of the drop, g is gravity, μ_{pillar} is the coefficient of dynamic friction, ϕ_s is the solid area fraction of the surface, and a is the acceleration of the drop.¹⁶⁵ Since the measurements were performed at the onset of drop rolling, the acceleration of the drop was considered to be negligible. Equation 7.3 was then

reduced to describe the coefficient of dynamic friction as a function of ROA and solid area fraction. This is shown in Equation 7.4.

$$\mu_{pillar} = \frac{\tan(ROA)}{\phi_s} \quad (7.4)$$

Equation 7.4 was evaluated for all pillar surfaces and results were plotted in Figure 7.10. Results show that the coefficient of dynamic friction experienced by the drop for all pillar surfaces is approximately constant. Therefore, this indicates that a surface with a decreasing solid area fraction will be accompanied by a decreasing ROA as well, an observation which is consistent with the trends that were measured in the experiment.

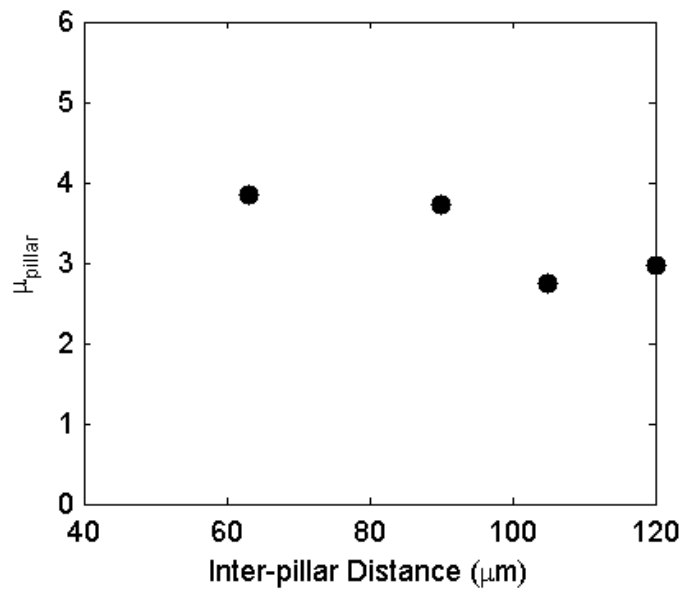


Figure 7.10 Coefficient of dynamic friction of pillar surfaces

7.3.2 Irregular Nanocomposite Surface

The study of microscopic receding line motion was extended on a nanocomposite surface with irregular, hierarchal surface features at the micro- and nano- length scales. An analysis of the deconstructed receding lines on the surface features similar to Figure 7.5 was performed with results shown in Figure 7.11. As with the earlier investigation on pillar surfaces, the receding direction was to the right. Since the features did not consist of repeatable patterns like the pillars, they were specified based on the locations of initial and pre-snap receding lines which were labeled accordingly in the figure. We observed general similarities of the receding line motion of this irregular surface with the pillar surfaces. The occurrence of “slide-snap” was preserved. Distinct angle variations of the microscopic receding

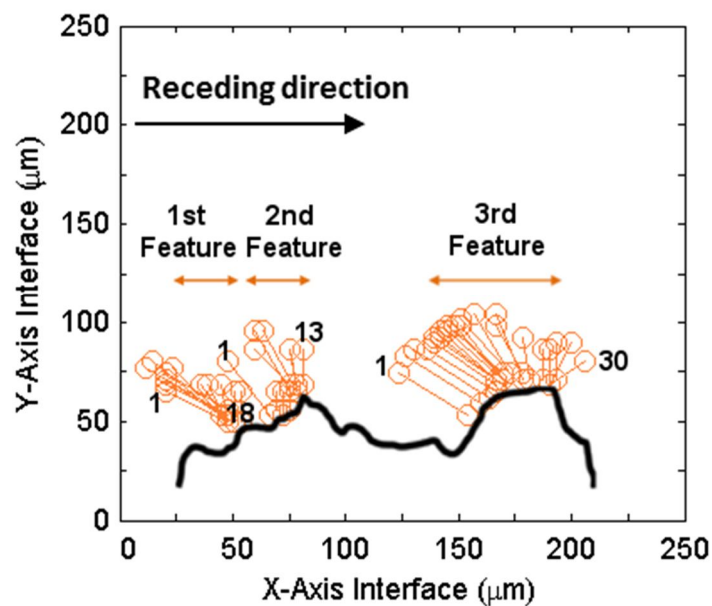


Figure 7.11 Sketches of the position of individual microscopic receding lines on an irregular nanocomposite coating from the receding line onset until point of “snapping”.

line as it slid on a feature were also observed. This is shown in Figure 7.12.

However, some differences were noted. For example, the distance of travel of the receding line on the first and second feature was less pronounced as compared to the case of pillar surfaces. Moreover, the pre-snap receding angles for these features were measured to be much higher at 90° . (Figure 7.12) The reason for this difference was attributed to the shape and contact area of the features. Surface structures that exhibit distinct pointed ends will have a smaller exposed area for wetting and attachment and therefore will depict receding motion at a localized area with higher angles right before detachment. This corresponds with the hypotheses from Krumpfer *et al.*¹⁴⁵ and Priest *et al.*¹⁵³ who predicted a high receding angle outcome for surfaces with needle-like structures or posts containing conical tops. This

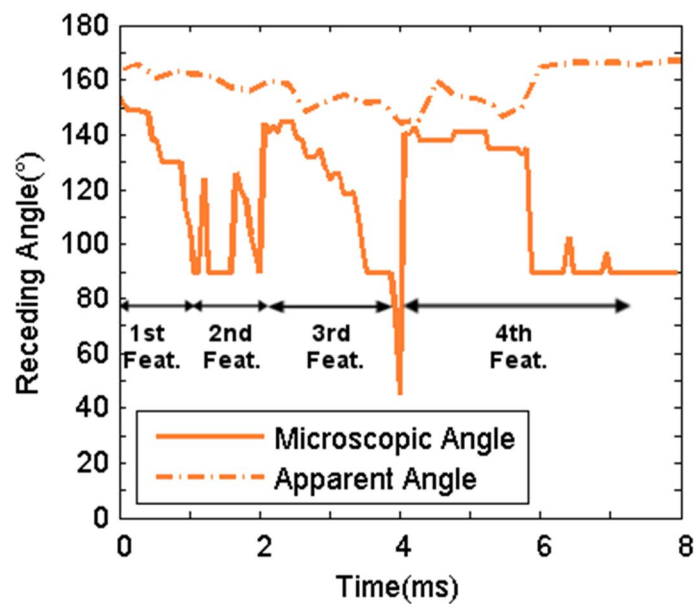


Figure 7.12 Measurements of the angles of each receding contact line as a function of time for a length of four irregular surface features.

discovery was further validated by comparing these receding dynamics to the third feature shown in Figure 7.11. The structure of this feature consisted of a flatter top and had a width of approximately 40 μm , hence bearing physical resemblance to the pillar surfaces that were previously investigated. It could be observed that its receding line dynamics were consistent with measurements that were previously acquired, i.e., the sliding of the receding line across the horizontal top of the feature followed by a detachment at 45 degrees. Therefore, this confirms the influence of the feature structure on the microscopic receding angle dynamics.

7.3 Conclusions

The study of microscopic receding line motion acquired at microsecond time resolution on pillar and irregular nanocomposite superhydrophobic surfaces revealed contact line dynamics that were previously not reported. The receding line progressed from the lower edge of a pillar, across the length of the pillar top before “snapping” to advance to the adjacent pillar, creating a “slide-snap” motion. This is in contrast to the “stick-slip” motion that was reported in previous studies. The variation of the microscopic receding angle for this entire sequence of motion was measured to be significant with a difference of approximately 90° between the angles measured at the initial and pre-snap of the receding line. Similar measurements performed at the macroscopic level would only yield a difference of approximately

20°. This observation was consistent for all investigated pillar surfaces with varying L distances. The microscopic receding angles were however found to generally increase with larger L distances which were due to capillary bridge effects. This relationship was also discovered to be maintained with apparent measurements. Therefore, these results showed self-similarity at the macroscopic and microscopic levels. The apparent and microscopic interface travel speeds were both found to be inversely proportional to L. This was due to the fact that the roll-off angles for surfaces with smaller L values were larger which resulted in a stronger exertion of tangential gravity force on the drop.

In addition, similar experiments performed on a nanocomposite surface revealed a similar “slide-snap” motion of the microscopic receding line. However, due to the sharper features of the surface, the receding line was found to be limited to a shorter sliding distance. Moreover, the angle of the receding line prior to detachment was measured to be higher (at 90°) as compared to the pillar surfaces.

Chapter 8

Conclusions

8.1 Fabrication & Durability of Nanocomposite Coatings

A spray-casting method where a substrate was traversed in controlled longitudinal and lateral motions while under the impact of nanocomposite slurry droplets was developed. This resulted in improved consistency of the quality of the nanocomposite coatings. In addition, the effect of spray-casting heights and air pressures on the superhydrophobicity and durability of the coatings were investigated. Results revealed the tradeoff nature of the superhydrophobicity and durability of nanocomposite coatings fabricated from the spray-casting technique, i.e., increasing the spray height and decreasing the spray pressure (increasing droplet flight time) improves superhydrophobic performance but is accompanied by a decrease in wear durability. On the other hand, decreasing the spray height and increasing the spray pressure (decreasing droplet flight time) increases the strength

of the coating but decreases its superhydrophobicity. By balancing these parameters, a combination of durability and superhydrophobicity can be achieved.

8.2 Temperature & Humidity Effects

The effect of temperature and humidity on the wettability of the nanocomposite coating was studied (with CA and ROA measurements for a single static drop) for a full temperature cycle from 20 °C to -3 °C and back to 20°C, at both low and high humidity conditions, while maintaining homogeneous thermal conditions (equal air, nanocomposite surface and water temperatures). It was shown that superhydrophobicity was maintained for a full temperature cycle at low *and* high humidity conditions, so long as the environmental conditions remained thermally homogeneous. In non-thermally homogeneous conditions, even the slightest differences in air and nanocomposite surface would result in condensation, which led to superhydrophobic degradation.

8.3 Drop Impact & Rebound Dynamics

An experiment was conducted to investigate the dynamics of a single water drop oblique impact and rebound, on a 45° inclined nanocomposite surface, and at various thermally homogeneous temperatures (50°C to -8°C). The effect of higher

fluid viscosities on impact and rebound dynamics was also studied by utilizing water-glycerol mixtures. The ranges of drop We_N and Oh that was achieved were from 9 to 67 and 0.0018 to 0.028, respectively. Results showed that super-cooled drops were repelled from the surface without ice nucleation. In addition, drop contact times were found to be generally independent of drop velocity or surface inclination. However, the surface inclination affected the non-dimensional maximum spread of the impacting drop for conditions where $We_N > 30$. At even higher $We_N (> 60)$, asymmetry effects induced by the inclination were found to accelerate the breakup of the drop. The rebound dynamics of the drop was also found to be a strong function of RCA and viscosity and could be categorized into eight outcomes, i.e., symmetric, asymmetric, irregular, irregular with breakup, bulbous, tail impingement and tail impingement with breakup.

8.4 Ice Adhesion Strength with Thick and Thin “Defects”

The ice adhesion strength of hydrophobic and superhydrophobic coatings were studied by accreting ice on the substrates under the impact of 20 μm super-cooled water droplets at an air temperature of -20°C . The ice was removed via a tensile loading, fracture toughness test initiated by “defect” discs on the substrate and by the force of air pressurization. Two “defect” thicknesses were used: a 1 mm

(thick) disc and a 50 μm (thin) disc. Results from the thick “defect” showed that in general, as compared to control substrates, hydrophobic and superhydrophobic surfaces can reduce ice adhesion strength. However, due to the thickness of the “defect” disc, no correlation between surface wettability parameters and ice adhesion strength was observed. As a result, it was replaced with a thin “defect” disc. New results obtained with the thin “defect” showed that for hydrophobic surfaces, regardless of underlying substrate material, ice adhesion strength decreased with an increasing RCA. However, no correlation between CAH and ice adhesion strength was observed. Similar results were observed for superhydrophobic surfaces, albeit with a weaker relationship between RCA and ice adhesion. A study of the superhydrophobic surface roughness parameters revealed that its ice adhesion strength was proportional to S_{al} . Effects from S_a , S_{sk} , S_{ku} were secondary and dependent on the wetting state of the coating after impact of the super-cooled droplets.

8.5 Microscopic Receding Angle Dynamics

The dynamics of the microscopic receding angle on textured pillar surfaces at varying interpillar distances and on an irregular nanocomposite coating was studied at micro-second temporal scales. Results revealed a “slide-snap” motion of the

receding contact line on the pillar surfaces, as compared to the “stick-slip” dynamics that were reported in literature. A measurement of the microscopic receding angles showed consistently large variations (up to 90°) between the initial and pre-snap receding lines. The microscopic receding angles were found to generally increase with larger interpillar distances. A similar study on irregular surfaces showed that the “slide-snap” motion of the receding line was preserved. However, due to the sharper surface features, the interface angle of the pre-snap receding line was discovered to be higher.

8.6 Contributions of Dissertation and Recommendations

This dissertation has systematically studied the issues pertinent to the application of superhydrophobic coatings as an ice-repellent surface. For example, the parameters controlling the balance of superhydrophobicity and durability of the nanocomposite coating fabricated by the spray-casting technique were studied. This is of practical importance. For a superhydrophobic surface to be successfully implemented as an effective ice mitigation tool in aerospace applications, a coating with the combination of high level durability and superhydrophobicity is desired. As far as the author is concerned, no previous publications have investigated this issue.

Static drop studies also revealed the importance of isothermal conditions in maintaining wettability of the superhydrophobic surfaces at various environmental conditions. In addition, results obtained from the dynamic drop studies on inclined surfaces revealed impact and rebound characteristics that were not previously reported. As described in section 5.1, conflicting conclusions on the effectiveness of superhydrophobic surfaces in reducing ice adhesion were reported from previous studies. Results from the current ice adhesion experiment provided reasons for the conflicting reports and also revealed the importance of surface autocorrelation length parameter in controlling ice adhesion strength. Lastly, the microscopic depinning motion of the RCA on superhydrophobic surfaces, which was discovered to be a crucial wettability parameter for low ice adhesion performance, was studied at microsecond temporal scales. Therefore, the results from this dissertation have advanced the community's knowledge and understanding of the relationship between icing and superhydrophobicity.

However, further work is needed. The studies that were conducted in this dissertation were performed at low drop impact speeds. Ice accretion in aerospace applications typically occurs at much higher impact velocity conditions (50-90 m/s). In such situations, the effect of the impact and rebound characteristics of a supercooled droplet on a superhydrophobic surface is not well understood. A fundamental study similar to the one described in Chapter 4, but at higher impact speeds and at

representative droplet sizes (20-100 μm) will therefore be of value. In addition, the surface inclination should be further varied to study the effects of oblique surface angles on droplet impact and rebound dynamics.

Extended studies of ice adhesion strength on superhydrophobic surfaces at high impact droplet velocities are also desired. This is to determine the effectiveness of the coating in resisting ice adhesion at realistic aerospace icing conditions. As described in Chapter 6, the superhydrophobic ice adhesion strength is dependent on S_{al} value of the coating. For the ice adhesion experiment conducted in this dissertation (low impact speeds), a S_{al} value within the range of 20-40 μm was found to be sufficient for the resistance of penetration of impacting droplets into the surface asperities. However the relationships between S_{al} , higher droplet impact speeds and ice adhesion strength are not well understood and therefore should be carefully studied.

In addition, an improvement of the current nanocomposite fabrication methods for the production of superhydrophobic coatings with consistent S_{al} values is required. Current fabrication techniques, even with a controlled spray-casting process, were found to result in coatings with varying S_{al} values. This is hypothesized to be due to the effects of environmental temperature, humidity as well as spray-casting droplet sizes. A study of these effects on coating S_{al} will therefore be of interest.

References

1. Barthlott, W.; Neinhuis, C. Purity of the sacred lotus, or escape from contamination in biological surfaces. *Planta* 1997, *202*, 1-8.
2. Feng, X.; Jiang, L. Design and creation of superwetting/antiwetting surfaces. *Adv Mater* 2006, *18*, 3063-3078.
3. Ma, M.; Hill, R. M. Superhydrophobic surfaces. *Current Opinion in Colloid & Interface Science* 2006, *11*, 193-202.
4. Kim, S. H. Fabrication of superhydrophobic surfaces. *J. Adhes. Sci. Technol.* 2008, *22*, 235-250.
5. Tserepi, A.; Vlachopoulou, M.; Gogolides, E. Nanotexturing of poly (dimethylsiloxane) in plasmas for creating robust super-hydrophobic surfaces. *Nanotechnology* 2006, *17*, 3977.
6. Cortese, B.; D'Amone, S.; Manca, M.; Viola, I.; Cingolani, R.; Gigli, G. Superhydrophobicity due to the hierarchical scale roughness of PDMS surfaces. *Langmuir* 2008, *24*, 2712-2718.
7. Guo, Z.; Fang, J.; Wang, L.; Liu, W. Fabrication of superhydrophobic copper by wet chemical reaction. *Thin Solid Films* 2007, *515*, 7190-7194.

8. Wang, M.; Raghunathan, N.; Ziaie, B. A nonlithographic top-down electrochemical approach for creating hierarchical (micro-nano) superhydrophobic silicon surfaces. *Langmuir* 2007, *23*, 2300-2303.
9. Martines, E.; Seunarine, K.; Morgan, H.; Gadegaard, N.; Wilkinson, C. D.; Riehle, M. O. Superhydrophobicity and superhydrophilicity of regular nanopatterns. *Nano letters* 2005, *5*, 2097-2103.
10. Qu, M.; Zhao, G.; Wang, Q.; Cao, X.; Zhang, J. Fabrication of superhydrophobic surfaces by a Pt nanowire array on Ti/Si substrates. *Nanotechnology* 2008, *19*, 055707.
11. Xi, J.; Feng, L.; Jiang, L. A general approach for fabrication of superhydrophobic and superamphiphobic surfaces. *Appl. Phys. Lett.* 2008, *92*, 053102.
12. Ma, M.; Gupta, M.; Li, Z.; Zhai, L.; Gleason, K. K.; Cohen, R. E.; Rubner, M. F.; Rutledge, G. C. Decorated electrospun fibers exhibiting superhydrophobicity. *Adv Mater* 2007, *19*, 255-259.
13. Wenzel, R. N. Resistance of solid surfaces to wetting by water. *Industrial & Engineering Chemistry* 1936, *28*, 988-994.
14. Cassie, A.; Baxter, S. Wettability of porous surfaces. *Transactions of the Faraday Society* 1944, *40*, 546-551.

15. Steele, A. *Durable nanocomposites for superhydrophobicity and superoleophobicity*; 2011; .
16. Kinnersley, S.; Roelen, A. The contribution of design to accidents. *Saf. Sci.* 2007, *45*, 31-60.
17. Sokhey, J. Images of ice accretion in aircraft engines. 2014.
18. Parent, O.; Ilinca, A. Anti-icing and de-icing techniques for wind turbines: Critical review. *Cold Reg. Sci. Technol.* 2011, *65*, 88-96.
19. Render, P.; Jenkinson, L. Investigation into ice detection parameters for turboprop aircraft. *J. Aircr.* 1996, *33*, 125-130.
20. Steele, A.; Bayer, I.; Loth, E. Inherently superoleophobic nanocomposite coatings by spray atomization. *Nano letters* 2008, *9*, 501-505.
21. Latthe, S. S.; Rao, A. V. Superhydrophobic SiO₂ micro-particle coatings by spray method. *Surface and Coatings Technology* 2012, *207*, 489-492.
22. Hwang, H. S.; Kim, N. H.; Lee, S. G.; Lee, D. Y.; Cho, K.; Park, I. Facile fabrication of transparent superhydrophobic surfaces by spray deposition. *ACS applied materials & interfaces* 2011, *3*, 2179-2183.

23. Teisala, H.; Tuominen, M.; Aromaa, M.; Mäkelä, J.; Stepien, M.; Saarinen, J.; Toivakka, M.; Kuusipalo, J. Development of superhydrophobic coating on paperboard surface using the liquid flame spray. *Surface and Coatings Technology* 2010, *205*, 436-445.
24. Manoudis, P.; Tsakalof, A.; Karapanagiotis, I.; Zuburtikudis, I.; Panayiotou, C. Fabrication of super-hydrophobic surfaces for enhanced stone protection. *Surface and coatings technology* 2009, *203*, 1322-1328.
25. Schutzius, T. M.; Tiwari, M. K.; Bayer, I. S.; Megaridis, C. M. High strain sustaining, nitrile rubber based, large-area, superhydrophobic, nanostructured composite coatings. *Composites Part A: Applied Science and Manufacturing* 2011, *42*, 979-985.
26. Crick, C. R.; Parkin, I. P. Superhydrophobic polymer films via aerosol assisted deposition—Taking a leaf out of nature's book. *Thin Solid Films* 2010, *518*, 4328-4335.
27. Yang, J.; Zhang, Z.; Men, X.; Xu, X. Fabrication of stable, transparent and superhydrophobic nanocomposite films with polystyrene functionalized carbon nanotubes. *Appl. Surf. Sci.* 2009, *255*, 9244-9247.

28. Ogihara, H.; Okagaki, J.; Saji, T. Facile fabrication of colored superhydrophobic coatings by spraying a pigment nanoparticle suspension. *Langmuir* 2011, *27*, 9069-9072.
29. Hong, L.; Pan, T. Photopatternable superhydrophobic nanocomposites for microfabrication. *Microelectromechanical Systems, Journal of* 2010, *19*, 246-253.
30. Xu, X.; Zhang, Z.; Guo, F.; Yang, J.; Zhu, X.; Zhou, X.; Xue, Q. Fabrication of Bionic Superhydrophobic Manganese Oxide/Polystyrene Nanocomposite Coating. *Journal of Bionic Engineering* 2012, *9*, 11-17.
31. Eigenbrod, V.; Hensch, C.; Pulker, H. Superhydrophobic Coatings for Technical Applications. *Vakuum in Forschung und Praxis* 2011, *23*, 24-27.
32. Steele, A.; Bayer, I.; Loth, E. Adhesion strength and superhydrophobicity of polyurethane/organoclay nanocomposite coatings. *J Appl Polym Sci* 2012, *125*, E445-E452.
33. Bayer, I. S.; Brown, A.; Steele, A.; Loth, E. Transforming anaerobic adhesives into highly durable and abrasion resistant superhydrophobic organoclay nanocomposite films: a new hybrid spray adhesive for tough superhydrophobicity. *Applied physics express* 2009, *2*, 125003.

34. Harton, S. E.; Templeman, C. G.; Vyletel, B. Percolation-driven multiscale roughening for superhydrophobic polymer nanocomposite coatings. *Macromolecules* 2010, *43*, 3173-3176.
35. Wei, Z.; Liu, W.; Xiao, C.; Tian, D.; Fan, Z.; Sun, X.; Wang, X. Based on atom transfer radical polymerization method preparation of fluoropolymer superhydrophobic films. *Thin Solid Films* 2010, *518*, 6972-6976.
36. Desbief, S.; Grignard, B.; Detrembleur, C.; Rioboo, R.; Vaillant, A.; Seveno, D.; Voué, M.; De Coninck, J.; Jonas, A. M.; Jérôme, C. Superhydrophobic aluminum surfaces by deposition of micelles of fluorinated block copolymers. *Langmuir* 2009, *26*, 2057-2067.
37. Stalder, A.; Kulik, G.; Sage, D.; Barbieri, L.; Hoffmann, P. A snake-based approach to accurate determination of both contact points and contact angles. *Colloids Surf. Physicochem. Eng. Aspects* 2006, *286*, 92-103.
38. Michael, N.; Bhushan, B. Hierarchical roughness makes superhydrophobic states stable. *Microelectronic engineering* 2007, *84*, 382-386.
39. Hussein, H. J.; Capp, S. P.; George, W. K. Velocity measurements in a high-Reynolds-number, momentum-conserving, axisymmetric, turbulent jet. *J. Fluid Mech.* 1994, *258*, 31-75.

40. Papadopoulos, G.; Pitts, W. M. A generic centerline velocity decay curve for initially turbulent axisymmetric jets. *Journal of fluids engineering* 1999, *121*, 80-85.
41. Steele, A.; Nayak, B. K.; Davis, A.; Gupta, M. C.; Loth, E. Linear abrasion of a titanium superhydrophobic surface prepared by ultrafast laser microtexturing. *J Micromech Microengineering* 2013, *23*, 115012.
42. Yin, L.; Xia, Q.; Xue, J.; Yang, S.; Wang, Q.; Chen, Q. In situ investigation of ice formation on surfaces with representative wettability. *Appl. Surf. Sci.* 2010, *256*, 6764-6769.
43. Karmouch, R.; Ross, G. G. Experimental study on the evolution of contact angles with temperature near the freezing point. *The Journal of Physical Chemistry C* 2010, *114*, 4063-4066.
44. Mockenhaupt, B.; Ensikat, H.; Spaeth, M.; Barthlott, W. Superhydrophobicity of biological and technical surfaces under moisture condensation: Stability in relation to surface structure. *Langmuir* 2008, *24*, 13591-13597.
45. Furuta, T.; Sakai, M.; Isobe, T.; Nakajima, A. Effect of dew condensation on the wettability of rough hydrophobic surfaces coated with two different silanes. *Langmuir* 2010, *26*, 13305-13309.

46. Chen, C.; Cai, Q.; Tsai, C.; Chen, C.; Xiong, G.; Yu, Y.; Ren, Z. Dropwise condensation on superhydrophobic surfaces with two-tier roughness. *Appl. Phys. Lett.* 2007, *90*, 173108.
47. Dorrer, C.; Rühe, J. Wetting of silicon nanoglass: from superhydrophilic to superhydrophobic surfaces. *Adv Mater* 2008, *20*, 159-163.
48. He, M.; Li, H.; Wang, J.; Song, Y. Superhydrophobic surface at low surface temperature. *Appl. Phys. Lett.* 2011, *98*, 093118.
49. Yin, L.; Zhu, L.; Wang, Q.; Ding, J.; Chen, Q. Superhydrophobicity of natural and artificial surfaces under controlled condensation conditions. *ACS applied materials & interfaces* 2011, *3*, 1254-1260.
50. Yarin, A. Drop impact dynamics: splashing, spreading, receding, bouncing.... *Annu. Rev. Fluid Mech.* 2006, *38*, 159-192.
51. Worthington, A. On the forms assumed by drops of liquids falling vertically on a horizontal plate. *Proceedings of the royal society of London* 1876, *25*, 261-272.
52. Worthington, A. A Second Paper on the Forms Assumed by Drops of Liquids Falling Vertically on a Horizontal Plate. *Proceedings of the Royal Society of London* 1876, *25*, 498-503.

53. Bayer, I. S.; Megaridis, C. M. Contact angle dynamics in droplets impacting on flat surfaces with different wetting characteristics. *J. Fluid Mech.* 2006, *558*, 415-449.
54. Šikalo, Š; Marengo, M.; Tropea, C.; Ganić, E. Analysis of impact of droplets on horizontal surfaces. *Exp. Therm. Fluid Sci.* 2002, *25*, 503-510.
55. Šikalo, Š; Ganić, E. Phenomena of droplet-surface interactions. *Exp. Therm. Fluid Sci.* 2006, *31*, 97-110.
56. Gunjal, P. R.; Ranade, V. V.; Chaudhari, R. V. Dynamics of drop impact on solid surface: experiments and VOF simulations. *AIChE J.* 2005, *51*, 59-78.
57. Lunkad, S. F.; Buwa, V. V.; Nigam, K. Numerical simulations of drop impact and spreading on horizontal and inclined surfaces. *Chemical Engineering Science* 2007, *62*, 7214-7224.
58. Mao, T.; Kuhn, D.; Tran, H. Spread and rebound of liquid droplets upon impact on flat surfaces. *AIChE J.* 1997, *43*, 2169-2179.
59. Rioboo, R.; Marengo, M.; Tropea, C. Time evolution of liquid drop impact onto solid, dry surfaces. *Exp. Fluids* 2002, *33*, 112-124.

60. Bolleddula, D.; Berchielli, A.; Aliseda, A. Impact of a heterogeneous liquid droplet on a dry surface: Application to the pharmaceutical industry. *Adv. Colloid Interface Sci.* 2010, *159*, 144-159.
61. Son, Y.; Kim, C.; Yang, D. H.; Ahn, D. J. Spreading of an inkjet droplet on a solid surface with a controlled contact angle at low Weber and Reynolds numbers. *Langmuir* 2008, *24*, 2900-2907.
62. van Dam, D. B.; Le Clerc, C. Experimental study of the impact of an ink-jet printed droplet on a solid substrate. *Physics of Fluids (1994-present)* 2004, *16*, 3403-3414.
63. Lagubeau, G.; Fontelos, M. A.; Josserand, C.; Maurel, A.; Pagneux, V.; Petitjeans, P. Spreading dynamics of drop impacts. *J. Fluid Mech.* 2012, *713*, 50-60.
64. Chandra, S.; Avedisian, C. On the collision of a droplet with a solid surface. *Proceedings: Mathematical and Physical Sciences* 1991, 13-41.
65. Wang, Z.; Lopez, C.; Hirs, A.; Koratkar, N. Impact dynamics and rebound of water droplets on superhydrophobic carbon nanotube arrays. *Appl. Phys. Lett.* 2007, *91*, 023105.

66. Jung, Y. C.; Bhushan, B. Dynamic effects of bouncing water droplets on superhydrophobic surfaces. *Langmuir* 2008, *24*, 6262-6269.
67. Comeau, D.; LaTourette, K.; Pate, J. The effect of weber number and spread factor of a water droplet impinging on a super-hydrophobic substrate. 2007.
68. Clanet, C.; Béguin, C.; Richard, D.; Quéré, D. Maximal deformation of an impacting drop. *J. Fluid Mech.* 2004, *517*, 199-208.
69. Mohammadi, M.; Moghtadernejad, S.; Graham, P. J.; Dolatabadi, A. Dynamic Impact Behavior of Water Droplet on a Superhydrophobic Surface in the Presence of Stagnation Flow. *Applied Mechanics and Materials* 2012, *232*, 267-272.
70. Chen, L.; Xiao, Z.; Chan, P. C.; Lee, Y. Static and dynamic characterization of robust superhydrophobic surfaces built from nano-flowers on silicon micro-post arrays. *J Micromech Microengineering* 2010, *20*, 105001.
71. Chen, L.; Xiao, Z.; Chan, P. C.; Lee, Y.; Li, Z. A comparative study of droplet impact dynamics on a dual-scaled superhydrophobic surface and lotus leaf. *Appl. Surf. Sci.* 2011, *257*, 8857-8863.

72. Tsai, P.; Hendrix, M. H.; Dijkstra, R. R.; Shui, L.; Lohse, D. Microscopic structure influencing macroscopic splash at high Weber number. *Soft Matter* 2011, 7, 11325-11333.
73. Kwon, D. H.; Lee, S. J. Impact and wetting behaviors of impinging microdroplets on superhydrophobic textured surfaces. *Appl. Phys. Lett.* 2012, 100, 171601.
74. Pearson, J. T.; Maynes, D.; Webb, B. W. Droplet impact dynamics for two liquids impinging on anisotropic superhydrophobic surfaces. *Exp. Fluids* 2012, 53, 603-618.
75. Šikalo, Š; Tropea, C.; Ganić, E. Impact of droplets onto inclined surfaces. *J. Colloid Interface Sci.* 2005, 286, 661-669.
76. Chiarot, P. R.; Jones, T. Grazing impact of continuous droplet streams with a superhydrophobic surface. *Exp. Fluids* 2010, 49, 1109-1119.
77. Zheng, L.; Li, Z.; Bourdo, S.; Khedir, K. R.; Asar, M. P.; Ryerson, C. C.; Biris, A. S. Exceptional superhydrophobicity and low velocity impact icephobicity of acetone-functionalized carbon nanotube films. *Langmuir* 2011, 27, 9936-9943.
78. van Boxel, J. H. Numerical model for the fall speed of raindrops in a rainfall simulator. *Workshop on Wind and Water Erosion* 1997.

79. Schiaffino, S.; Sonin, A. A. Molten droplet deposition and solidification at low Weber numbers. *Physics of Fluids (1994-present)* 1997, 9, 3172-3187.
80. Glycerine Producers' Association *Physical properties of glycerine and its solutions*; Glycerine Producers' Association: 1963; .
81. Hare, D.; Sorensen, C. The density of supercooled water. II. Bulk samples cooled to the homogeneous nucleation limit. *J. Chem. Phys.* 1987, 87, 4840-4845.
82. Kestin, J.; Sokolov, M.; Wakeham, W. A. Viscosity of liquid water in the range—8 C to 150 C. *Journal of Physical and Chemical Reference Data* 1978, 7, 941-948.
83. Hacker, P. T. *Experimental values of the surface tension of supercooled water*; National Advisory Committee for Aeronautics: 1951; .
84. Richard, D.; Clanet, C.; Quéré, D. Surface phenomena: Contact time of a bouncing drop. *Nature* 2002, 417, 811-811.
85. Antonini, C.; Villa, F.; Bernagozzi, I.; Amirfazli, A.; Marengo, M. Drop Rebound after Impact: The Role of the Receding Contact Angle. *Langmuir* 2013.
86. Jung, S.; Dorrestijn, M.; Raps, D.; Das, A.; Megaridis, C. M.; Poulikakos, D. Are superhydrophobic surfaces best for icephobicity? *Langmuir* 2011, 27, 3059-3066.

87. Cao, L.; Jones, A. K.; Sikka, V. K.; Wu, J.; Gao, D. Anti-icing superhydrophobic coatings. *Langmuir* 2009, *25*, 12444-12448.
88. Mishchenko, L.; Hatton, B.; Bahadur, V.; Taylor, J. A.; Krupenkin, T.; Aizenberg, J. Design of ice-free nanostructured surfaces based on repulsion of impacting water droplets. *Acs Nano* 2010, *4*, 7699-7707.
89. Farhadi, S.; Farzaneh, M.; Kulinich, S. Anti-icing performance of superhydrophobic surfaces. *Appl. Surf. Sci.* 2011, *257*, 6264-6269.
90. Wang, F.; Li, C.; Lv, Y.; Lv, F.; Du, Y. Ice accretion on superhydrophobic aluminum surfaces under low-temperature conditions. *Cold Reg. Sci. Technol.* 2010, *62*, 29-33.
91. Tourkine, P.; Le Merrer, M.; Quéré, D. Delayed freezing on water repellent materials. *Langmuir* 2009, *25*, 7214-7216.
92. Meuler, A. J.; McKinley, G. H.; Cohen, R. E. Exploiting topographical texture to impart icephobicity. *ACS nano* 2010, *4*, 7048-7052.
93. Sarshar, M. A.; Swartz, C.; Hunter, S.; Simpson, J.; Choi, C. Effects of contact angle hysteresis on ice adhesion and growth on superhydrophobic surfaces under dynamic flow conditions. *Colloid Polym. Sci.* 2013, *291*, 427-435.

94. He, M.; Wang, J.; Li, H.; Song, Y. Super-hydrophobic surfaces to condensed micro-droplets at temperatures below the freezing point retard ice/frost formation. *Soft Matter* 2011, *7*, 3993-4000.
95. Yang, S.; Xia, Q.; Zhu, L.; Xue, J.; Wang, Q.; Chen, Q. Research on the icephobic properties of fluoropolymer-based materials. *Appl. Surf. Sci.* 2011, *257*, 4956-4962.
96. Jung, S.; Tiwari, M. K.; Doan, N. V.; Poulikakos, D. Mechanism of supercooled droplet freezing on surfaces. *Nature communications* 2012, *3*, 615.
97. Kulinich, S.; Farhadi, S.; Nose, K.; Du, X. Superhydrophobic surfaces: are they really ice-repellent? *Langmuir* 2010, *27*, 25-29.
98. Antonini, C.; Innocenti, M.; Horn, T.; Marengo, M.; Amirfazli, A. Understanding the effect of superhydrophobic coatings on energy reduction in anti-icing systems. *Cold Reg. Sci. Technol.* 2011, *67*, 58-67.
99. Ahlborn, G.; Poehlmann, H. *Development of a hydrophobic substance to mitigate pavement ice adhesion* 1976.
100. Bascom, W.; Cottington, R.; Singleterry, C. Ice adhesion to hydrophilic and hydrophobic surfaces. *The Journal of Adhesion* 1969, *1*, 246-263.

101. Raraty, L.; Tabor, D. The adhesion and strength properties of ice. *Proceedings of the Royal Society of London. Series A. Mathematical and Physical Sciences* 1958, *245*, 184-201.
102. Jellinek, H. H. G. Adhesive properties of ice. *J. Colloid Sci.* 1959, *14*, 268-280.
103. Anderson, D. N.; Reich, A. D. *Tests of the performance of coatings for low ice adhesion*; National Aeronautics and Space Administration: 1997; .
104. Zou, M.; Beckford, S.; Wei, R.; Ellis, C.; Hatton, G.; Miller, M. Effects of surface roughness and energy on ice adhesion strength. *Appl. Surf. Sci.* 2011, *257*, 3786-3792.
105. Meuler, A. J.; Smith, J. D.; Varanasi, K. K.; Mabry, J. M.; McKinley, G. H.; Cohen, R. E. Relationships between water wettability and ice adhesion. *ACS applied materials & interfaces* 2010, *2*, 3100-3110.
106. Laforte, C.; Laforte, J.; Carrière, J. In *In How a solid coating can reduce the adhesion of ice on a structure*; Proceedings of the International Workshop on Atmospheric Icing of Structures (IWAIS); 2002; , pp 1-5.
107. Jafari, R.; Menini, R.; Farzaneh, M. Superhydrophobic and icephobic surfaces prepared by RF-sputtered polytetrafluoroethylene coatings. *Appl. Surf. Sci.* 2010, *257*, 1540-1543.

108. Ge, L.; Ding, G.; Wang, H.; Yao, J.; Cheng, P.; Wang, Y. Anti-icing property of superhydrophobic octadecyltrichlorosilane film and its ice adhesion strength. *Journal of Nanomaterials* 2013, 2013, 3.
109. Kimura, S.; Yamagishi, Y.; Sakabe, A.; Adachi, T. A new surface coating for prevention of icing on airfoils. *Training* 2007, 2011, 03-04.
110. Dodiuk, H.; Kenig, S.; Dotan, A. Do Self-cleaning Surfaces Repel Ice? *J. Adhes. Sci. Technol.* 2012, 26, 701-714.
111. Kulinich, S.; Farzaneh, M. On ice-releasing properties of rough hydrophobic coatings. *Cold Reg. Sci. Technol.* 2011, 65, 60-64.
112. Kulinich, S.; Farzaneh, M. Ice adhesion on super-hydrophobic surfaces. *Appl. Surf. Sci.* 2009, 255, 8153-8157.
113. Kulinich, S.; Farzaneh, M. How wetting hysteresis influences ice adhesion strength on superhydrophobic surfaces. *Langmuir* 2009, 25, 8854-8856.
114. Wang, F.; Lv, F.; Liu, Y.; Li, C.; Lv, Y. Ice adhesion on different microstructure superhydrophobic aluminum surfaces. *J. Adhes. Sci. Technol.* 2013, 27, 58-67.

115. Wang, Y.; Xue, J.; Wang, Q.; Chen, Q.; Ding, J. Verification of icephobic/anti-icing properties of a superhydrophobic surface. *ACS applied materials & interfaces* 2013, *5*, 3370-3381.
116. Dotan, A.; Dodiuk, H.; Laforte, C.; Kenig, S. The relationship between water wetting and ice adhesion. *J. Adhes. Sci. Technol.* 2009, *23*, 1907-1915.
117. Susoff, M.; Siegmann, K.; Pfaffenroth, C.; Hirayama, M. Evaluation of icephobic coatings—Screening of different coatings and influence of roughness. *Appl. Surf. Sci.* 2013, *282*, 870-879.
118. Chen, J.; Liu, J.; He, M.; Li, K.; Cui, D.; Zhang, Q.; Zeng, X.; Zhang, Y.; Wang, J.; Song, Y. Superhydrophobic surfaces cannot reduce ice adhesion. *Appl. Phys. Lett.* 2012, *101*, 111603.
119. Hassan, M.; Lee, H.; Lim, S. The variation of ice adhesion strength with substrate surface roughness. *Measurement Science and Technology* 2010, *21*, 075701.
120. Varanasi, K. K.; Deng, T.; Smith, J. D.; Hsu, M.; Bhate, N. Frost formation and ice adhesion on superhydrophobic surfaces. *Appl. Phys. Lett.* 2010, *97*, 234102.

121. Andrews, E.; Stevenson, A. Fracture energy of epoxy resin under plane strain conditions. *J. Mater. Sci.* 1978, *13*, 1680-1688.
122. Andrews, E.; Lockington, N. The cohesive and adhesive strength of ice. *J. Mater. Sci.* 1983, *18*, 1455-1465.
123. Andrews, E.; Majid, H.; Lockington, N. Adhesion of ice to a flexible substrate. *J. Mater. Sci.* 1984, *19*, 73-81.
124. Boyer, R. Titanium for aerospace: rationale and applications. *Advanced Performance Materials* 1995, *2*, 349-368.
125. Alansatan, S.; Papadakis, M. *Experimental investigation of ice adhesion* 1999.
126. Ide, R. F. *Liquid water content and droplet size calibration of the NASA Lewis Icing Research Tunnel*; NASA: 1990; .
127. Namjoshi, S.; Jain, V.; Mall, S. Effects of shot-peening on fretting-fatigue behavior of Ti-6Al-4V. *Journal of engineering materials and technology* 2002, *124*, 222-228.
128. Gadelmawla, E.; Koura, M.; Maksoud, T.; Elewa, I.; Soliman, H. Roughness parameters. *J. Mater. Process. Technol.* 2002, *123*, 133-145.

129. Metrology, M. Spatial Parameters ACF (Autocorrelation Function).
http://www.michmet.com/3d_s_spatial_parameters_acf.htm (accessed March, 28, 2014).
130. Varanasi, K. K.; Deng, T.; Hsu, M.; Bhate, N. Hierarchical Superhydrophobic Surfaces Resist Water Droplet Impact. 2009.
131. Extrand, C. Designing for optimum liquid repellency. *Langmuir* 2006, *22*, 1711-1714.
132. Fortin, G.; Perron, J. Ice adhesion models to predict shear stress at shedding. *J. Adhes. Sci. Technol.* 2012, *26*, 523-553.
133. Yeh, K.; Chen, L.; Chang, J. Contact angle hysteresis on regular pillar-like hydrophobic surfaces. *Langmuir* 2008, *24*, 245-251.
134. Öner, D.; McCarthy, T. J. Ultrahydrophobic surfaces. Effects of topography length scales on wettability. *Langmuir* 2000, *16*, 7777-7782.
135. Padmanabhan, S.; Bose, A. The importance of direct measurement of dynamic contact angles during the wetting of solids by surfactant solutions. *J. Colloid Interface Sci.* 1988, *126*, 164-170.

136. Gao, L.; McCarthy, T. J. Teflon is hydrophilic. Comments on definitions of hydrophobic, shear versus tensile hydrophobicity, and wettability characterization. *Langmuir* 2008, *24*, 9183-9188.
137. Chen, W.; Fadeev, A. Y.; Hsieh, M. C.; Öner, D.; Youngblood, J.; McCarthy, T. J. Ultrahydrophobic and ultralyophobic surfaces: some comments and examples. *Langmuir* 1999, *15*, 3395-3399.
138. Wang, S.; Jiang, L. Definition of superhydrophobic states. *Adv Mater* 2007, *19*, 3423-3424.
139. Bhushan, B.; Nosonovsky, M. The rose petal effect and the modes of superhydrophobicity. *Philos. Trans. A. Math. Phys. Eng. Sci.* 2010, *368*, 4713-4728.
140. Shanahan, M. E. Simple Theory of " Stick-Slip " Wetting Hysteresis. *Langmuir* 1995, *11*, 1041-1043.
141. Extrand, C. Contact angles and hysteresis on surfaces with chemically heterogeneous islands. *Langmuir* 2003, *19*, 3793-3796.
142. Gao, L.; McCarthy, T. J. Contact angle hysteresis explained. *Langmuir* 2006, *22*, 6234-6237.

143. Extrand, C. Model for contact angles and hysteresis on rough and ultraphobic surfaces. *Langmuir* 2002, *18*, 7991-7999.
144. Patankar, N. A. Hysteresis with regard to Cassie and Wenzel states on superhydrophobic surfaces. *Langmuir* 2010, *26*, 7498-7503.
145. Krumpfer, J. W.; McCarthy, T. J. Contact angle hysteresis: a different view and a trivial recipe for low hysteresis hydrophobic surfaces. *Faraday Discuss.* 2010, *146*, 103-111.
146. Dorrer, C.; Rühe, J. Micro to nano: Surface size scale and superhydrophobicity. *Beilstein journal of nanotechnology* 2011, *2*, 327-332.
147. Reyssat, M.; Quéré, D. Contact Angle Hysteresis Generated by Strong Dilute Defects†. *The Journal of Physical Chemistry B* 2009, *113*, 3906-3909.
148. Gao, L.; McCarthy, T. J. The “lotus effect” explained: two reasons why two length scales of topography are important. *Langmuir* 2006, *22*, 2966-2967.
149. Bukowsky, C.; Torres, J. M.; Vogt, B. D. Slip-stick wetting and large contact angle hysteresis on wrinkled surfaces. *J. Colloid Interface Sci.* 2011, *354*, 825-831.

150. Ramos, S.; Tanguy, A. Pinning-depinning of the contact line on nanorough surfaces. *The European Physical Journal E* 2006, *19*, 433-440.
151. Lv, C.; Yang, C.; Hao, P.; He, F.; Zheng, Q. Sliding of water droplets on microstructured hydrophobic surfaces. *Langmuir* 2010, *26*, 8704-8708.
152. Smyth, K. M.; Paxson, A. T.; Kwon, H.; Varanasi, K. K. Visualization of contact line motion on hydrophobic textures. *Surface Innovations* 2012, *1*, 84-91.
153. Priest, C.; Albrecht, T. W.; Sedev, R.; Ralston, J. Asymmetric wetting hysteresis on hydrophobic microstructured surfaces. *Langmuir* 2009, *25*, 5655-5660.
154. Duursma, G.; Sefiane, K.; David, S. Advancing and receding contact lines on patterned structured surfaces. *Chem. Eng. Res. Design* 2010, *88*, 737-743.
155. Kusumaatmaja, H.; Yeomans, J. Modeling contact angle hysteresis on chemically patterned and superhydrophobic surfaces. *Langmuir* 2007, *23*, 6019-6032.
156. Mognetti, B.; Yeomans, J. Modeling receding contact lines on superhydrophobic surfaces. *Langmuir* 2010, *26*, 18162-18168.

157. Zhang, J.; Kwok, D. Y. Contact line and contact angle dynamics in superhydrophobic channels. *Langmuir* 2006, *22*, 4998-5004.
158. Paxson, A. T.; Varanasi, K. K. Self-similarity of contact line depinning from textured surfaces. *Nature communications* 2013, *4*, 1492.
159. Milionis, A.; Martiradonna, L.; Anyfantis, G. C.; Cozzoli, P. D.; Bayer, I. S.; Fragouli, D.; Athanassiou, A. Control of the water adhesion on hydrophobic micropillars by spray coating technique. *Colloid Polym. Sci.* 2013, *291*, 401-407.
160. Milionis, A.; Fragouli, D.; Martiradonna, L.; Anyfantis, G. C.; Cozzoli, P. D.; Bayer, I. S.; Athanassiou, A. Spatially Controlled Surface Energy Traps on Superhydrophobic Surfaces. *ACS applied materials & interfaces* 2014.
161. Steele, A.; Bayer, I.; Moran, S.; Cannon, A.; King, W. P.; Loth, E. Conformal ZnO nanocomposite coatings on micro-patterned surfaces for superhydrophobicity. *Thin Solid Films* 2010, *518*, 5426-5431.
162. Cao, L.; Hu, H.; Gao, D. Design and fabrication of micro-textures for inducing a superhydrophobic behavior on hydrophilic materials. *Langmuir* 2007, *23*, 4310-4314.
163. Bhushan, B.; Nosonovsky, M.; Jung, Y. C. Towards optimization of patterned superhydrophobic surfaces. *J. R. Soc. Interface* 2007, *4*, 643-648.

164. Lander, L. M.; Siewierski, L. M.; Brittain, W. J.; Vogler, E. A. A systematic comparison of contact angle methods. *Langmuir* 1993, *9*, 2237-2239.
165. Sakai, M.; Kono, H.; Nakajima, A.; Zhang, X.; Sakai, H.; Abe, M.; Fujishima, A. Sliding of Water Droplets on the Superhydrophobic Surface with ZnO Nanorods†† Part of the “Langmuir 25th Year: Wetting and superhydrophobicity” special issue. *Langmuir* 2009, *25*, 14182-14186.